NEUTRON DIFFRACTION STUDY OF PHASE TRANSITIONS IN MICROPOROUS-COLUMNAR SI ELECTRODES FOR LI-ION BATTERIES USING IN-SITU ELECTROCHEMICAL CELL

by

Bhaskar Sravan Vadlamani

A dissertation submitted to the faculty of
The University of Utah
in partial fulfillment of the requirements for the degree of

Doctor of Philosophy

Department of Metallurgical Engineering

The University of Utah

August 2017

The University of Utah Graduate School

STATEMENT OF DISSERTATION APPROVAL

The dissertation of **Bhaskar Sravan Vadlamani**

has been approved by the following supervisory committee members:

K. S. Ravi Chandran	, Chair	**04/26/2017** Date Approved
Manoranjan Misra	, Member	**04/26/2017** Date Approved
Michael L. Free	, Member	**04/25/2017** Date Approved
Anil Virkar	, Member	**04/25/2017** Date Approved
Henry S. White	, Member	**04/25/2017** Date Approved
Ke An	, Member	**04/25/2017** Date Approved

and by **Manoranjan Misra** , Chair/Dean of

the Department/College/School of **Metallurgical Engineering**

and by David B. Kieda, Dean of The Graduate School.

ABSTRACT

The research can be broadly divided into three parts: (i) design of an in-situ electrochemical cell that can be used for neutron diffraction studies of small-volume electrodes in Li-ion batteries, (ii) development of Si (100) electrode with microporous columnar architecture to achieve high energy storage capacity, and (iii) neutron diffraction investigation of lithiation phenomenon in microporous columnar Si (100) electrode using the in-situ cell.

The first part of the work is concerned with the design and performance of a novel in-situ electrochemical cell that greatly facilitates the neutron diffraction study of complex phase transitions in small volume electrodes of Li-ion cells. The unique aspect of cell design is that it uses single crystal Si (100) sheets as casing material and planar cell configuration, giving an improved signal-to-noise ratio relative to other casing materials. Diffraction patterns of high quality that are Rietveld-refinable could be obtained simultaneously for all the electrodes in graphite/$LiCoO_2$ and graphite/$LiMn_2O_4$ cells during cycling. It is shown that most of the finer details of the phase transitions, and the associated changes in crystallographic parameters of electrode phases, can be captured.

The second part of the work is concerned with microstructure engineering Si electrode, to produce columnar microporous structure, which can achieve high energy storage capacity. It is shown that this electrode provides a highly reversible specific Li-storage capacity (~1250 mAh/g), and the highest total Li-storage capacity (~1.25

mAh/cm^2) relative to other Si electrodes. The most exciting finding of this study is that the volume expansion caused during lithiation is accommodated within the pores and the pore walls do not crumble even after a large number of cell cycles, mitigating the Si cracking issues. The present findings reveal a new pathway for architecturing Si electrodes for much larger and highly reversible total charge-storage capacities for on-chip Li-ion cells.

The third part of this research, focused on understanding the crystallographic and phase transformation aspect that leads to a high degree of reversible lithiation in the single layer microporous Si electrode, has been performed to understand the lithiation and phase transformation aspects. The results indicate that lithiation induces mosaicity during lithiation.

In loving memory of my sweet brother, Sai Sridhar Vadlamani (1991 to 2013).

TABLE OF CONTENTS

LIST OF TABLES

ACKNOWLEDGMENTS

If you can't explain it simply, you don't understand it well enough

-Albert Einstein

I would like to express my profound gratitude to my advisor, Prof. K.S. Ravi Chandran, for the wonderful guidance, patience, encouragement, and advice throughout my time as a PhD student. I thank him from the bottom of my heart for framing a challenging, distinct research problem and helping me solve it by inculcating critical thinking in me. The training I have undergone through numerous discussions with him not only helped me resolve key issues related to my research but also my personal life. I am grateful to him for being supportive when I had a serious issue related to my personal life. I just can't imagine a better and more concerned advisor than him for my PhD.

I would like to acknowledge my supervisory committee members: Prof. Anil Virkar, Dr. Ke An, Prof. Henry White, Prof. Michael Free, and Prof. Manoranjan Misra for their valuable help and suggestions. I am especially grateful to Prof. Anil Virkar for asking me critical questions during our discussions, which helped me shape a stronger thesis. I am thankful to Dr. Ke An and Dr. Stoica, who are the beamline scientists at the VULCAN diffractometer at SNS in Oak Ridge National Laboratory, for their help during the neutron diffraction experiments and subsequent data analysis.

I thank Dr. Subba Rao, formerly at National University of Singapore, for his valuable suggestions. I am thankful to Dr. Madhusudan Jagannathan for helping me with my

electrochemistry experiments during my initial days.

I am also grateful to the DOE-Office of Basic Energy Sciences for the financial support throughout my PhD. I am also thankful to the General User program of ORNL for providing me beam time to conduct in-situ neutron diffraction experiments at VULCAN diffractometer. I thank M. Frost, H. D. Skopenske and Dr. Y. Chen and Rhonda Moody, who are staff at SNS, for their support during experimentation. I also thank Brian Baker, Charles, Randy, Brian Van Denver and Paulo, who are staff at Nano Fab, University of Utah for all their support.

This acknowledgment would not be complete without thanking Evelyn Wells, Kay Argyle, Sara Wilson, and Brenda Wicks for their help with the administrative affairs in the department. Special thanks to my wonderful lab mates: Pankaj, Zhang Yuxuan, Fei Cao, Josh, Somnaug, Ahmed, and Jun Du. I am thankful to Asish Chanana, Aishwaryadev Banerjee, and Apratim Mujumdar, who were my buddies at nanofab, for their support during late night experiments.

I am thankful to Dr. Sastry S Indrakanti, Prof. P. Surya Parkash Rao (PSPR), Prof. M.K. Mohan, and Prof. G.M.K. Sharma who are faculty at NIT Warangal, India for all their strong support and encouragement towards research. I am especially indebted to Dr. Sastry S Indrakanti for strongly motivating me towards pursuing a PhD during my undergraduate days.

I would like to thank Prof. J. Gopalakrishnan (SSCU, IISc Bangalore), Prof. Olivier Gullion (TU Darmstadt), and Prof. J. Roedel (TU Darmstadt), who were summer intern advisors during my undergraduate studies, for making me have a feel for research.

Life would have been bore without my friends Pankaj, Seetapathi Rao, Srikanth, Moumita, Parth, Tosifa, Javed, Amrita, Tiwari, Dr. Mahesh, Dr. Prashant, Sindhoora, and Sayan. I am thankful to Krishanan Jee, Satish Jee, Mani Jee, Karthik, Rohit, Dr. Sai, Govinda, Sreeraj, Nagnedra, Prakash, Dr. Mahesh, Dr. Prashant for the wonderful spiritual discussions. I also

thank Krish, Mohan Rao, Prem, Srimanth, Phani, Bulgy, Prassu, Neti Ravi for all fun we had. I also thank Harini, Dr. Lalitha, Dr. Ajay, Dr. Rohini, Dr. Easwar, Dr. Rajesh Korla, Sandeep Vurra, and Poshig for all their support.

I am thankful to my uncle and aunt: Sitaram Ayyagari and Usha Sri, and Sriram Ayyagari and Sarmista for all their help. I am also thankful to my aunt Parvati Akka for all her support.

Last but not the least, I would like to thanks my parents Subrahmanya Sastry and Lakshmi for spiritually bringing me up right from my childhood and all the sacrifices they have made for my upbringing. I cannot express in my words how grateful I am to my grandparents Srirama Murthy and Naga Ratnam, Suryanarayana Murthy and Lakshmi Devi. It is all your prayers that have sustained me so far. Above all, I owe a lot to Almighty God for giving me the wisdom, courage, mental strength, and health to complete the research activity.

Bhaskar Vadlamani

August 2017

CHAPTER 1

INTRODUCTION

1.1 Background

Li-ion batteries have attracted the attention of mankind as energy storage devices, and they are found in a wide range of applications from portable electronics like smart phones, cameras, ipads, and laptops to emerging electric transportation systems like hybrid electric vehicles (HEVs), plug-in hybrid electric vehicles (PHEVs), and fully electric vehicles (EVs). Li-ion batteries outperform other battery systems like lead-acid, Ni-Cd, and Ni-MH, due to their higher gravimetric and volumetric energy densities (Figure 1.1).[1] The very high gravimetric energy storage densities of Li-ion batteries, as high as 120-150 W h kg^{-1} (two to three times that of typical Ni-Cd batteries), is possible because their cell voltage is above 3.6 V (three times those of alkaline battery systems), and due to their light weight (specific gravity of Li = 0.53 g cm^{-3}, Li equivalent weight of Li = 6.94 g mol^{-1}).

The current Li-ion battery technology can meet the power requirement of HEVs and PHEVs, but it needs to be developed further to meet the power requirement of EVs (Figure 1.2).[2] Also, the progress in Li-ion battery energy storage is not keeping pace with progress in the computer industry, which follows Moore's law that predicts a doubling of memory capacity every two years. The demand from ever increasing power requirements has spurred significant research interest in development of Li-ion battery electrodes with even higher energy and power densities.

A conventional Li-ion battery uses $LiCoO_2$ as positive electrode material and graphite as negative electrode material.[3] During charge/discharge, the Li-ion shuttles between the positive electrode and the negative electrode (Figure 1.3)—therefore Li-ion batteries are also called rocking chair batteries. The typical charge/discharge hysteresis curve obtained

for a Li-ion battery is shown in Figure 1.4.[4] The energy density of a Li-ion battery, which is the area under the charge/discharge curve, can be maximized by (i) increasing cell voltage and/or (ii) increasing gravimetric (mAh/g), volumetric (mAh/cm^3), or the total capacity (mAh/cm^2) of the electrodes. The strategy in choosing the positive and negative electrode pairs, in order to maintain cell voltage above 3 V, is that positive electrodes have voltage above 4 V and negative electrodes have voltage below 1V (preferably as close as possible to Li) (Figure 1.5).

Earlier research focused on development of positive electrode materials, such as $LiCoPO_4$ (LCP) which has higher voltage (Figure 1.5 a) and Lithium Nickel Cobalt Manganese Oxide (NCM), Lithium Nickel Cobalt Aluminum Oxide (NCA) which have higher gravimetric capacity (Figure 1.5 b) compared to conventional $LiCoO_2$.[5] But this has not resulted in significant improvement in energy density. This led the researchers to focus on negative electrode materials.

1.2 Alloy Anodes for Li-ion Batteries

Earlier work on Li-ion batteries focused on use of elemental Li for the negative electrode. This approach not only resulted in total cell failure, due to dendritic short circuiting,[6] but also introduced serious safety issues due to local overheating. Subsequently, the elemental Li (3860 mAh/g) was replaced with intercalation graphite (372 mAh/g) anodes, which is a huge sacrifice in energy density. There has been considerable interest in finding negative electrode alternatives to graphite electrodes which not only have higher Li storage capacities but also possess an ability to operate at higher current densities, lower irreversible capacity loss, better cycling performance,

lower specific volume and lower cost. Li alloy anodes have been of particular interest as they have huge specific capacities and are potential replacements for carbonaceous anodes.

Si, Sb, Sn, Al, and Mg are the potential candidates for alloy anodes as they can form alloys with Li and are also cheap, abundant, and environmentally friendly.[7] However, they could not find commercial application, because they undergo huge volume changes and undergo huge capacity fading due to phenomenon called "decrepitation" or "crumbling." For example, the specific capacity of Si, Ge, and Sn corresponding to $Li_{4.4}Si$, $Li_{4.4}Ge$, $Li_{4.4}Sn$ are 4200 mAh/g, 1600 mAh/g, and 1000 mAh/g and the respective volume changes are 400%, 370%, and 283%. The huge dimensional changes cause mechanical strain in the electrode particles and often result in fracture of particles into smaller pieces. This could result in loss of electrical contact between particles in the electrode and current collector, leading to capacity fading.[8,9]

The issues related to capacity fading in Si, which has the highest specific capacity of all the negative electrode materials (Figure 1.5 b), were partially overcome in the past by nanostructuring the electrodes to accommodate the huge volume changes.[10] The nanostructured morphologies include nanoparticles,[11] thin films,[12] nanowires,[13] nano tubes,[14] and microporous Si.[15,16,17,18] Although nanostructured electrodes help in overcoming issues not only related to volume changes but also diffusion, the areal mass loading density is generally poor (below 0.3 mg cm^{-2}) due to huge porosity.[10, 19] The mass loading density in Si electrodes need to be increased to more than 1 mg cm^{-2} to be competitive with a commercial graphite electrode, which has a total capacity above 2 mAh cm^{-2}. Si thin films, which are ~150 nm thick, deliver a total capacity of 0.08 mAh

cm^{-2} (specific capacity ~2200 mAh/g).[20] Si nanowires exhibit very high capacity of ~3500 mAh/g for 20 cycles.[13] However, the total capacity is only 0.7 mAh/cm^2. On the other hand, microporous Si,[15, 16] with areal mass loading density of ~ 1 mg cm^{-2}, can be fabricated by a cheaper electrochemical etching route. Moreover, the microstructure can be fine-tuned by controlling the electrochemical etching[21] parameters. In this research, we plan to explore the potential of microporous columnar Si as negative electrode material for Li-ion battery.

1.3 Neutron Diffraction Studies on Li-ion Batteries

The cycling of a Li-ion battery involves removal/insertion of the Li atom into the bulk of the electrode, thereby inducing phase transitions in the bulk of the electrode material.[22,23] The information obtained from the conventional electrochemical techniques is just from the surface, thereby preventing us from studying changes occurring in the bulk. But the capacity of a Li-ion battery electrode or battery performance in general is affected by whether there is a diffusion limitation challenge for the Li atom in the bulk. Therefore, the study of phase transitions—evolution and dissolution of various electrode phases, their crystal structural and microstructural aspects, phase fractions—is necessary to understand/improve the functioning of Li-ion batteries.

Conventionally, X-Ray Diffraction is used to study the phase transitions, but the information obtained is limited due to limited depth of penetration (<few tens of microns).[24] On the other hand, neutron diffraction is well suited for the study of electrode phase transitions in Li-ion cells due to higher depth of penetration[25] and higher neutron scattering cross-section of Li.[26] In this work, (a) we plan to design a Li-ion cell that can

be used to best track the real time phase transitions in Li-ion battery electrodes using neutron diffraction and (b) further use the cell to investigate the real time phase transitions in microporous Si electrodes.

1.4 Objectives of the Present Research

The objectives of the current research work are as follows:

(i) To design and demonstrate a novel in-situ electrochemical cell that produces neutron diffraction patterns with high signal-to-noise ratio, using a small volume of electrode materials. The evolution and dissolution of various electrode phases in $LiCoO_2$/graphite and $LiMn_2O_4$/graphite cells from both the electrodes will be simultaneously studied.

(ii) To synthesize microcolumnar porous Si with uniformly distributed columnar pores using a cheaper electrochemical etching route and test its electrochemical performance. The corresponding phase transitions occurring during cycling were investigated by electron diffraction.

(iii) To investigate the real time phase transitions occurring in microporous columnar Si using neutron diffraction.

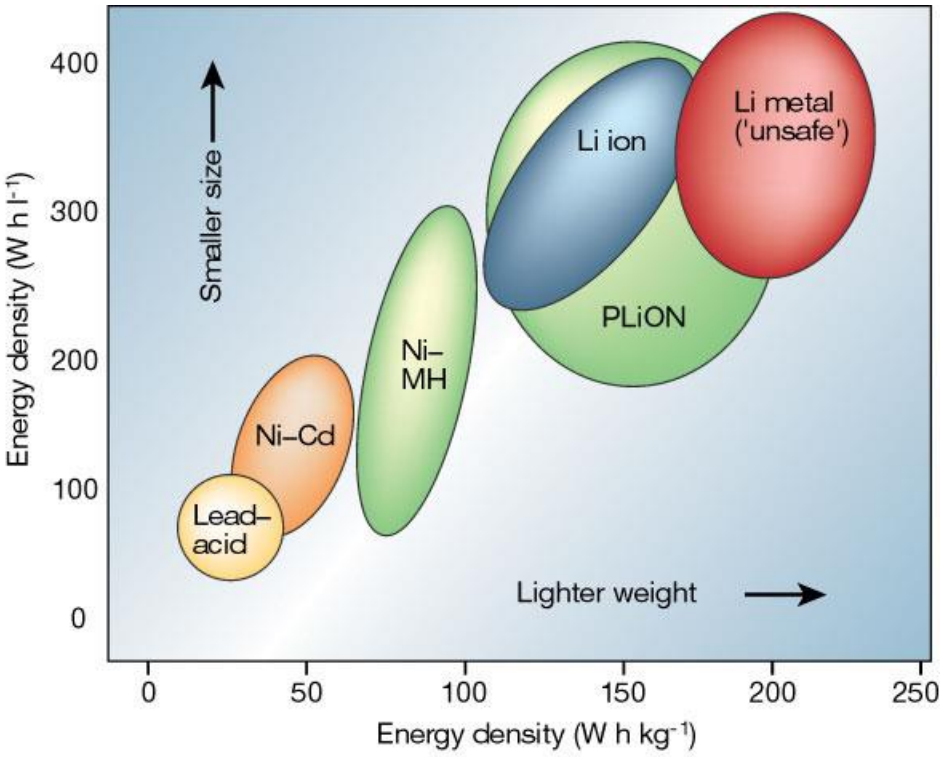

Figure 1.1 Comparison of gravimetric and volumetric energy densities of Lead-acid, Ni-Cd, Ni-MH, Li-ion, and PLion battery technologies. Reprinted with permission from J. M. Tarascon and M. Armand, Nature, 414, 359, 2001.[1] Copyright 2001 Nature.

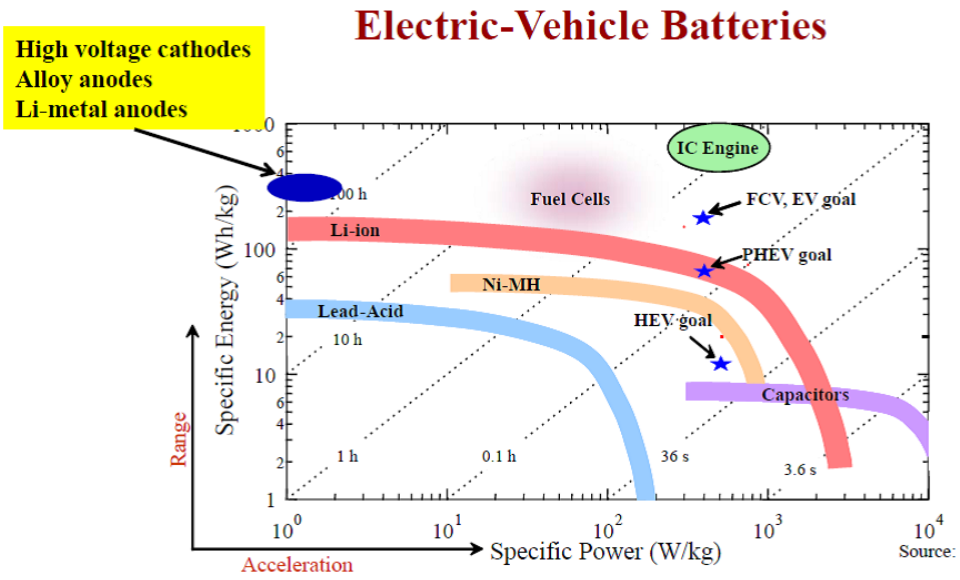

Figure 1.2 The specific energy and power capacities of several battery technologies. Reprinted with permission from V. Srinivasan, AIP Conference Proceedings, 283, 2008.[2] Copyright 2008 Nature.

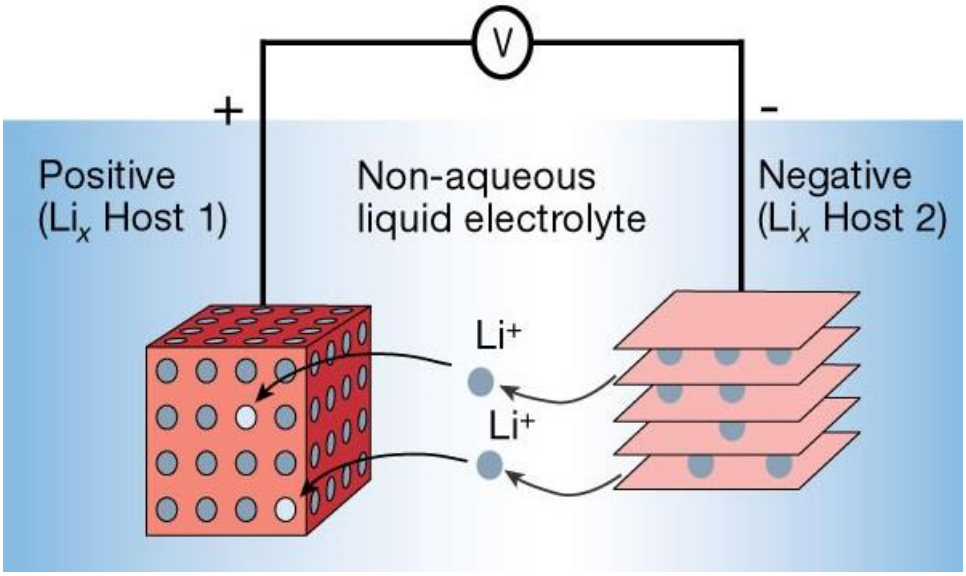

Figure 1.3 Schematic illustration of the working of a Li-ion battery consisting of insertion compounds as positive and negative electrodes. Reprinted with permission from J. M. Tarascon and M. Armand, Nature, 414, 359, 2001.[1] Copyright 2001 Nature.

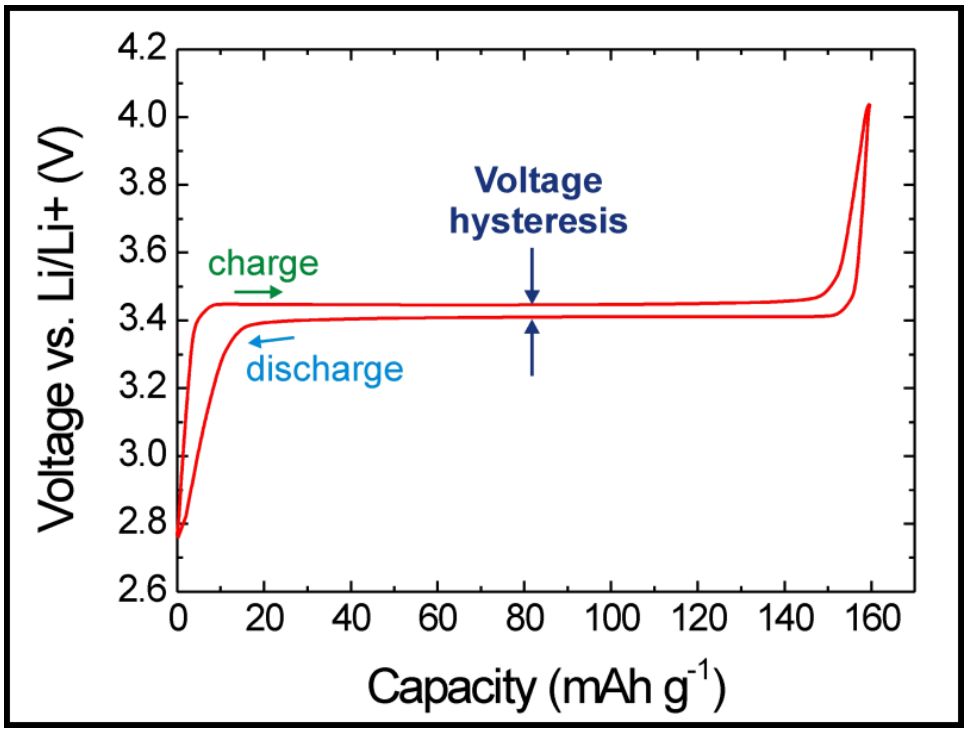

Figure 1.4 Typical galvanostatic charge/discharge curve for a $LiFePO_4$ material at a rate of C/20. Reprinted with permission from W. Dreyer, J. Jamnik, C. Guhlke, R. Huth, J. Moškon, and M. Gaberšček, Nature Materials, 9, 448, 2010.[4] Copyright 2010 Nature Materials.

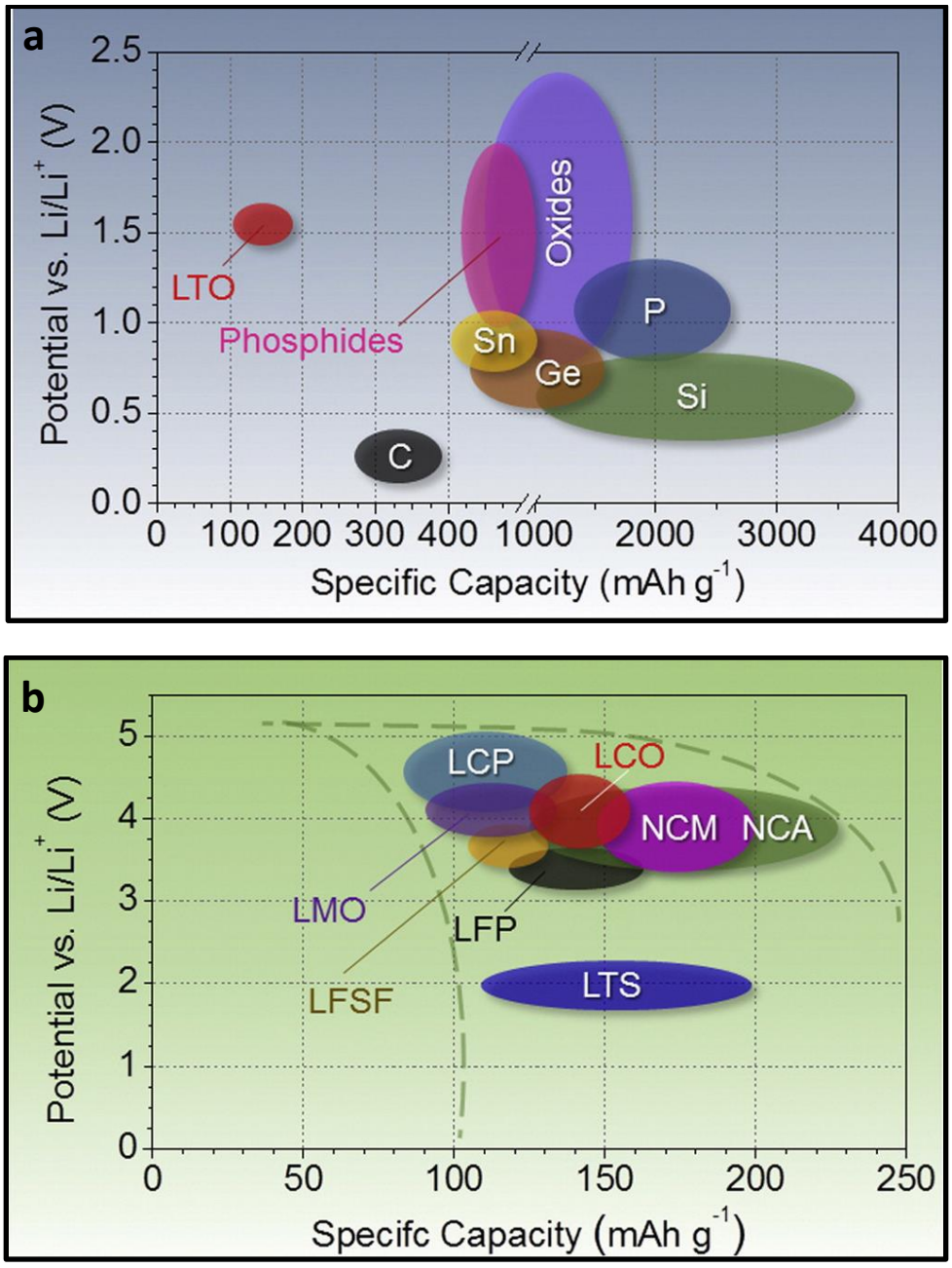

Figure 1.5 Approximate ranges of average discharge potentials and specific capacity of some of the most common (a) negative electrode and (b) positive electrode materials. Reprinted with permission from N. Nitta, F. Wu, J. T. Lee, and G. Yushin, Materials Today, 18, 252, 2015.[5] Copyright 2015 Materials Today.

1.5 References

1. J. M. Tarascon and M. Armand, *Nature*, **414**, 359 (2001).

2. V. Srinivasan, *AIP Conference Proceedings*, 283 (2008).

3. T. Nagaura, A lithium-ion battery, in The Third International Rechargeable Battery Seminar, Deerfield Beach, FL (March 5-7, 1990).

4. W. Dreyer, J. Jamnik, C. Guhlke, R. Huth, J. Moškon, and M. Gaberšček, *Nat. Mater*., **9**, 448 (2010).

5. N. Nitta, F. Wu, J. T. Lee, and G. Yushin, *Mater. Today*, **18**, 252 (2015).

6. J. Steiger, *Ph.D. Dissertation*, Karlsruher Institut für Technologie (KIT), Karlsruhe (2015).

7. W. J. Zhang, *J. Power Sources*, **196**, 13 (2011).

8. M. Winter and J. O. Besenhard, *Electrochim. Acta*, **45**, 31 (1999).

9. U. Kasavajjula, C. Wang, and A.J. Appleby, *J. Power Sources*, **163**, 1003 (2007).

10. H. Wu and Y. Cui, *Nano Today*, **7**, 414 (2010).

11. Z. P. Guo, J. Z. Wang, H. K. Liu, and S. X. Dou, *J. Power Sources*, **146**, 448 (2005).

12. J. P. Maranchi, A. F. Hepp, and P. N. Kumta, *Electrochem. Solid-State Lett.*, **6**, A198 (2003).

13. C. K. Chan, H. Peng, G. Liu, K. McIlwrath, X. F. Zhang, R. A. Huggins, and Y. Cui, *Nature nanotech.*, **3**, 31 (2007).

14. T. Song, J. Xia, J. H. Lee, D. H. Lee, M. S. Kwon, J. M. Choi, J. Wu, S. K. Doo, H. Chang, W. I. Park, D. S. Zang, H. Kim, Y. Huang, K.C. Hwang, J. A. Rogers, and U. Paik, *Nano Lett*., **10**, 1710 (2010).

15. M. Thakur, M. Isaacson, S. L. Sinsabaugh, M. S. Wong, and S. L. Biswal, *J. Power Sources*, **205**, 426 (2012).

16. M. Jagannathan, *Ph.D. Dissertation*, University of Utah (2013).

17. H. C. Shin, J. A. Corno, J. L. Gole, and M. Liu, *J. Power Sources*, **139**, 314 (2005).

18. D. Kang, J. A. Corno, J. L. Gole, and H. Shin, *J. Electrochem. Soc.*, **155**, A276 (2008).

19. M. R. Zamfir, H. T. Nguyen, E. Moyen, Y. H Lee, and D. Pribat, *J. Mater. Chem. A*, **1**, 9566 (2013).

20. S. Ohara, J. Suzuki, K. Sekine, and T. Takamura, *J. Power Sources*, **136**, 303 (2004).

21. M. J. Sailor, *Porous Silicon in Practice*, Wiley-VCH, Weinheim, Germany (2012).

22. J. B. Goodenough and Y. Kim, *Chem. Mater*., **22**, 587 (2010).

23. M. Tang, W. C. Carter, and Y.M. Chiang, *Ann. Rev. Mater. Res*., **40**, 501 (2010).

24. S. Mukerjee, T. R. Thurston, N. M. Jisrawi, X. Q. Yang, J. McBreen, M. L. Daroux, and X. K. Xiang, *J. Electrochem. Soc*., **145**, 466 (1998).

25. R. Pvnn, Neutron Scattering a Primer, *Los Alamos Science*, p. 2, Summer 1990.

26. G. E. Bacon, *Neutron Diffraction*, p. 38, Clarendon Press, Oxford (1975).

CHAPTER 2

LITERATURE REVIEW

.

2.1 Neutron Diffraction Studies on Li-ion Batteries

Neutron Diffraction (ND) study of Li-ion batteries (LIBs) involves interaction of neutrons with various active and nonactive battery components like electrodes, binders, current collectors, separator, liquid electrolyte, and casing material. Neutrons interact with matter by two means—coherent scattering that gives Bragg reflections, and incoherent scattering that gives rise to the background noise in the ND pattern.[1,2] The Bragg reflections arise from the electrode phases, binder, current collector, and casing material. The background contribution predominantly arises from the components (separator, liquid electrolyte, casing pouch material) that have poor or no degree of crystallinity. But the background in the ND pattern masks the weak Bragg reflections from dilute and weakly diffracting phases. The subsequent analysis of the ND pattern by Rietveld refinement, for the extraction of structural parameters, demands Bragg reflections with high signal-to-noise ratio.

ND patterns with Bragg reflections of higher counts can be obtained by using incident neutrons of higher flux, detectors covering a wide solid angle range, higher data collection times, and higher sample volume. While the former two are fixed for an instrument, the later two can be controlled by the experimenter. The usage of higher data collection times demands confinement to low C-rate discharge/charge experiments or State of Charge (SOC) experiments. But the sequence of phase transitions occurring in SOC and constant C-rate experiments are different, thereby preventing us from understanding the functioning of a battery in real time. For example, $LiCoO_2$ was found to undergo a first order phase transition when delithiated continuously[3] and this was not the case when delithiated at a particular SOC.[4,5,6] Earlier work on ND studies in LIBs

used thicker electrodes, as they give better counts due to higher sample volume, but have had issues with electrochemistry. The issues with electrochemistry of thicker electrodes and ways to overcome will discussed in detail later.

ND patterns with low background can be obtained by using a deuterated electrolyte and hydrogen-free cell components like a binder or separator. The electrolyte in a battery contributes significantly to the background as it's a liquid (has no definite crystal structure) and has H which scatters incoherently. It was found that 1 ml of hydrogenated electrolyte added to 1 g of MoS_2 gives no features of MoS_2 in the ND pattern.[7] Very recent work by Pang et al.[8] has shown that glass-fiber separators, PVDF separators, and polypropylene Celgard separators produce low to high background, respectively. The use of casing materials containing no/low hydrogen and no non-crystalline substances like glass/quartz,[9,10] $Ti_{0.68}Zr_{0.32}$,[11] Al,[12] V,[13,14] and Si[15] were found to be very effective. Additionally, it's better if the casing material gives no Bragg reflections at all (e.g., amorphous Si) or gives Bragg reflections that don't overlap with electrode phase reflections. Al has nearly zero incoherent cross-section and so gives nearly as little background as air (Figure 2.1).[16] However, Rietveld refinement by incorporating Al (sheet), which has strong multidirectional texture due to rolling, is very challenging. Textured casing material may need to be incorporated into the computational model as two phases with one direction at a time, which might affect the goodness of fit χ^2. The reduction in background is essential to improve the signal-to-noise ratio, as reducing the background by half has the same effect as doubling the counting time.

As the background affects the phase transition study significantly, it is very important to understand the background contribution by different materials. $Ti_{0.68}Zr_{0.32}$[17] alloy

produces no Bragg reflections due to balancing the negative coherent scattering length of Ti with the positive coherent scattering length of Zr, averaging the net scattering length of alloy to zero. But it produces significant background in the ND pattern.[16] Vanadium scatters isotropically, producing no Bragg reflections but a very broad background.[16] The background from the $Ti_{0.68}Zr0_{.32}$ and V are similar (Figure 2.2),[16] but V is more easily available in the market in various shapes, whereas $Ti_{0.68}Zr_{0.32}$ needs to be special ordered from specific companies. The background contribution by quartz due to a lack of long range crystallinity is significantly high compared to V or Al (Figure 2.1).[16] Si is another material that gives nearly zero background (due to nearly zero incoherent neutron cross-section), which is less compared to V (Figure 2.3).[16] Electronic grade Si, abundantly available in the market in the form of single crystal wafers, is very cheap and doesn't show any chemical reaction with electrolyte.

2.2 Neutron Friendly In-Situ Cell Designs

The in-situ electrochemical cells for ND reported in the literature (Table 2.1) can be broadly classified into two categories, those using thicker electrodes and those using thinner electrodes, to obtain better signal-to-noise ratio.

2.2.1 In-Situ Cells Using Thicker Electrodes

2.2.1.1 Cylindrical In-Situ Cells With Pyrex Glass Casing

The first publication on in-situ electrochemical cell design (Figure 2.4) for ND studies in LIBs appears to be that of Bergstom et al.[18] They used a cylindrical pyrex glass cell and studied the phase transitions in a $LiMn_2O_4$/Li half-cell. Pyrex glass was probably

chosen as it gives very low background and can be added as an additional function in the Rietveld refinement. The circular geometry ensures a constant path length for the diffracted beam moving towards the detector.

The in-situ cell consists of a 10 mm diameter quartz glass (0.5 mm thick) tube lined inside with ~100 nm gold layer. Li rod of 2 mm diameter was used as the negative electrode and placed at the center of the tube. The Li electrode was coated with a thin polymer electrolyte layer which was surrounded by the Celgard separator soaked in liquid electrolyte. The space in between the separator and the glass tube was filled with $LiMn_2O_4$ mixed with electrolyte. ND pattern of the cell showed well resolved $LiMn_2O_4$ phase Bragg reflections, despite background from the pyrex glass, Li, and electrolyte. The cell was charged at 4 V till the composition of $Li_{0.84}Mn_2O_4$ was attained, which was calculated based upon the charge passed, and the ND pattern was collected. The ND pattern was refined using Rietveld refinement for lattice parameter and Li occupancy. The results obtained were in close agreement with the calculated values, which proves the ability of the cell to track phase transitions. But an 8 mm thick $LiMn_2O_4$ electrode was used to maintain the large sample volume, and thus impractical, very low C-rates.

Berg et al.[19] have modified the above cell design and studied phase transitions in $LiMn_2O_4$/Li half-cell again (Figure 2.5). The inside of the pyrex tube was lined with Li foil, making it a negative electrode. Li foil was surrounded by a Celgard separator soaked in 1 M solution of $LiBF_4$ in 2:1 EC:DMC. The interior of tube was filled with $LiMn_2O_4$+Carbon black mixture, making it the positive electrode. The pyrex glass tube was sealed with brass plugs to ensure air and moisture tightness. ND patterns were collected at various SOC—uncharged, 4 V, 4.05 V, 4.10 V, 4.12 V, 4.16 V, and 4.24 V.

The Li content found from occupancy refinement and the amount of charge passed were found to be in close agreement. But a thicker $LiMn_2O_4$ electrode was used to maintain more sample volume, which led to problems like large overpotentials and use of C-rates as low as C/750. The use of thicker electrode increases the path length for electrons passing from the current collector, resulting in higher ohmic resistance that manifests as overpotential. Due to the thicker electrode, the surface composition of $LiMn_2O_4$ is much different from the bulk, which leads to unresolvable peaks in the ND pattern.

2.2.1.2 Coin Type In-Situ Coin Cell With Al Casing

In the work of Rosciano et al.,[20] the coin cell was made out of PEEK (Figure 2.6). The electrodes, separated by separator, were held under mechanical pressure to ensure intimate contact by using an Al piston by pressing against an Al sample holder, loaded under spring pressure. The neutron beam enters the cell through the 500 μm thick Al window in the front, interacts with the electrode volume, and then exits through the Al current collector in the bottom. The advantage of choosing Al is that it gives negligible background due to its nearly zero incoherent scattering cross-section. In-situ half-cell experiments were conducted using $LiNiO_2$ and $Li_{1.1}(Ni_{1/3}Mn_{1/3}Co_{1/3})_{0.9}O_2$ as positive electrodes against the negative Li electrode. The active material-to-carbon ratio was not good enough to get intense reflections for $Li_{1.1}(Ni_{1/3}Mn_{1/3}Co_{1/3})_{0.9}O_2$. However, the change in the (003) peak position at different SOC could be tracked. However, an overpotential of ~120 mV was observed, despite the low C-rate (C/50).

The performance of the cell was further improved by Colin et al.[21] engineering the electrode architecture in two ways. First, the uniform bulk current distribution in the

electrode material from the current collector was ensured by dividing the thickness into three layers. The graphite content in the layer away from the current collector was maintained at a high level to ensure better electronic conductivity. This was expected to minimize the overpotential. Second, the porous network in the electrode material was improved to ensure better wetting of electrode particles by electrolyte, by burning a mixture of electrode mass and NH_4CO_3 under vacuum at 150 °C. The phase transitions in the architectured $Li(Li_{1/3}Ti_{5/3})O_4$ electrode were studied during charging and discharging. The diffraction peaks were far better than that obtained in the former work.[20]

2.2.2 In-Situ Cells Using Thinner Electrodes

2.2.2.1 Cylindrical Roll-Over Cell With V Casing

The chief goal of the cell designed by Sharma al.[7] was to use thin electrodes, but still maintain a higher sample volume, so as to avoid the issues concerned with polarization that causes overpotential. This was accomplished by stacking and rolling layers of Separator, Cu with a $MoS_2/Li(Li_{1/3}Ti_{5/3})O_4$ electrode, Separator, Li metal into a bundle and inserting it into a Vanadium can (Figure 2.7). V was used as it gives a very low background. The background from the cell was further minimized by using a minimal amount of deuterated electrolyte. The cell can be used to collect data continuously unlike the cells discussed before, enabling monitoring the real time phase transitions. The data statistics were so good that data collected over 5 min could be binned into one pattern for Rietveld refinement, whereas it was 9 hrs in the previous work. The use of a high flux neutron diffractometer with area detectors gave an added advantage.

2.2.2.2 Cylindrical In-Situ Cell With Ti-Zr Casing

This is the first work[22] to present an in-situ cell that gives Bragg reflections from electrode material (powder form) alone and not from any other battery components (Figure 2.8). The null matrix $Ti_{0.68}Zr_{0.32}$ alloy was used as casing material as it gives no Bragg peak. The electrochemical performance of the cell was tested using $Li_{1.1}Mn_{1.9}O_4$ and $LiFePO_4$ electrode materials. The cell was successfully used to demonstrate real time phase transitions during delithiation of $LiFePO_4$. Rietveld refinement could be performed to extract as many as 15 structural parameters from neutron data collected over a 60-min period. Structural changes sensitive to 0.042 Li removal were detected.

2.2.2.3 Cylindrical In-Situ Cell With Al and Quartz Casing

The cell by Roberts et al.[12] consists of wound layers of cathode, separator, and anode stacked and inserted into an Al/quartz cylindrical can (Figure 2.9). The background in ND was minimized by replacing hydrogen components with hydrogen-free equivalents. The effects of a PTFE binder instead of PVDF, deuterated electrolyte instead of hydrogenated electrolyte, Al casing instead of quartz, and quartz glass fiber separator instead of Celgard, were investigated (Table 2.2). The phase transitions in the $LiFePO_4$/Li half-cell were investigated for proof of concept studies. Cell 1 was found to give huge background with no Bragg reflections due to the large hydrogen content. The use of H free components in Cell 2 resulted in ND patterns with Bragg reflections over significant background. The neutron data collected on uncharged LIB over a period of 15 h was Rietveld refinable. The cell was successfully used to track phase transitions, as $LiFePO_4$ transforms to $FePO_4$ during charging. When Cell 2 was modified by using fluorinated

electrolyte (Cell 3), no improvement in the ND pattern was observed. The signal-to-noise ratio in Cell 3 was further improved in Cell 4 by replacing quartz with Al. The ND pattern of high signal-to-noise ratio was obtained. The lattice parameters and atomic positions could be refined using Rietveld refinement.

2.2.2.4 Prismatic In-Situ Cell With Si (100) Casing

In the work of Vadlamani et al.,[15] authors designed and constructed a novel electrochemical cell for in-situ ND experiments that was used to study the phase transitions in both electrodes (anode/cathode) simultaneously using minimal electrode volumes. The cell used (100) oriented single crystal Si sheets, eliminating the multiple reflections casing and reducing the background scattering. Single crystal Si was chosen because it has a low incoherent scattering cross-section. It produces a significantly lower background compared to V, Ti-Zr null matrix alloy, or glass.

The designed cell was validated by relooking the phase transitions in the well-established graphite/$LiCoO_2$ and graphite/$LiMn_2O_4$ cells with just two electrode layers (~100 μm each). The diffraction patterns were analyzed using Rietveld refinement, with $\chi^2 < 8.2$. The trends in the lattice parameters and unit cell volume were observed. The cell facilitated detection of the intricate features, like first order phase transitions in $LiCoO_2$.

2.3 Si as an Electrode

Si is a promising electrode material for high performance Li-ion batteries due to its exceptional specific capacity of 3580 mAh/g, which is more than ten times higher than conventional graphite, C-based anodes.[23] During the insertion of Li^+ into the Si lattice,

phase transitions are induced, which results in ~300% volumetric expansion in the Si lattice. The huge strain in the Si lattice results in plastic deformation,[24] pulverization of powder electrodes, and ultimately, capacity fading.[25,26] The proper architecting of a Si electrode is necessary to overcome the electrode cycling issues. Of late, these issues have been addressed by architecting the electrode in the form of thin films,[27] nano wires,[28] core-shell nano wires,[29] nano tubes,[30] nano particles,[31] and nano composites.[32] The use of nano particles offers better performance—due to shorter Li diffusion lengths, lower over-potentials due to the high surface area, and improved fracture resistance.[33] Our earlier work showed that microfabricated columnar Si (100) electrodes, prepared by the cheaper electrochemical etching route, exhibit very large reversible capacities.[34]

2.4 Electrochemical Etching of Si

Electrochemical etching can be used to fabricate a wide variety of microporous structures, from an irregular shape such as a sponge, to perfectly cylindrical shapes, with pore diameter/spacing ranging from 1 nm to a few μm. The pore diameter, spacing, morphology (smooth, branched, faceted), and orientation, and the interaction between pores are dependent on some key experimental parameters. The parameters include current density, electrolyte composition and homogeneity, light direction and intensity (n-type Si), and temperature. Based on the pore dimension, IUPAC distinguishes pores into micropores (<2 nm), mesopores (2-50 nm), and macropores (>50 nm). The pore formation in Si occurs only under a combination of specific parameters. For example, a macroporous structure using acetonitrile, propylene carbonate and propylene carbonate electrolyte, is observed only if resistivity of Si exceeds ~10 Ω-cm for both (100) and

(111); whereas dimethylformamide can be formed using ~1 Ω-cm of Si.[35] While mesoporous and macroporous Si are very well suited for the Li-ion battery application, microporous Si is not. Apart from pores, nano wires can also be formed using metal assisted etching.[36] The relationship between morphology, formation mechanism, and Si doping is summarized in Table 2.3. The salient features of electrochemical etching in Si are:

- In highly doped p-type Si, as current density increases the pore size increases.[37]
- In p-type Si, as dopant concentration increases, the macropore surface density increases.[38]
- As resistivity increases, the macropore surface porosity decreases; whereas pore diameter and etching rate increases.
- The macropore etching rate increases with current density.[39]
- In photoluminescent n-type Si, macropore diameter in pore propagation direction can be controlled by light intensity.[40]

2.5 Phase Transitions During Lithiation/Delithiation of Si

The phase transitions during lithiation/delithiation of Si at room temperature have been studied in the past using Si powders, [41,42,43,44] Si thin films,[41,45] and Si nano wires.[46,47] The evolution of various phases during lithiation of Si may be understood from the Li-Si equilibrium phase diagram. The Li-Si equilibrium phase diagram[48] (Figure 2.10) shows four equilibrium phases, namely $Li_{12}Si_7$, Li_7Si_3, $Li_{13}Si_4$, and $Li_{22}Si_5$. The room temperature voltage-capacity profile during Si lithiation must therefore show a stepped profile with four plateaus corresponding to the equilibrium between phases. Surprisingly,

the stepped potential was only observed at a high temperature (415 ºC) but not at room temperature (Figure 2.11). The equilibrium EMF data with respect to Li for the liquid system[49] at 415 ºC and solid system at room temperature[50] is presented in Table 2.4.

The real time phase transitions occurring during room temperature lithiation/delithiation of Si was studied by Li et al.[44] using X-Ray diffraction (Figure 2.12). The first lithiation of Si resulted in a single plateau (Figure 2.12a) that gently slopes downwards, indicating the two phase coexistence of c-Si+a-Li_xSi phase. The amorphous phase in coexistence with Si was found to be ~$Li_{3.5}Si$. There seems to be no proper agreement on the value of x in the literature. The value of x was found to be 2.17 by Limthongkul et al.,[41] 2.9 by Danet et al.,[51] and 3.4 by Key et al.[52] Upon further lithiation, as the voltage drops below 60 mV, the formation of c-$Li_{3.75}Si$ occurred but not $Li_{4.4}Si$, which had been expected as per the phase diagram. The formation of c-$Li_{3.75}Si$ from a-$Li_{3.75}Si$ was reported to be a spontaneous and congruent transformation that is solely controlled by the lithium concentration in the a-LixSi, involving neither large-scale atomic migration nor phase separation.[53] Using DFT calculations it was established that c-$Li_{15}Si_4$ formation is favored over other possible crystalline phases due to the similarity in its electronic structure with a-$Li_{3.75}Si$. This is due to the slower kinetics of lithiation.

The voltage profile of the first delithiation of lithiated Si shows a curve with a single plateau (Figure 2.12b). The plateau is an indication of the coexistence of $Li_{15}Si_4$ and a-Li_ySi (y~2) phases. The voltage raises after the plateau, once the $Li_{15}Si_4$ phase dissolves, and the further delithiation of a-Li_2Si results in the formation of a-Li_tSi ($0<t<2$). The second lithiation cycle indicates no plateau indicative of the presence of a single phase

(Figure 2.12c). The phase diagram constructed based on the information obtained from electrochemical studies and an XRD studies is shown in Figure 2.12d.

Table 2.1. Review of the electrochemical cell designs mentioning various cell components.

Type of Cell	**Casing Material**	**Electrodes**		**Separator**	**Electrolyte**	**Ref**
		Positive	**Negative**			
Cylindrical	Pyrex	$LiMn_2O_4$ (8 mm)	Lithium	Celgard	liquid	10
Cylindrical	Pyrex	$LiMn_2O_4$	Lithium	Celgard	1 M $LiBF_4$ in 2:1 EC:DMC	9
Coin cell type	PEEK	$LiNiO_2$,(5mm), $Li_{1.1}(Ni_{1/3}Mn_{1/3}Co_{1/3})_{0.9}O_2$ (5 mm)	Lithium	Glass fiber	1 M $LiPF_6$ in 1:1 wt% EC:DMC	20
Cylindrical	Vanadium	MoS_2, $Li(Li_{1/3}Ti_{5/3})O_4$	Lithium	Celgard	1 M $LiPF_6$ in 1:1 vol% deuterated EC:DMC	7
Cylindrical	$Ti_{0.68}Zr_{0.32}$	$LiFePO_4$ (~1 mm)	Lithium	Glass fiber	1 M $LiPF_6$ in 1:1 vol% deuterated EC:DMC	11
Cylindrical	Vanadium	$LiFePO_4$ (few µm)	Lithium	Celgard	1 M $LiPF_6$ in 1:1 vol% deuterated EC:DMC	14
Coin cell type	Si (100)	$LiCoO_2$, $LiMn_2O_4$ (~100 µm each)	Graphite (~100 µm)	Celard	1 M $LiPF_6$ in 1:1 of EC:DMC	15

Table 2.2. Summary of cells prepared for testing and the approximate sample mass and hydrogen percentages for the various designs.

Cell Type	**Cathode**	**Separator and Electrolyte**	**Anode**	**Packaging**	**Mass of $LiFePO_4$**	**Mass of $LiFePO_4$**	**Mass of % H**	**Atomic % $LiFePO_4$**	**Atomic % H**
Cylindrical	LiFePO4, Carbon, PVDF binder on Al foil	Polypropylene soaked in conventional electrolyte	Lithium metal	Polypropylene/ Aluminum coffee bag	~ 1 g	~ 13	~ 5.4	~ 5.4	~ 40
Coin cell type	LiFePO4, Carbon, PTFE binder on Al Mesh	Quartz glass fiber soaked in deuterated electrolyte	Lithium metal	Quartz glass tube	~ 1 g	~ 13	~ 0	~7	~ 0
Cylindrical	LiFePO4, Carbon, PTFE binder on Al Mesh	Quartz glass fiber soaked in flourinated electrolyte	Lithium metal	Quartz glass tube	~ 1 g	~ 13	~ 1.5	~ 7	~ 24
Cylindrical	LiFePO4, Carbon, PTFE binder on Al Mesh	Quartz glass fiber soaked in deuterated electrolyte	Lithium metal	Aluminum glass tube	~ 1 g	~ 13	~ 0	~ 7	~ 0

Table 2.3. The relationship between morphology, formation mechanism, and Si doping.

Morphology	**Silicon type**	**Mechanism**
Micropores (<2 nm)	p	Crystallographic face selectivity, enhanced electric field, tunneling, quantum confinement
Mesopores (2-50) nm	p+(0.1-0.01Ω-cm), p++(≤0.01-0.001Ω-cm), n+	Enhanced electric field, tunneling
Macropores (>50 nm)	n	Space-charge limited
Macropores (>50 nm)	n	photoexcitation
Nanowire	p	Metal assisted etching

Table 2.4. Equilibrium potentials for various phases at RT and 415 ºC.

Phases in Equilibrium	**EMF (mV vs Li)**	
	RT	**415 ºC**
Si-$Li_{12}Si_7$	582	332
$Li_{12}Si_7$-Li_7Si_3	520	288
Li_7Si_3-$Li_{13}Si_4$	428	158
$Li_{13}Si_4$-$Li_{21}Si_5$	300	44

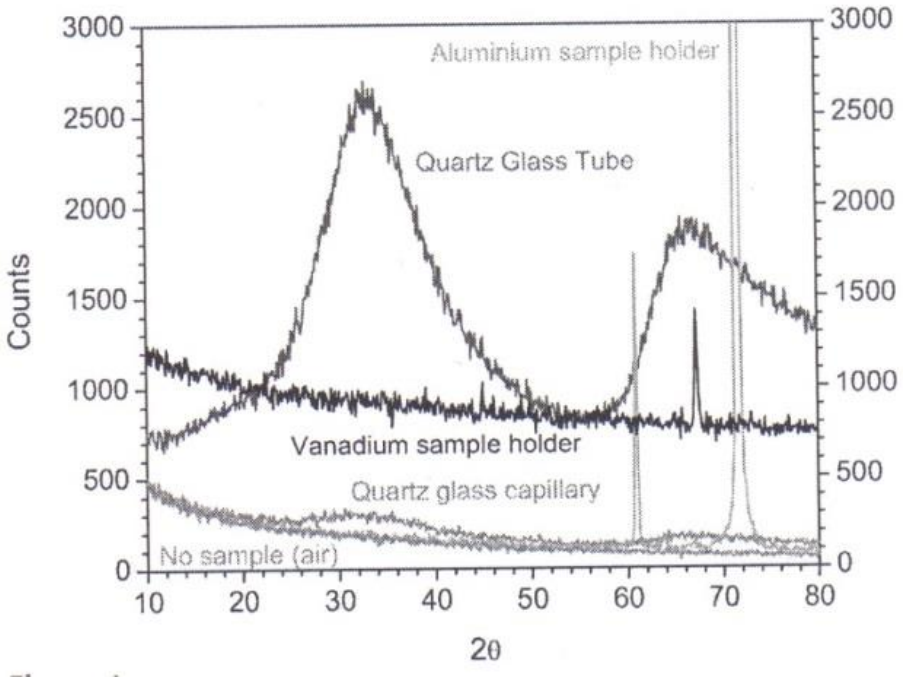

Figure 2.1 Neutron diffraction patterns of Al, V, air, quartz capillary (0.01 mm wall thickness), and quartz tube (8 mm-OD, 1mm wall thickness) collected at 2.37 A˚. It can be noticed that Al and air have similar background.[16] Reproduced with permission of the International Union of Crystallography.

(https://doi.org/10.1107/S0021889807011387)

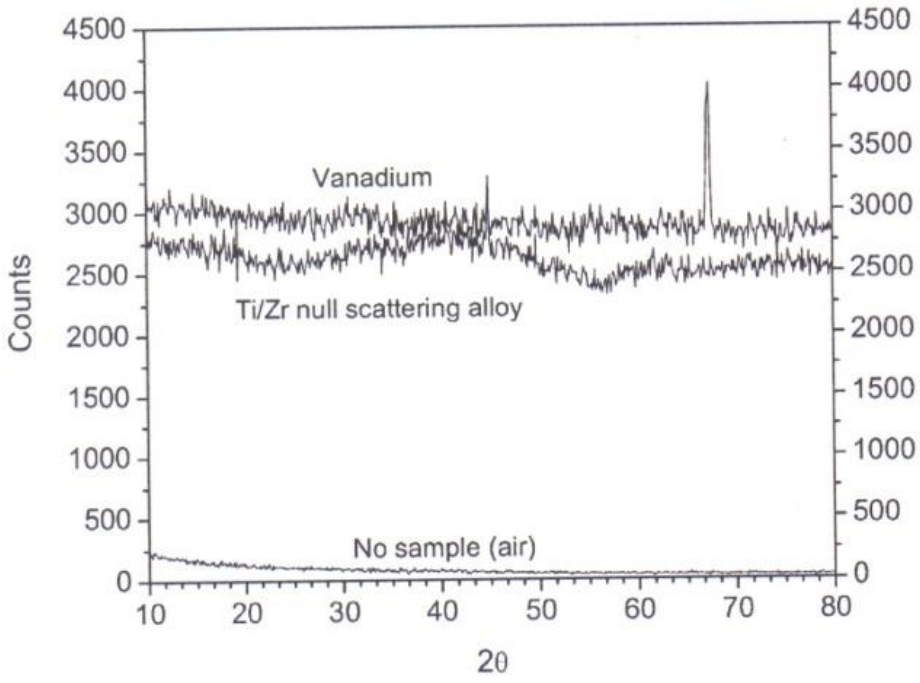

Figure 2.2 Neutron diffraction patterns of V, Ti/Zr null matrix alloy, and air at 2.37 A˚. It can be noticed that TiZr and V have similar background. Vanadium yields a flatter background, but contributes a weak Bragg peak at 2θ = 68°.[16] Reproduced with permission of the International Union of Crystallography. (https://doi.org/10.1107/S0021889807011387)

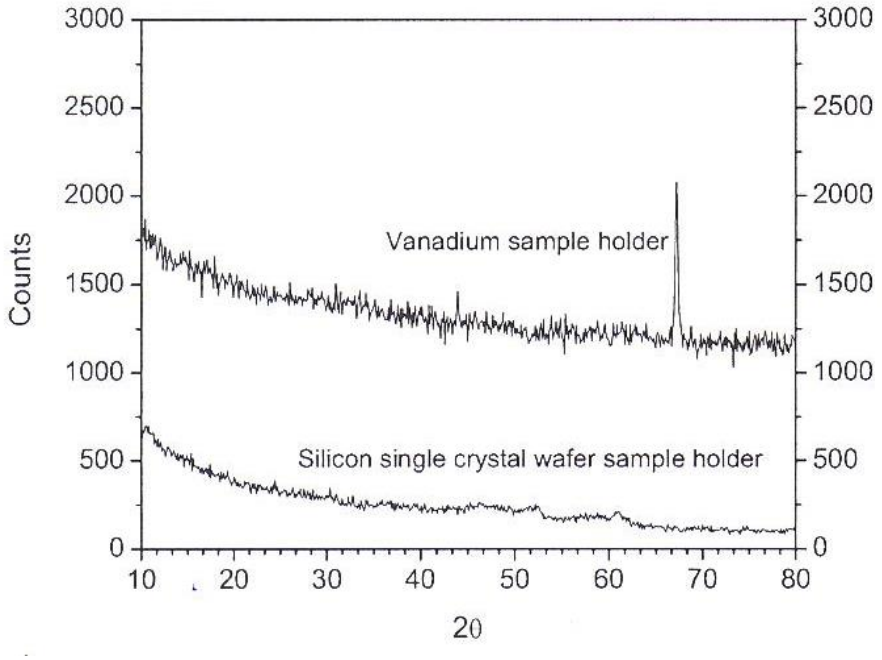

Figure 2.3 Neutron diffraction patterns of V and single crystal Si. Single crystal Si shows much less background than V.[16] Reproduced with permission of the International Union of Crystallography. (https://doi.org/10.1107/S0021889807011387)

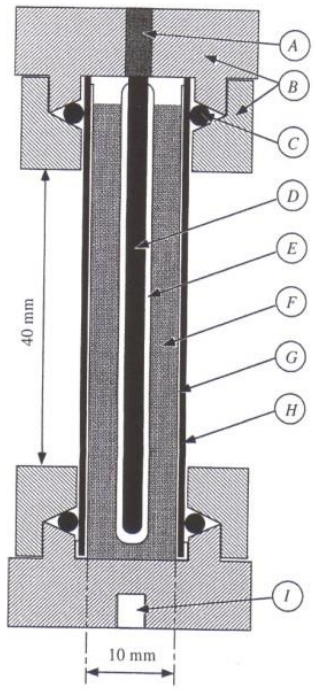

Figure 2.4 A cell for in situ neutron diffraction studies of lithium-ion insertion/extraction processes in polycrystalline electrode materials. (A) Seal for the lithium anode; (B) brass collars; (C) NBR O ring; (D) lithium anode (diameter 2 mm); (E) solid polymer electrolyte and mechanical separator (thickness 1 mm); (F) mixture of $LiMn_2O_4$, electrolyte, and carbon black; (G) gold layer, thickness 100 nm; (H) Pyrex tube, wall thickness 0.5 mm; (I) connector to neutron powder diffractometer.[18] Reproduced with permission of the International Union of Crystallography. (https://doi.org/10.1107/S002188989800538X)

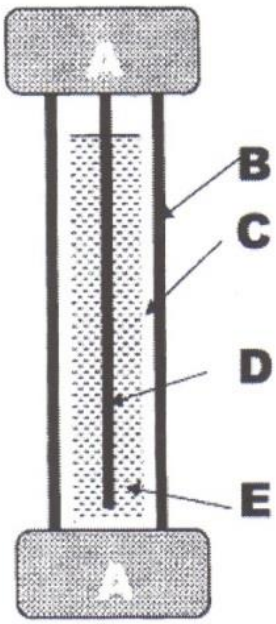

Figure 2.5 A schematic representation of the cell used for in-situ neutron diffraction studies: (A) brass plugs; (B) Pyrex© tube lined with lithium foil; (C) separator soaked in electrolyte; (D) current collector; (E) mixture of $LiMn_2O_4$, electrolyte, and carbon black.[19] Reprinted with permission from H. Berg, H. Rundlöv, and J. O. Thomas, Solid State Ionics, 144, 65, 2001.[19] Copyright 2001 Solid State Ionics.

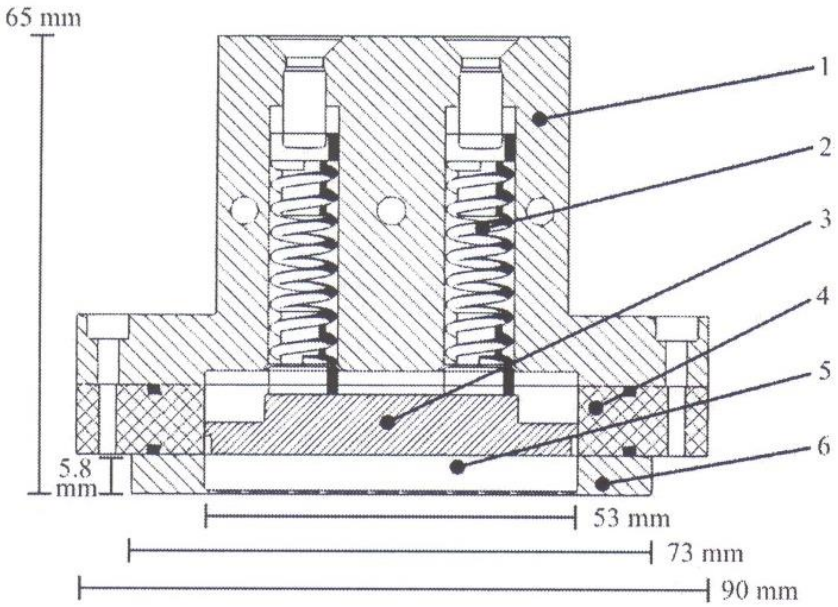

Figure 2.6 Cross section of the assembled device: (1) cell top, (2) spring with piston, (3) negative current collector, (4) cell body, (5) compartment for the active material and entry window for neutrons, (6) positive current collector.[20] Reproduced with permission of the International Union of Crystallography.

(https://doi.org/10.1107/S0021889808018025)

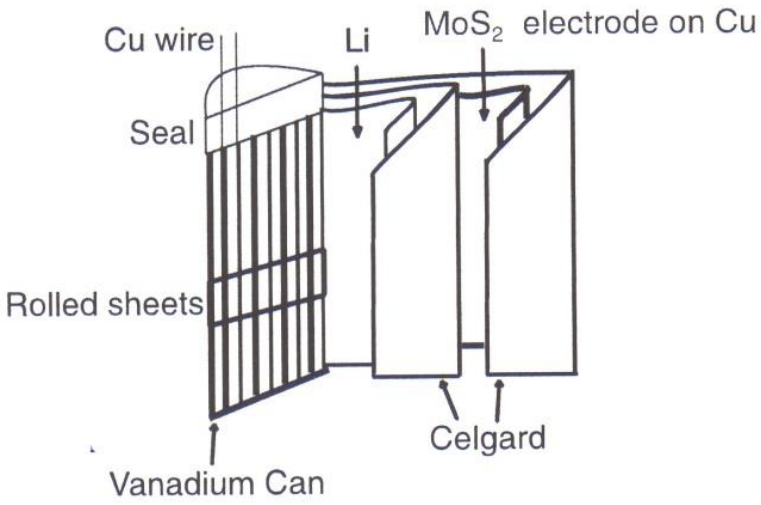

Figure 2.7 A schematic of a section through the "roll-over" cell for in-situ neutron diffraction studies. Sheets of Celgard® (white), MoS_2 electrode on Cu (red), Celgard, and Li (blue), are rolled and sealed inside a vanadium can (green). The can is sealed in an argon-filled glovebox. Reprinted with permission from N. Sharma, G. Du, A. J. Studer, Z. Guo, and V. K. Peterson, Solid State Ionics, 37, 199, 2011.[7] Copyright 2011 Solid State Ionics.

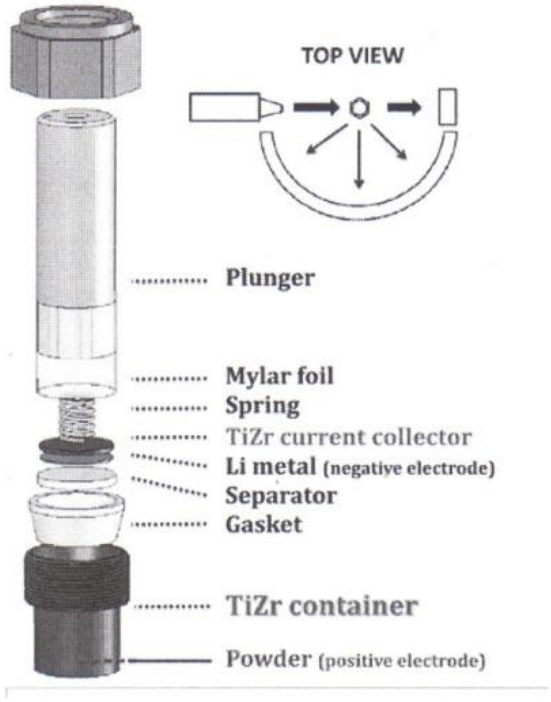

Figure 2.8 Description of the electrochemical cell designed for in-situ or *operando* neutron diffraction. Reprinted with permission from M. Roberts, J. J. Biendicho, S. Hull, P. Beran, T. Gustafsson, G. Svensson, K. Edström, Journal of Power Sources, 226, 249, 2013.[22] Copyright 2013 Journal of Power Sources.

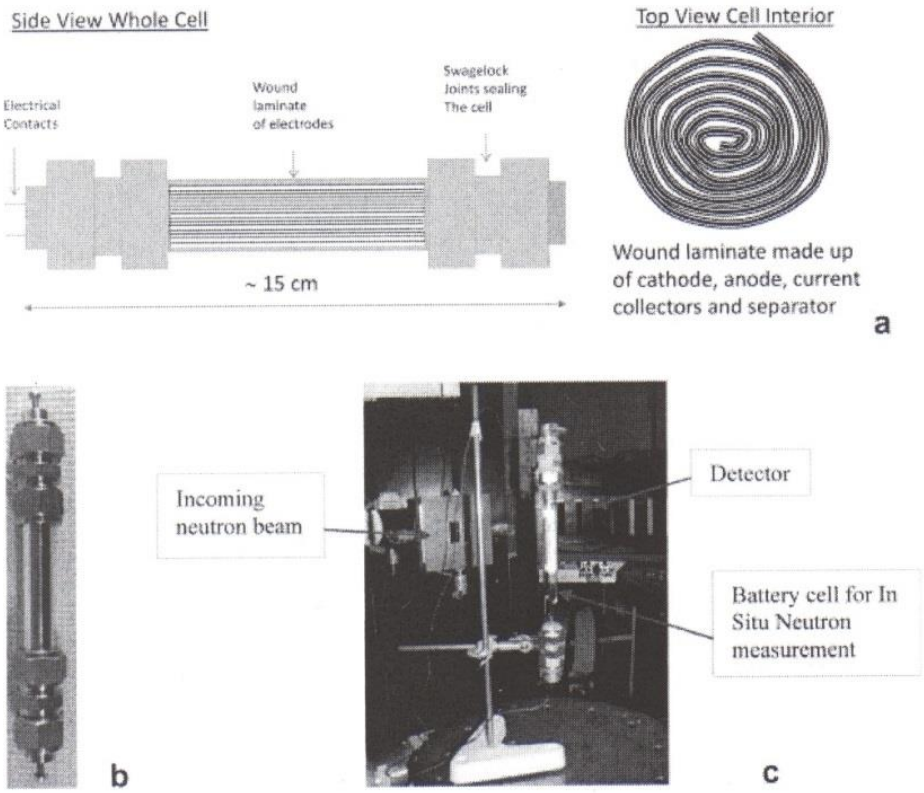

Figure 2.9 Images of the battery cell for in-situ neutron diffraction measurement. (a) A schematic of the battery cell. (b) A photo of the diffraction setup sealed in aluminium tube (Cell 4). (c) A photo of the cell design and placement on the diffraction instrument goniometer (Cell 2). Reprinted with permission from M. Roberts, J. J. Biendicho, S. Hull, P. Beran, T. Gustafsson, G. Svensson, and K. Edstrom, Journal of Power Sources, 226, 249, 2013.[12] Copyright 2013 Journal of Power Sources.

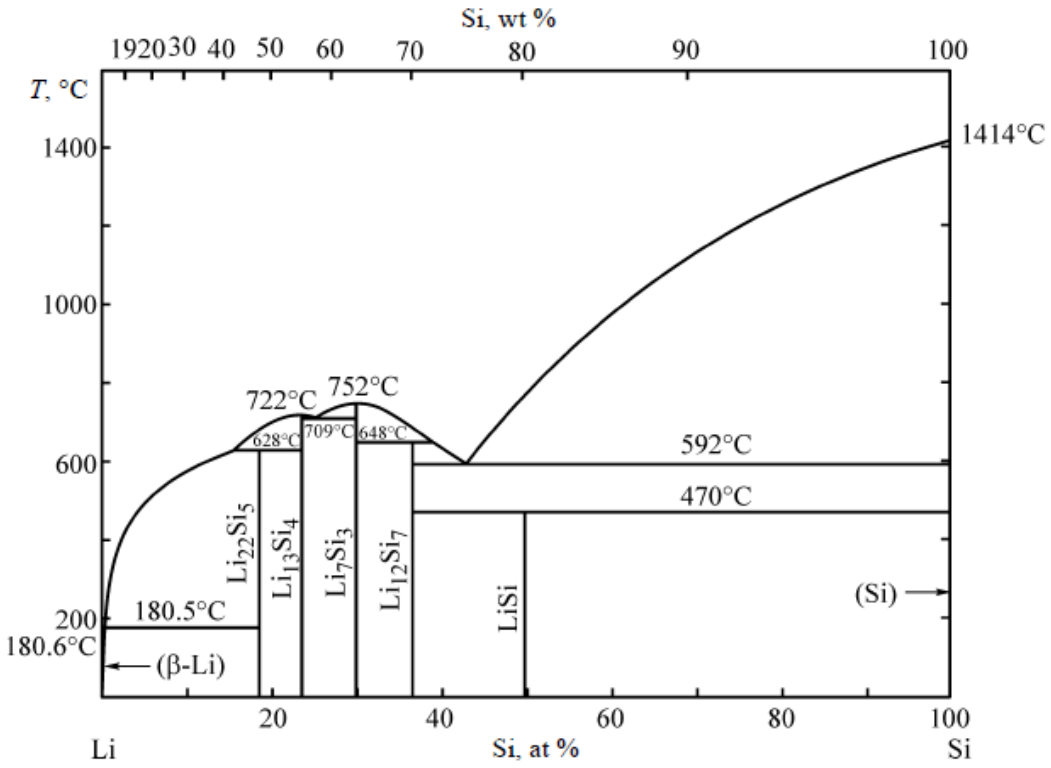

Figure 2.10 Li-Si phase diagram.[48]

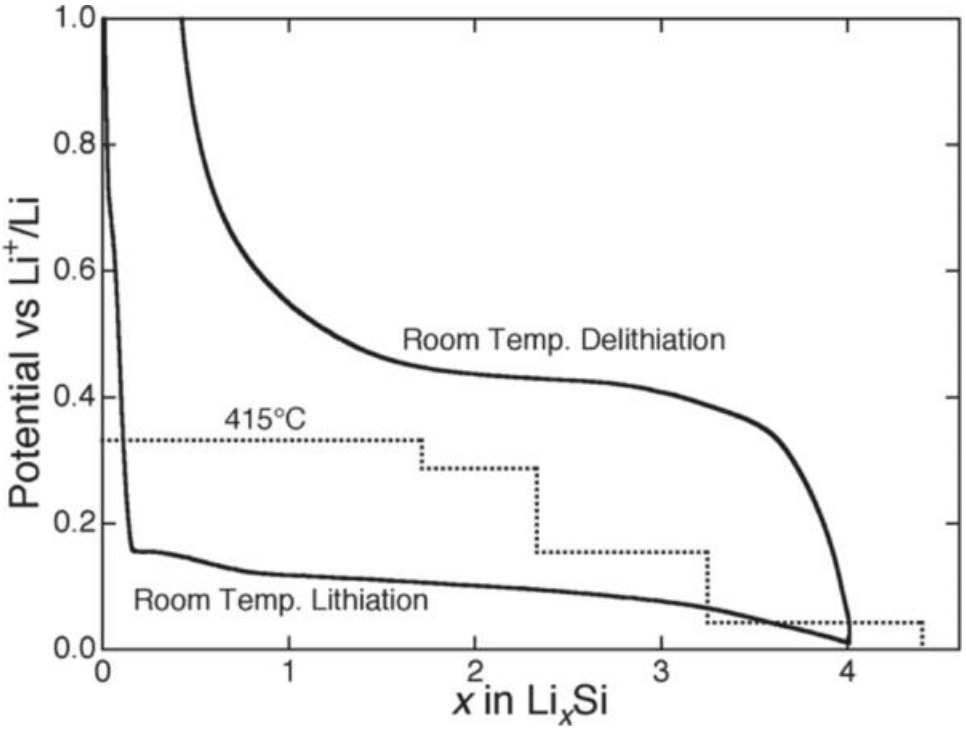

Figure 2.11 Voltage-capacity curves during lithiation of Si at room temperature and high temperature (415 ºC).[49]

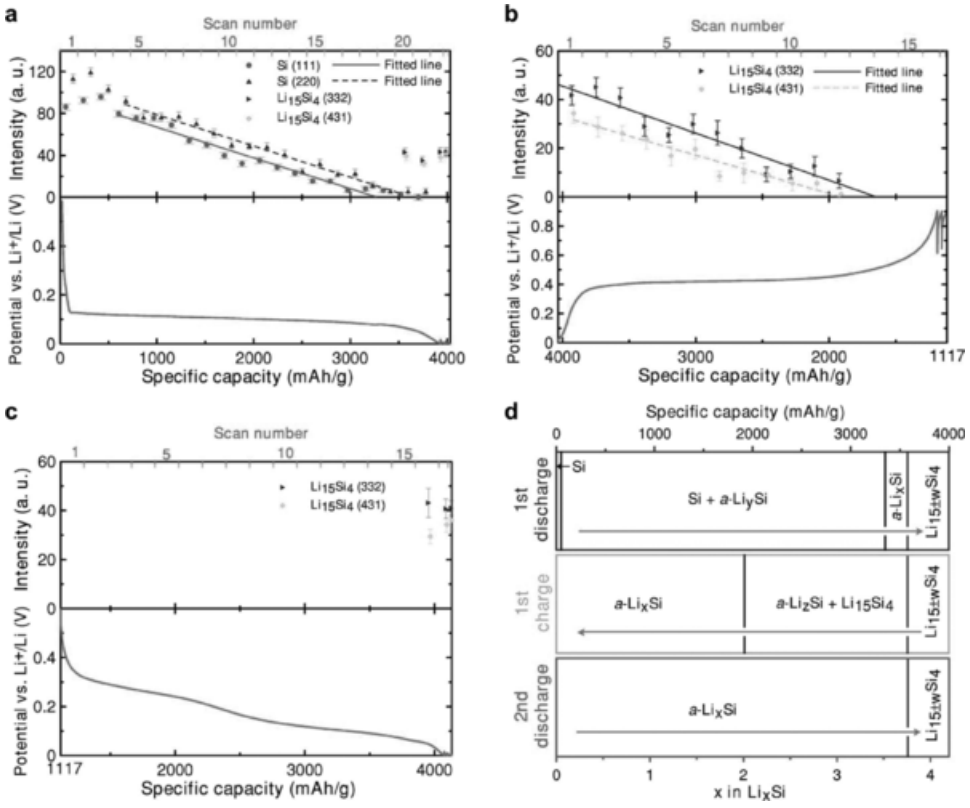

Figure 2.12 In-situ X-ray diffraction during galvanostatic cycling of a crystalline Si electrode in a half cell at room temperature. (a) First lithiation, (b) second lithiation, (c) second lithiation, (d) phase diagram.[44]

2.6 References

1. R. Pvnn, Neutron Scattering a Primer, *Los Alamos Science*, p. 2, Summer 1990.

2. G. E. Bacon, *Neutron Diffraction*, p. 38, Clarendon Press, Oxford, (1975).

3. J. N. Reimers and J. R. Dahn, *J. Electrochem. Soc*., **139**, 2091 (1992)

4. A. Senyshyn, M. J. Muhlbauer, K. Nikolowski, T. Pirling, and H. Ehrenberg, *J. Power Sources*, **203**, 126 (2012).

5. M. A. Rodriguez, D. Ingersoll, S. C. Vogel, and D. J. Williams, *Electrochem. Solid State Lett*., **7**, A8 (2004)

6. M. A. Rodriguez, D. Ingersoll, and D. H. Doughty, *Adv. X-ray Anal*., **45**, 182 (2002).

7. N. Sharma, G. Du, A. J. Studer, Z. Guo, and V. K. Peterson, *Solid State Ionics*, **37,** 199 (2011).

8. W. K. Pang and V. K. Peterson, *J. Appl. Cryst*., **48**, 280 (2015).

9. H. Berg, H. Rundlöv, and J. O. Thomas, *Solid State Ionics*, **144**, 65 (2001).

10. O. Bergstöm, M. Andersson, K. Edström, and T. A. Gustafsson, *J. Appl. Crystallogr*., **31**, 823 (1998).

11. M. Bianchini, J. B. Leriche, J. L. Laborier, L. Gendrin, E. Suard, L. Croguennec, and C. Masquelier, *J. Electrochem. Soc*., **160**, A2176 (2013).

12. M. Roberts, J. J. Biendicho, S. Hull, P. Beran, T. Gustafsson, G. Svensson, and K. Edstrom, *J. Power Sources*, **226**, 249 (2013).

13. N. Sharma, G. Du, A. J. Studer, Z. Guo, and V. K. Peterson, *Solid State Ionics* **199-200**, 37 (2011).

14. N. Sharma, X. Guo, G. Du, Z. Guo, J. Wang, Z. Wang, and V. K. Peterson, *J. Am. Chem. Soc*., **134**, 7867 (2012).

15. B. Vadlamani, K. An, M. Jagannathan, and K. S. R. Chandran, *J. Electrochem. Soc*., **161**, A1731 (2014).

16. M. Potter, H. Fritzsche, D. H. Ryan, and L. M. D. Cranswick, *J. Appl. Crystallogr*., **40**, 489 (2007).

17. S. S. Sidhu, L. Heaton, D. D. Zauberis, and F. P. Campos, *J. Appl. Phys*., **27**, 1040 (1956).

18. O. Bergstom, A. M. Andersson, K. Edstrom, and T. Gustafsson, *J. Appl. Cryst*.,

31, 823 (1998).

19. H. Berg, H. Rundlöv, and J. O. Thomas, *Solid State Ionics*, **144**, 65 (2001).

20. F. Rosciano, M. Holzapfel, W. Scheifele, and P. Novak, *J. Appl. Cryst*., **41**, 690 (2008).

21. J. F. Colin, V. Godbole, and P. Novák, *Electrochem. Commun.*, **12**, 804 (2010).

22. M. Bianchini, J. B. Leriche, J. L. Laborier, L. Gendrin, E. Suard, L. Croguennec, and C. Masquelier, *J. Electrochem. Soc*., **160**, A2176 (2013).

23. T. D. Hatchard and J. R. Dahn, *J. Electrochem. Soc*., **151**, A838 (2004).

24. K. Zhao, W. L. Wang, J. Gregorie, M. Pharr, Z. Suo, J. J. Vlassak, and E. Kaxiras, *Nano Lett*., **11**, 2962 (2011).

25. J. H. Ryu, J. W. Kim, Y. E. Sung, and S. M. Oh, *Electrochem. Solid-State Lett*., **7**, A306 (2004).

26. Y. Oumellal, N. Delpuech, D. Mazouri, N. Dupre, J. Gaubicher, P. Moreau, P. Soudan, B. Lestriez, and D. Guyomard, *J. Mater. Chem*., **21**, 6201 (2011).

27. S. Ohara, J. Suzuki, K. Sekine, and T. Takamura, *J. Power Sources*, **136,** 303 (2004).

28. C. K. Chan, H. Peng, G. Liu, K. Mcilwrath, X. F. Zhang, R. A. Huggins, and Y. Cui, *Nat. Nanotechnol*., **3**, 31 (2008).

29. H. Kim and J. Cho, *Nano Lett*., **8**, 3688 (2008).

30. T. Song, J. Xia, J. Lee, D. H. Lee, M. Kwon, J. Choi, J. Wu, S. K. Doo, H. Chang, W. Park, D. S. Zhang, H. Kim, Y. Huang, K. Hwang, J. A. Rogers, and U. Paik, *Nano Lett.* **10,** 1710 (2010).

31. W. R. Liu, M. H. Yang, H. C. Wu, S. M. Chiao, and N. L. Wu, *Electrochem. Solid-State Lett*., **8,** A100 (2005).

32. S. S. Hwang, C. G. Cho, and H. Kim, *Electrochim. Acta*, **55**, 3236 (2010).

33. R. Deshpande, Y. T. Cheng, and M. W. Verbrugge, *J. Power Sources*, **195**, 5081 (2010).

34. M. Jagannathan, *Ph.D. Dissertation*, University of Utah (2013).

35. E. A. Ponomarev and C. Levy-Clement, *J. Porous Mater*., **7**, 51 (2000).

36. Z. Huang, N. Geyer, P. Werner, J. De Boor, and U. Gösele, *Adv. Mater*., **23**, 285 (2011).

37. A. Janshoff, A. Dancil, K. S. Dancil, C. Steinem, D. P. Greiner, V.S.Y. Lin, C. Gurtner, K. Motesharei, M. J. Sailor, and M. R. Ghadiri, *J. Am. Chem. Soc*., **120**, 12108 (1998).

38. A. Vyatkin, V. Starkov, V. Tzeitlin, H. Presting, J. Konle, and U. Konig, *J. Electrochem. Soc*., **149**, G70 (2002).

39. F. A. Harraz, K. Kamada, K. Kobayashi, T. Sakka, and Y. H. Ogata, *J. Electrochem. Soc*., **152**, C213 (2005).

40. S. Matthias, J. Schilling, K. Nielsch, F. Muller, R. B. Wehrspohn, and U. Gosele, *Adv. Mater*., **14**, 1618 (2002).

41. P. Limthongkul, Y. Jang, N. J. Dudney, and Y. Chiang, *Acta Mater*., **51**, 1103 (2003).

42. M. N. Obrovac and L. Christensen, *Electrochem. Solid-State Lett*., **7**, A93 (2004).

43. M. N. Obrovac and L. J. Krause, *J. Electrochem. Soc*., **154**, A103 (2007).

44. J. Li and J. R. Dahn, *J. Electrochem. Soc*., **154**, A156 (2007).

45. T. D. Hatchard and J. R. Dahn, *J. Electrochem. Soc*., **151**, A838 (2004).

46. C. K. Chan, H. Peng, G. Liu, K. Mcilwrath, X. F. Zhang, R. A. Huggins, and Y. Cui, *Nat. Nanotechnol*., **3**, 31 (2008).

47. K. Kang, H. S. Lee, D. W. Han, G. S. Kim, D. Lee, G. Lee, Y. M. Kang, and M. H. Jo, *Appl. Phys. Lett*., **96**, 053110 (2010).

48. A. G. Morachevskii and A. I. Demidov, *Russ. J. Appl. Chem*., **88**, 547 (2015).

49. C. J. Wen and R. A. Huggins, *J. Solid State Chem*., **37**, 271 (1981).

50. W. J. Weydanz, M. Wohlfahrt-Mehrens, and R. A. Huggins, *J. Power Sources*, **237**, 81 (1999).

51. J. Danet, T. Brousse, K. Rasim, D. Guyomard, and P. Moreau, *Phys. Chem. Chem. Phys*., **12**, 220 (2010).

52. B. Key, R. Bhattacharyya, M. Morcrette, V. Seznec, J. Tarascon, and C. P. Grey, *J. Am. Chem.* Soc., **131**, 9239 (2009).

53. M. Gu, Z. Wang, J. G. Connell, D. E. Perea, L. J. Lauhon, F. Gao, and C. Wang, *ACS Nano*, **7**, 6303 (2013).

CHAPTER 3

AN IN-SITU ELECTROCHEMICAL CELL FOR NEUTRON DIFFRACTION STUDIES OF PHASE TRANSITIONS IN SMALL VOLUME ELECTRODES OF LI-ION BATTERIES

B. Vadlamani, K. An, M. Jagannathan, and K.S. Ravi Chandran.

An In-Situ Electrochemical Cell for Neutron Diffraction studies of Phase Transitions in Small Volume Electrodes of Li-ion Batteries. Reprinted with Permission.

Journal of The Electrochemical Society, 2014, Vol. 161 (10), pp. A1731-A1741

Journal of The Electrochemical Society, **161** (10) A1731-A1741 (2014) A1731
0013-4651/2014/161(10)/A1731/11/$31.00 © The Electrochemical Society

An In-Situ Electrochemical Cell for Neutron Diffraction Studies of Phase Transitions in Small Volume Electrodes of Li-Ion Batteries

B. Vadlamani,[a] K. An,[b] M. Jagannathan,[a] and K. S. Ravi Chandran[a,z]

[a] *Department of Metallurgical Engineering, The University of Utah, Salt Lake City, Utah, USA*
[b] *Chemical and Engineering Materials Division, Spallation Neutron Source, Oak Ridge National Laboratory, Oak Ridge, Tennessee, USA*

The design and performance of a novel in-situ electrochemical cell that greatly facilitates the neutron diffraction study of complex phase transitions in small volume electrodes of Li-ion cells, is presented in this work. Diffraction patterns that are Rietveld-refinable could be obtained simultaneously for all the electrodes, which demonstrates that the cell is best suited to explore electrode phase transitions driven by the lithiation and delithiation processes. This has been facilitated by the use of single crystal (100) Si sheets as casing material and the planar cell configuration, giving improved signal-to-noise ratio relative to other casing materials. The in-situ cell has also been designed for easy assembly and to facilitate rapid experiments. The effectiveness of cell is demonstrated by tracking the neutron diffraction patterns during the charging of graphite/$LiCoO_2$ and graphite/$LiMn_2O_4$ cells. It is shown that good quality neutron diffraction data can be obtained and that most of the finer details of the phase transitions, and the associated changes in crystallographic parameters in these electrodes, can be captured.
 [DOI: 10.1149/2.0951410jes]

Manuscript submitted April 14, 2014; revised manuscript received July 10, 2014. Published July 31, 2014.

Electrodes in Li-ion batteries are subjected to complex phase transitions and structural changes upon repeated lithiation and delithiation.[1,2] The nature and extent of these transitions determine key battery performance metrics such as electrode structural stability, maximum charge capacity, and the degree of capacity fading during cell cycling. In the common graphite anode, lithiation leads to the progressive formation of phases, for example, from solid solution to LiC_{12} and finally to LiC_6, by Li intercalation.[3–5] Any kinetic or Li-diffusion limitation within the electrode or poor electrode conductivity can disrupt these continuous transitions and hence affect the capacity of charge that can be stored. Further, in metallic anodes such as Si, the charge capacity is determined by whether crystallization or amorphization occurs upon lithiation of Si and this appears to be controlled the particle/thin-film characteristics.[6–8] Due to capacity matching, the phase transitions in both electrodes of a cell have to be commensurate with each other–that is, cathode should deliver sufficient flux of Li ions for insertion in anode at the imposed C-rate. Kinetic limitation at one electrode will affect the utilization level of the other electrode and vice-versa. Thus, understanding of equilibrium or nonequilibrium phase transitions at the cell-level, and under the intended operating cell parameters, is a prerequisite to resolve the effects of electrode composition or microstructure or fabrication method on Li-ion battery performance.

Although electrode phase transitions have been studied using in-situ X-Ray diffraction (XRD)[9–11] method, the structural information obtained is limited to a few microns because of the limited depth of penetration. Synchrotron X-ray experiments[12–14] provide an improvement–here the effective depth of penetration is higher–for example, for $LiMn_2O_4$, the depth of penetration[12] is a few hundred microns with 25 keV synchrotron X-Rays. However, the use of XRD for Li intercalating electrodes can be problematic because of the poor X-ray scattering of Li atoms and the associated difficulties with Rietveld refinement of Li-containing phases, especially when these phases are present in small volume fractions.

Neutron diffraction (ND) is well suited for the study of electrode phase transitions in Li-ion cells because (i) the higher depth of penetration[15] of neutrons allows examination of entire electrode volume, (ii) the higher scattering cross-section[16] of electrochemical species like Li or Na allow detection of small amounts of phases and (iii) ND experiments can be conducted non-destructively on commercial batteries.[17–20] There are, however, major difficulties for the laboratory researcher trying to investigate the influence of an electrode composition or fabrication procedure or C-rate effects on electrode phase transitions and crystallography. The principal difficulty is the requirement of large quantities of electrode material powders to make a commercial-size battery and assembling and sealing them hermetically to prevent electrode/electrolyte oxidation during long cell cycles. Many research laboratories are neither equipped for commercial packaging nor such packaging is necessary. Earlier ND studies made use of thicker electrodes[21–23] of the order of few millimeters to obtain neutron diffraction patterns because of lower fluxes at the neutron sources. Electrochemical experiments with thicker electrodes often require higher overpotentials, which can lead to non-equilibrium conditions and/or Li deposition at the electrode surface. This may lead to longer and impractical charging rates, defeating the original purpose. When organic cell components or casing materials with a high degree of structural disorder are present in the diffracting volume, the ND data suffers from large background noise caused by incoherent cross-section from H and $_3Li^7$. This is largely due to the separator, electrolyte and nonactive cell packaging components making it difficult to identify weakly diffracting phases. Obviously, the amounts of separator material and electrolyte have to be kept to minimum levels. This calls for the design of an in-situ electrochemical cell that enables the use of small sample volumes with minimal amount of additional components such that neutron diffraction patterns with better signal-to-noise ratio can be obtained.

In this work, we have designed and constructed a novel electrochemical cell for in-situ ND experiments, which can be used to study the phase transitions in both the electrodes (anode/cathode) simultaneously using minimal electrode volumes. The cell uses (100) oriented single crystal Si sheets eliminating the casing and reducing the background scattering. Single crystal Si has been chosen because it has low incoherent scattering cross-section and produces a significantly lower background compared to V, Ti-Zr null matrix alloy and glass.[24] Roberts et al.[25] have used Al as casing material in their cylindrical in-situ cell and were successful in obtaining a better signal-to-noise ratio. Although Al also has near-zero incoherent neutron cross-section, it gives multiple diffraction peaks that overlap with that from the electrodes. This is avoided here by using (100) Si sheets. Recently, an in-situ cylindrical cell made of the null matrix alloy[26] ($\sim Ti_{2.08}Zr$) was used to study phase transitions in $LiFePO_4$.[27] However, the Ti-Zr alloy, owing to brittleness, is difficult fabricate into sheets for planar cells and is not commonly available. Also, it produces background levels similar to V[24] which may mask weak diffraction peaks.

Using single crystal Si sheets as casing material in our in-situ cell, we show here that good neutron diffraction patterns, indicating clearly the electrode phase transitions, lattice parameter shifts and changes in unit cell volume, can be obtained using ~100 μm thick electrodes. The ND experiments using the in-situ cell were conducted in the VULCAN instrument,[28–30] the time of flight engineering neutron diffractometer at Spallation Neutron Source, Oak Ridge National Laboratory,

[z] E-mail: ravi.chandran@utah.edu

TN, USA. The phase transitions in graphite, $LiCoO_2$ and $LiMn_2O_4$ electrodes during cell-charging to full capacities were tracked and analyzed using Rietveld refinement. We show here that most of the phase transitions and the associated crystallographic information for these electrodes could be captured, using minimum volumes of electrodes.

Experimental

Cell design.— The main objective of this work is to design an in-situ electrochemical cell for neutron diffraction experiments that can use low volume electrodes that can be fabricated in a laboratory. Such a cell should

- Accommodate planar electrode configurations (anode/separator/cathode arrangement) that are commonly made. This would allow rapid experimentation with different electrode compositions, as often as necessary.
- Allow the use of about 100 μm thick battery electrodes in small volumes (with active material area of about 12 mm x 5 mm), making a total cell thickness of about 400 μm. The electrodes are made of powder materials (C, or $LiCoO_2$ or $LiMn_2O_4$ mixed with binder and/or conductive carbon) and are slurry-coated on Cu or Al current collectors and baked to remove the organics. The electrodes are quite fragile.
- Create sufficient diffracted intensities for Rietveld refinement–this means that incoherent scattering from the casing or packaging material should be minimized. For this purpose (100) Si sheets of 500 μm in thickness, are used here as windows. Figure A.1 given in the appendix, is the ND pattern of the (100) Si, which confirms that the background scattering is very low. Additionally, the Bragg peak at 1.35 Å from this material does not overlap with any of that examined in this study.
- Be easy to assemble and seal hermetically to prevent electrolyte oxidation.
- Permit the use of various electrolyte arrangements, that is, either soaked separator or flooded chamber.

The design incorporating all of the above attributes is shown in Figure 1. Basically, the in-situ cell configuration consists of electrodes (1,2) symmetrically arranged with the electrolyte-soaked separator (3) in between them, forming two electrochemical cells. The cell assembly is located in the center of the window that is a cut-out in the Teflon cell frame (4). The electrical contact is made via the copper bolts (5) at the top and through flexible copper wires. To ensure good contact between electrodes and separator, while they are located between the (100) Si sheet windows (6,7), a (100) Si spacer (8) and a precompressed 304 SS spring (9) are installed. The spring is put under slight compression by the Si sheet windows, which are also in compression against the O-rings (10,11). This compression keeps the cell located correctly for diffraction and centered with respect to Si windows. The compression was optimized to achieve full graphite electrode lithiation capacity, by experimenting with springs of different stiffness levels. The O-rings form the seal between the Si windows and the Teflon frame. The nuts and bolts (12,13) are gradually tightened so that uniform pressure is applied on the Si sheet windows by the Teflon outer frames (14,15) without breaking the Si windows. The final step in cell assembly involves tightening the Teflon lid (16) against the Teflon cell frame (4) by uniformly compressing the O-ring (17) so that overall hermetic sealing is ensured. The cell was assembled inside the glove box and was directly placed in the VULCAN diffractometer. Figure 2 is a photograph of the assembled cell.

Neutron diffraction experiments.— For neutron diffraction experiments with the in-situ cell, graphite (99.6% pure, coated on to 9 μm thick Cu current collector) as anode and $LiCoO_2$ (99.9% pure) or $LiMn_2O_4$ (99.5% pure, coated on to both sides of 15 μm thick Al current collector) as cathode were assembled inside the cell. These electrode materials were supplied by MTI Corporation, CA, USA. In each configuration, one centrally-located double-sided cathode and

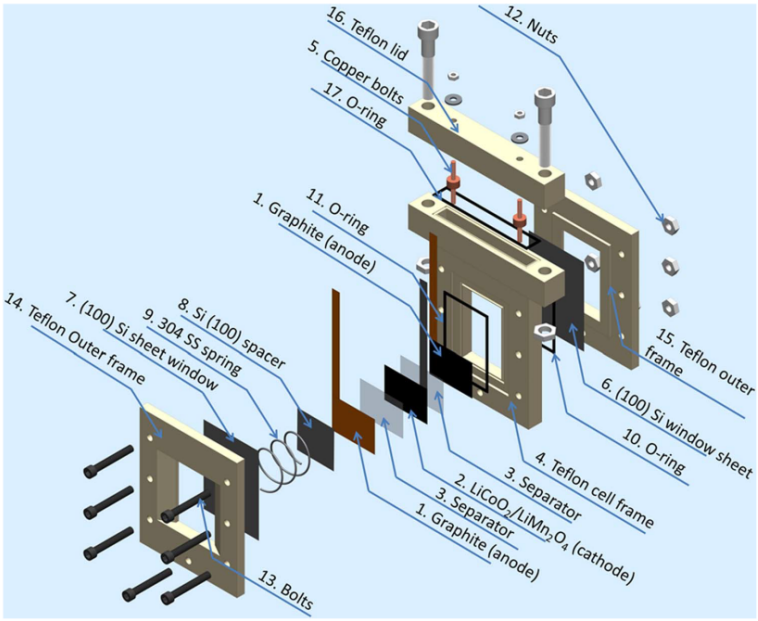

Figure 1. Exploded view of the in-situ electrochemical cell showing various components.

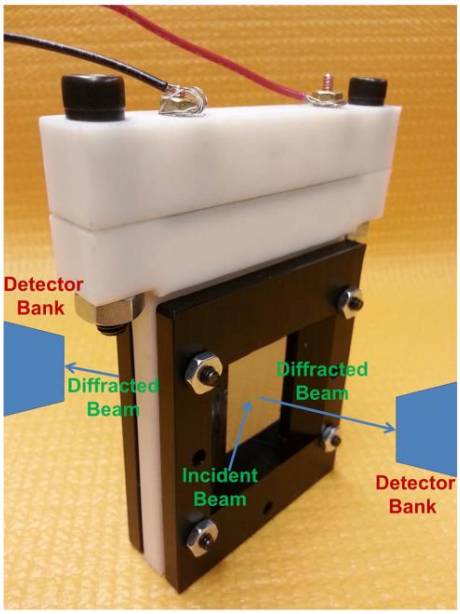

Figure 2. In-situ electrochemical cell in the assembled state.

two single-sided anodes, forming two parallel cells, were used. Electrodes were cut with portions of current collector as contact tabs, extending about 60 mm (Figure 1). The electrical connections between the tabs and Cu contacts at the top of the cell were made by soldering with Cu wires. A 25 μm thick Celgard 3501 separator, soaked in electrolyte (1M $LiPF_6$ in 1:1 ratio of EC:DEC), was placed between each set of electrodes and the cell was fully assembled inside a glove box.

During the ND experiments, the graphite/$LiCoO_2$ cell and the graphite/$LiMn_2O_4$ cell were charged using a Bio-Logic SP-300 potentiostat. The graphite/$LiCoO_2$ cell was charged to 4.2 V at a current of 1.94 mA (C/10 rate) and held at the maximum potential for 1 h. The graphite/ $LiMn_2O_4$ cell was charged to 4.12 V at a current of 2.2 mA (C/9 rate). The charge capacities for the graphite, $LiCoO_2$ and $LiMn_2O_4$ electrodes used here are 14.36 mAh, 10.21 mAh, 9.41 mAh respectively. The capacity-limiting electrodes here, therefore, are $LiCoO_2$ and $LiMn_2O_4$ with theoretical capacities of 140 mAh/g and 105 mAh/g, respectively. The in-situ neutron diffraction data was obtained in the VULCAN diffractometer[28–30] with an incident beam (5 mm × 12 mm) of 0.56–3.44 Å bandwidth allowing the d-space range of 0.4–2.46 Å in the diffracted patterns. The 5-mm collimators were used for the receiving neutrons at the +90° and -90° detectors banks. The cell was oriented at 45 degree from the incident beam (Figure 2), and the effective diffraction volume is about 5 mm × 12 mm × 500 μm. Event-based neutron data was collected continuously as the cell is charged to full capacity. Diffraction patterns were also collected at the fully discharged condition and the fully charged conditions. ND data was binned every 1 h and was reduced using VDRIVE software.[31] The Rietveld refinement, for the study of structural evolution of various phases, was performed using GSAS[32] program with EXPGUI interface.[33]

Results and Discussion

The variation of voltage as a function of Li concentration x in Li_xCoO_2 during cell-charging and the corresponding in-situ neutron diffraction (ND) patterns collected for the graphite/$LiCoO_2$ cell are shown in Figures 3a and 3b. The Li concentration x in Li_xCoO_2 was calculated from the current and the time of charging and the active mass of $LiCoO_2$. As x varies from 1 in fully discharged state of cell to 0.50 in fully charged state (4.2V) of cell, the crystal structure of $LiCoO_2$ evolves from rhombohedral symmetry (R-3m) to monoclinic symmetry (P2/m). The capacity reached after charging the cell for 10 h was 133 mAh/g, which is very close to the theoretical capacity of $LiCoO_2$ (140 mAh/g). Corresponding to this charge, the capacity stored in graphite is 222 mAh/g, which is about 66% of its theoretical capacity (330 mAh/g).

Phase transitions in graphite/$LiCoO_2$ cell.— The phase transitions occurring in the graphite electrode of the graphite/$LiCoO_2$ cell during charging can be seen from the diffraction patters presented in Figures 4a and 4b and 5a and 5b. These figures also include the patterns collected at the fully discharged (x = 1) and charged (x = 0.51) cell conditions. The Bragg reflection at ~1.38 Å could not be indexed based on any of the cell components and remains unchanged upon charging (Figure 5a). Such a Bragg reflection was also observed in work of Wang et al.[17]. At this point we are not clear of the origin of

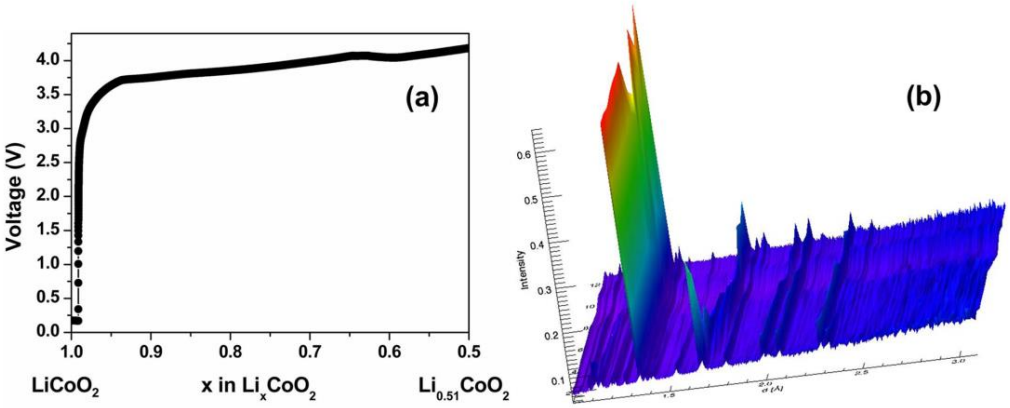

Figure 3. (a) The variation of voltage versus Li concentration x in Li_xCoO_2 as cell is charged to 4.2 V indicating that the $LiCoO_2$ gets transformed to $Li_{0.51}CoO_2$ and (b) the complete neutron diffraction pattern showing the structural changes in graphite, $LiCoO_2$ during charging.

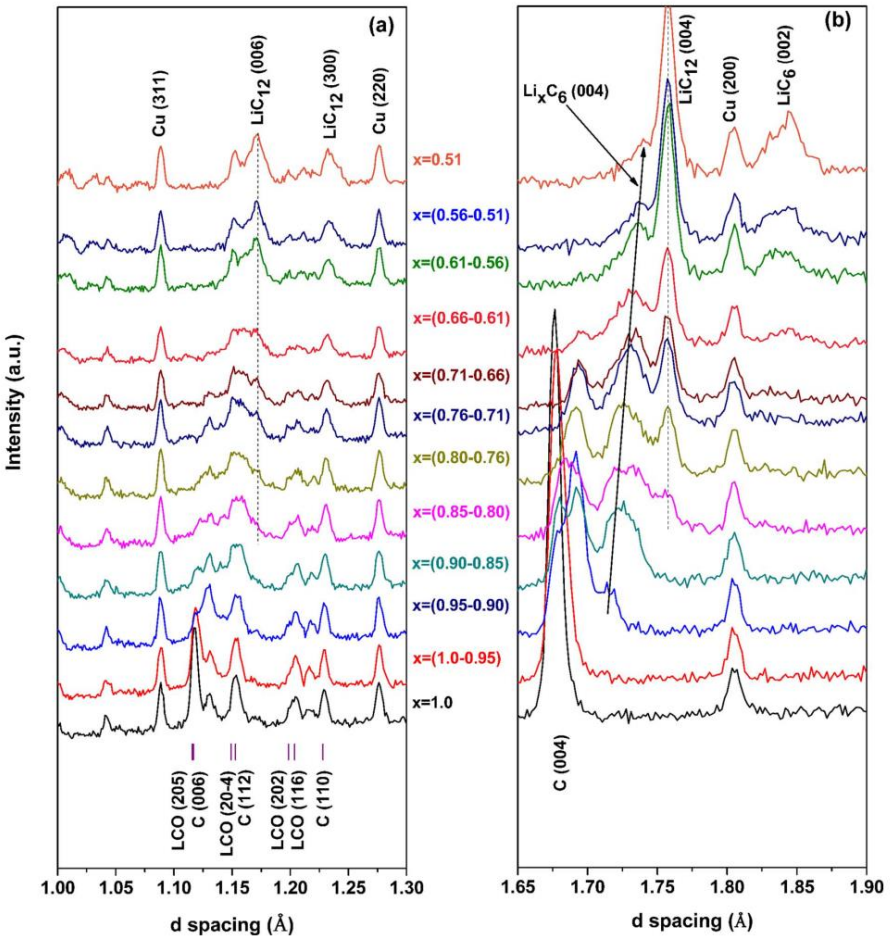

Figure 4. In-situ ND patterns showing the phase transitions in graphite(C) during charging. The formation of various graphite intercalation compounds, Li_xC_6, LiC_{12}, LiC_6 and the changes in their lattice parameters can be seen. (a) for the range:1–1.3 Å and (b) for the range:1.65–1.9 Å. Also the Bragg reflections from $LiCoO_2$ (LCO) are shown.

these reflections. It can be seen that the intercalation of Li in graphite follows various stages. The stages involve the formation of Li_xC_y solid solution, which, with further lithiation, evolves into LiC_{12} and then into LiC_6 compound. Intercalation of Li in the graphite lattice, increases the interplanar spacing between the basal planes. In the present work, this can be seen as the shifting of the (004) peak of graphite (or Li_xC_y solid solution) from 1.675 Å to higher interplanar spacings (Figure 4b). This Bragg reflection vanishes at x = (0.66–0.61) indicating the complete transformation of the solid solution into other compounds, as described below.

A large part of Li storage in graphite is in the form of Li_xC_6 (x = 0.04–0.20) and LiC_{12} and LiC_6 compounds, each overlapping the other during the lithiation process. The compound formation begins with the formation of a new Bragg peak at 1.714 Å (Figure 4b) in diffraction pattern x = (0.95–0.90)–this can be interpreted as the formation of $Li_{0.04}C_6$ during the initial stages of intercalation.[3] As the intercalation proceeds, this peak shifts to the right and finally reaches 1.74 Å in the diffraction pattern x = 0.51 which corresponds to the $Li_{0.20}C_6$ phase.[3] At this stage, a large fraction of the electrode consists of LiC_{12}. The formation of LiC_{12} phase in graphite electrode is principally characterized by the (004) peak which occurs at ~1.757 Å that does not overlap with any of the other phases (Figure 4b). It can be seen that the formation of LiC_{12} phase actually begins after 3 h of charge in the diffraction pattern x = (0.85–0.80) and prevails till the end of charging. This means that Li_xC_6 is gradually consumed by LiC_{12} during the charging period. This is also supported by the formation of LiC_{12}, as evident from its (006) peak at 1.171 Å in the diffraction pattern x = (0.85–0.80) in Figure 4a.

Towards the end of the charging period (last 3 h), LiC_{12} transforms to LiC_6. This is evident in the diffraction pattern x = (0.66–0.61) where the characteristic LiC_6 (002) reflection occurs at 1.84 Å (Figure 4b). The crystal structure of LiC_6 is similar to that of LiC_{12} but for one layer of Li atoms is intercalated in between every two graphene layers.[34] As a result the *c* lattice parameter of LiC_6 is nearly half of that of LiC_{12} (Table I). It is to be noted that LiC_6 is the graphite intercalation compound that accommodates maximum amount of Li. However,

Journal of The Electrochemical Society, **161** (10) A1731-A1741 (2014) A1735

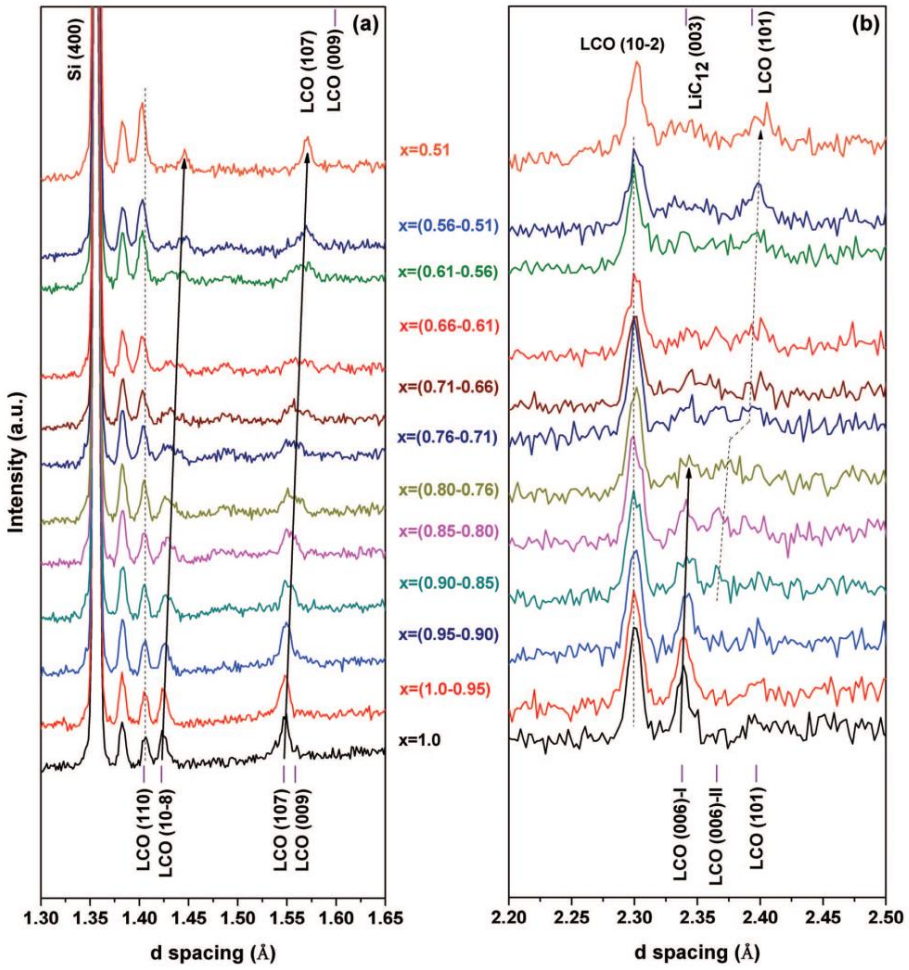

Figure 5. In-situ ND patterns showing the phase transitions in $LiCoO_2$ (LCO) during charging. The shifts in (10–8), (107) and (110) peak positions which indicate the changes in the lattice parameters of $LiCoO_2$ can be observed. (a) for the range: 1.3–1.65 Å and (b) for the range: 2.2–2.5 Å.

at the end of charging, it can be seen from the diffraction pattern x = (0.56–0.51) that not all of the LiC_{12} phase has transformed to LiC_6 phase. This is also reflected in the capacity reaching only 222 mAh/g, while the theoretical being 330 mAh/g for graphite. These observations, made using the present cell, are consistent with the XRD observations of Dahn et al.[3] and the neutron diffraction study of Li-ion commercial battery by Wang et al.[17].

Figures 4 and 5 also reveal the phase transitions in the $LiCoO_2$ electrode, which are consistent with the lithiation of graphite. Based on XRD, Reimers et al.[35] suggested that the delithiation of layered hexagonal Li_xCoO_2 may occur in multiple stages; (i) hexagonal layered structure from $LiCoO_2$ to $Li_{0.93}CoO_2$, termed here as phase I; (ii) a first ordered phase transition from phase I to phases I+II with the composition of phase II lying in between $Li_{0.93}CoO_2$ to $Li_{0.75}CoO_2$; (iii) single phase region in between $Li_{0.75}CoO_2$ to $Li_{0.65}CoO_2$; and finally, (iv) monoclinic phase around $Li_{0.50}CoO_2$.

In the present experiment, the phase transitions occurring in $LiCoO_2$ during the removal of Li ions can be clearly seen from the diffraction patterns presented in Figure 5a and 5b. The interplanar spacing of (110) prismatic planes are decreasing as evident from the slight shifting of the (110) Bragg peak to the left in Figure 5a. This indicates that the *a* lattice parameter decreases as the cell is charged. The shifting of the (10–8), (107) Bragg reflections to the right (Figure 5a), despite the decrease in the *a* lattice parameter, indicates that the *c* lattice parameter must increase. As Li^+ ions are removed from $LiCoO_2$, the repulsion between the negatively charged CoO_2 octahedra aligned along the c-axis would increase and result in the increased interplanar spacing along the c-axis. This is consistent with that observed by others as well.[18,35] The increase in c-axis and the decrease in a-axis indicate that the atomic configurations are rearranged during delithiation. This perhaps is the reason for the absence of any shifting of the main Bragg reflection (10–2) in Figure 5b upon delithiation. This parallels with that observed with respect to $Li(Ni_{1/3}Mn_{1/3}Co_{1/3})O_2$ compound where the d spacing of its (108) peak was found to be constant.[36]

The next prominent (006) reflection of layered phase I of $LiCoO_2$, at ~ 2.338 Å (Figure 5b), can also be used to track changes in the

Table I. Lattice parameters, space groups and atomic positions for various phases in graphite, $LiCoO_2$ and $LiMn_2O_4$ electrodes. Lattice parameters obtained from electrode phases in graphite/$LiCoO_2$, graphite/$LiMn_2O_4$ cells after Rietveld refinement are also given.

Phase	Lattice Parameters (Å) (Literature)	Space group	Atomic positions	Lattice Parameters (Å) (Graphite/$LiCoO_2$ cell, this work)	Lattice Parameters(Å) (Graphite/$LiMn_2O_4$ cell, this work)	Ref.
C	a = 2.464(2) c = 6.711(4)	$P6_3/mmc$	C(0,0,0.25) C(1/3, 2/3,$\frac{1}{4}$)	a = 2.4560(3) c = 6.7002(2)	a = 2.4564(3) c = 6.700(3)	44
LiC_{12}	a = 4.288(2) c = 7.065(20)	P6/mmm	Li(0,0,0) C(1/3, 0,$\frac{1}{4}$)	a = 4.2686(9) c = 7.0229(6)	a = 4.2780(13) c = 7.0231(6)	45
LiC_6	a = 4.305(1) c = 3.706(1)	P6/mmm	Li(0,0,0), C(1/3, 0, 1/2)	a = 4.3008(1) c = 3.687(2)		45
$LiCoO_2$	a = 2.815(1) c = 14.05(1)	R-3m	Li(0,0,0) Co(0,0,0.5) O(0,0,0.23961)	a = 2.8088(4) c = 14.026(4)		46
$Li_{0.51}CoO_2$		R-3m	Li(0,0,0) Co(0,0,0.5) O(0,0,0.23961)	a = 2.8027(6) c = 14.389(6)		
$LiMn_2O_4$	a = 8.2211(4)	Fd-3m	Li(0.125,0.125,0.125) Mn(0.5,0.5,0.5), O(0.263,0.263,0.263)		a = 8.2128(6)	43
λ-MnO_2	a = 8.0639(3)	Fd-3m	Li(0.125,0.125,0.125) Mn(0.5,0.5,0.5) O(0.263,0.263,0.263)		a = 8.060(3)	41

c axis. This Bragg peak shifts to the right with delithiation and its intensity decreases indicating the reduced phase fraction of layered phase I. After 2 h of charging, the development of a weak reflection to the right of the (006) reflection at 2.34 Å (x = 0.90–0.85) can be seen. This seems to correspond to the partial formation of the layered phase II ($Li_{0.9}CoO_2$) in diffraction pattern. This is also supported by the split in the (009) Bragg reflection (Figure 5a) at the same time (x = 0.90–0.85). This phase I→ phase I + phase II transition may be interpreted as first order, because of the continuity of Bragg peaks and the lattice parameters across the two-phase region, as also was shown by Reimers et al.[35]. The (006)-II reflection of phase II shifts to the right with further charging of cell, and, finally reaches 2.4 Å toward end of charging (x = 0.56–51). At the fully charged state (x = 0.51) of cell, it overlaps with the (101) reflection of $LiCoO_2$ (Figure 5b). The present results, based on neutron diffraction, confirm the existence of phase I and phase II during the large part of delithiation of $LiCoO_2$ and the nature of the phase I to I+II transition as the first order. This is in agreement with the in-situ XRD work of Reimer et al.[35] and in-situ neutron diffraction work on commercial Li-ion battery of Sharma et al.[18]. In contrast, such a first order transition was not observed in the ND works of Rodriguez et al.[37] and Senyshyn et al.[19] as well as the XRD work of Rodriguez et al.[38]. The reason for the discrepancy could be due to the way the electrochemical charging was conducted. In the later works, the diffraction data was collected at particular Sate of Charge (SOC) whereas in the former works, the diffraction data was collected continuously as the cell is cycled.

Rietveld Analysis.—To understand the structural transitions of graphite and $LiCoO_2$ in a quantitative manner, Rietveld refinement was performed. The various phases incorporated in refinement during charging process are that of graphite, LiC_{12}, LiC_6, $LiCoO_2$, Cu, Al, Si. The structural information for the electrode compounds is presented in Table I. The isotropic displacement parameters for various atoms were refined using the diffraction pattern obtained in the fully discharged condition. The values thus obtained were used in all other patterns. The background was modeled using a shifted Chebyschev polynomial function with 12 terms. Even though $LiCoO_2$ has shown a first order phase transition during charging with two phases coexisting, during the refinement it was treated as a single phase as the peak splitting was quite small. During Rietveld refinement, exact peak shape was obtained by refining the peak shape parameters gam-1, sig-1, sig-2 in the Profile section of GSAS. The refined ND patterns that were collected for 1 h of counting time at the fully discharged condition and at the fully charged condition (4.2 V) are shown in Figures 6a and 6b for graphite and $LiCoO_2$. The goodness of fit, χ^2, obtained for Rietveld fits in Figures 6a and 6b are 4.1 and 6.2 respectively. In general, the refinement fits with χ^2 in the range of 6 to 11 are considered to be good, for a maximum of 16 independent refinable parameters.[18] For all the reported patterns in the d-spacing range 1 Å to 3.1 Å, the χ^2 values were less than 8.2. This suggests that Rietveld refinement is acceptable.

The structural data including lattice parameters, unit cell volume were extracted from the Rietveld refinement. The lattice parameters of various phases obtained after refinement of the patterns collected at fully discharged state and at fully charged state are shown in Table I. It can be seen that there is good agreement between the lattice parameters determined in this work and that reported in literature. The variation of lattice parameters and the unit cell volume, as obtained from Rietveld refinement, are shown as a function of lithium concentration x (in Li_xCoO_2) in Figures 7a–7d. The lattice parameter *c* of the graphite (Figure 7a) can be seen to be increasing with increased insertion of Li, consistent with the shift of (004) peak of graphite to the right in Figure 4b. Figure 7b shows that the lattice parameters of LiC_{12} and LiC_6 phases do not change significantly which is an indication of attainment of their stoichiometry. The lattice parameter *a* of $LiCoO_2$ can be seen to be decreasing (Figure 7c) due to the decrease in the interplanar spacing of (110) prismatic planes, as was evident from the shifts in (110) reflections of $LiCoO_2$, shown in Figure 5b. Figure 7c also shows continuous increase in the lattice parameter *c* of $LiCoO_2$ which correlates with the continuous shifting of (009) toward right side as in Figure 5a. In this study, a 2.6% increase in the lattice parameter *c* of $LiCoO_2$ was observed which is comparable to that observed by Kim[39] (∼3%) and Sharma[18] (2.9%) when $LiCoO_2$ is fully delithiated. It can also be seen that the unit cell volume of LiC_{12} slightly increases with lithiation (Figure 7d). Interestingly, the unit cell volume of $LiCoO_2$ actually increases upon delithiation–this is due to the repulsion between CoO_2 octahedra after Li is removed.

Phase transitions in $LiMn_2O_4$/graphite cell.— The voltage-versus-lithium concentration x in $Li_xMn_2O_4$ and the corresponding in-situ neutron diffraction (ND) patterns collected during charging to 4.12 V are shown in Figures 8a and 8b. The in-situ ND patterns binned for every 1 h during charging as well as the patterns collected at fully discharged state of cell are shown in Figures 9a and 9b. The phase transitions occurring in graphite and $LiMn_2O_4$ electrodes during charging

Journal of The Electrochemical Society, **161** (10) A1731-A1741 (2014) A1737

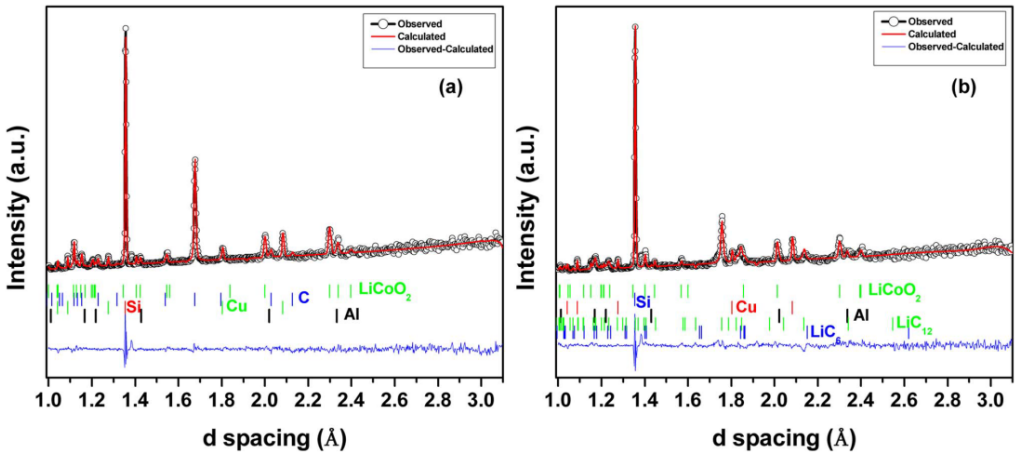

Figure 6. Rietveld refinement plot for graphite and $LiCoO_2$ at (a) fully discharged condition and (b) fully charged condition at 4.2 V. The vertical bars indicate the Bragg peak positions and the blue line indicates the difference between observed and calculated intensities.

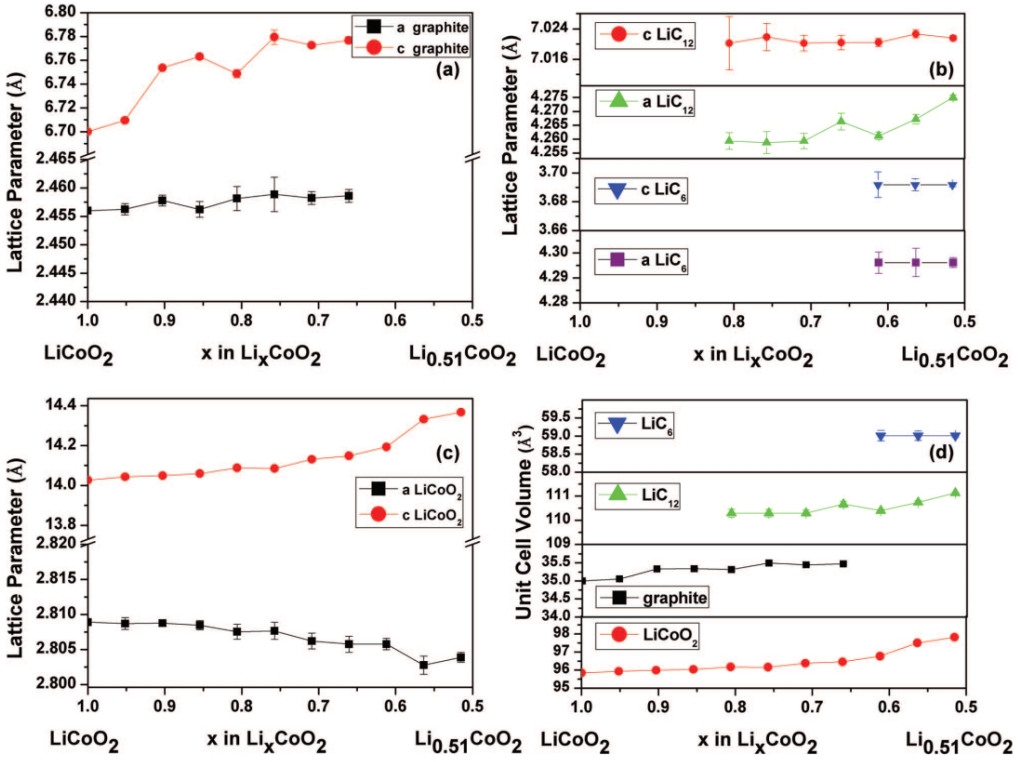

Figure 7. (a-c) The variation of lattice parameters and (d) unit cell volume of various phases as function of lithium concentration x in Li_xCoO_2 in the graphite/$LiCoO_2$ cell. The deviation marks are either equal to or less than the symbol sizes where ever they are not visible.

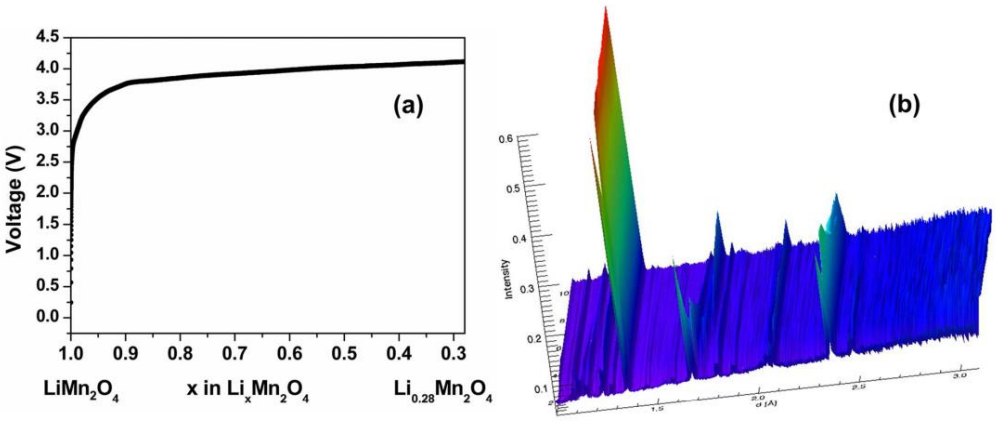

Figure 8. (a)The variation of voltage-versus-lithium concentration x in $Li_xMn_2O_4$ as cell is charged to 4.12 V indicating that, the $LiMn_2O_4$ gets transformed to $Li_{0.28}Mn_2O_4$ and (b) the complete in-situ neutron diffraction patterns during the charging of graphite/$LiMn_2O_4$ cell.

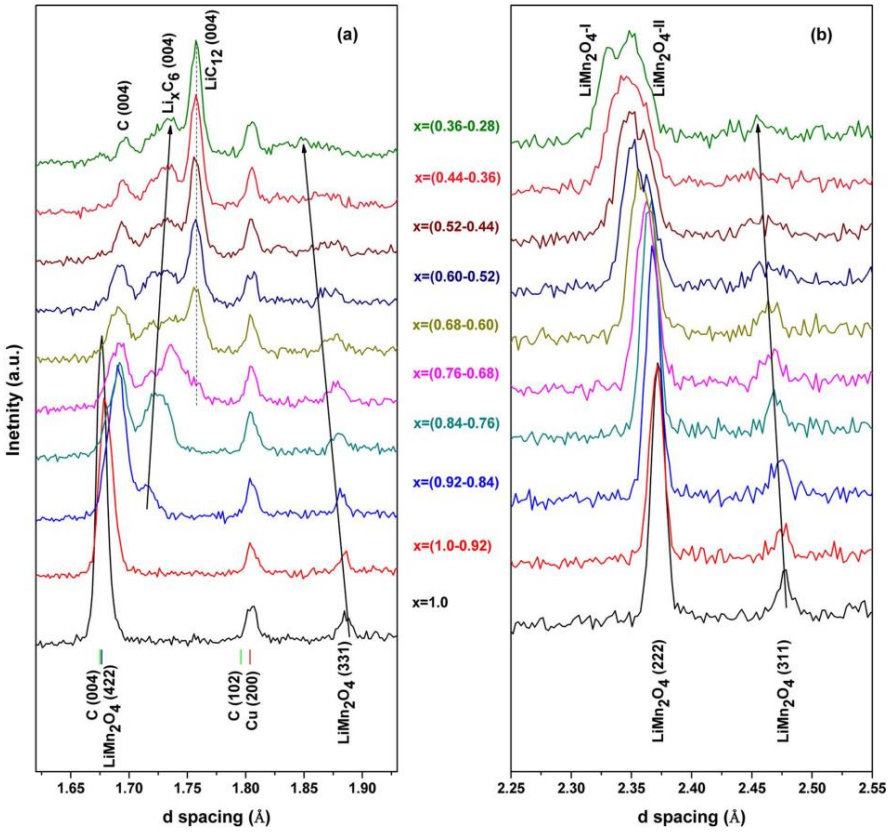

Figure 9. In-situ ND patterns showing the phase transitions in (a) graphite and (b) in $LiMn_2O_4$ during charging.

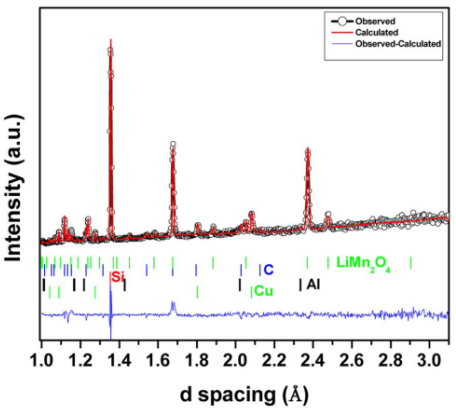

Figure 10. Rietveld refinement plot for graphite and $LiMn_2O_4$ at fully discharged condition. The vertical bars indicate the Bragg peak positions and the blue line indicates the difference between observed and calculated intensities.

are clearly evident from these figures. The Rietveld refined ND pattern that was collected for 1 h of counting time at fully discharged condition is shown in Figure 10. The various phases incorporated in the refinement during charging process are graphite (C), LiC_{12}, $LiMn_2O_4$, Cu, Al, Si. The structural information of the electrode phases is presented in Table I. The variations in the lattice parameters and the unit cell volumes for various phases are shown in Figure 11.

The structural changes occurring in the graphite electrode against the $LiMn_2O_4$ electrode are largely similar to that in graphite/$LiCoO_2$ cell. However, the exception is that, during charging, the highest Li intercalation compound formed in graphite is LiC_{12} but not LiC_6 as was the case for the graphite/$LiCoO_2$ cell. This is due to the lesser Li storage capacity of $LiMn_2O_4$ (105 mAh/g) compared to that in $LiCoO_2$ (140 mAh/g).

The $LiMn_2O_4$ electrode also undergoes phase transition upon delithiation. Ex-situ X-Ray diffraction work of Ohzuku et al.[40] on $Li_xMn_2O_4$ showed that two cubic phases (phase II+phase I) coexist for $0.60>x>0.27$, and a single cubic phase (phase I) exists for $1.0>x>0.6$. Both phase I and phase II exhibit cubic Fd-3m symmetry with different lattice parameters and composition. The present experiments reveal the phase transitions in $LiMn_2O_4$ in detail. As the cell-charging proceeds, the (311) peak of $LiMn_2O_4$ (Figure 9b) can be seen to be shifting to the left indicating decrease in the lattice parameter *a*. The (222) reflection shown in Figure 9b is a strong one and can be seen to be shifting to the left continuously during charging as the Li^+ ion is removed from $LiMn_2O_4$. This indicates the contraction of the unit cell, while still maintaining the integrity of spinel network. Apart from this, it can be seen that the (222) peak broadens and finally gets split into two peaks, which is an indication of formation of two phases during delithiation. The diffraction patterns up to $x = (0.76–0.68)$ could be modeled with single cubic phase I (Fd-3m) in Rietveld refinement. The satisfactory profile fitting for the subsequent diffraction pattern, $x = (0.68–0.60)$, actually needed incorporation of the additional cubic phase II (Fd-3m) in the refinement model. This stage corresponds to the transition from a single cubic phase I to cubic phase I + cubic phase II. With further removal of Li^+ ion, the d-spacing of the two cubic phases can be seen to be decreasing (Figure 9b). Finally, after charging to 4.12 V, the $LiMn_2O_4$ transforms to λ-MnO_2 corresponding to $a = 8.06$ Å.[41] Hence, this work also establishes that $Li_xMn_2O_4$ exhibits (i) single cubic phase structure (I) for $1>x>0.68$ and (ii) two cubic phase structures (I & II) for $0.76>x>0.28$. This is consistent with the work of Ohzuku et al.[40]

The nature of phase transitions in $LiMn_2O_4$ upon delithiation is known to dependent on the material quality. In the study by Mukerjee et al.,[12] delithiation of $Li_xMn_2O_4$ obtained from two different sources was investigated and the diffraction data showed the existence of two cubic phases. However, the XRD data on the electrode obtained from one source, indicated first-order transition with coexistence of two cubic phases clearly whereas XRD data of the electrode from another source indicated no clear evidence of the two-phase coexistence. This is generally in agreement with our work but for the Li composition range for the existence of two-phases. In contrast, the high resolution XRD work of Sun et al.[42] concluded the existence of three cubic phases I, II, III on delithiation of $Li_xMn_2O_4$. In Li-rich electrode, a more continuous change in lattice parameter was seen, whereas in Li-lean electrode jumps in lattice parameters were seen at the point of phase transition. Thus the variation in lattice parameters and the question of coexistence of cubic phases depended on whether $LiMn_2O_4$ phase were Li-rich or Li-lean. This may partially explain the differences seen between these studies. The splitting of (222) peak was not detected in the prior in-situ neutron diffraction works on $LiMn_2O_4$.[21,22,43] This indicates that the present cell, despite the small volumes of electrodes, can indeed detect the finest features with data quality amenable for Rietvield refinement.

Rietveld analysis.—The Rietveld refinement of the ND patterns of the graphite/$LiMn_2O_4$ cell was also done as described for graphite/$LiCoO_2$ cell. The Rietveld refinement in fully discharged state of cell is shown in Figure 10. The goodness of fit, χ^2, obtained is 6.6, indicating a good quality refinement. All the patterns refined had values of $\chi^2<7.7$, inspite of some background scattering, which suggests that the refinement is acceptable. The lattice parameters extracted from the refinement are given in Table I and they agree well with that reported in literature. The (222) reflection, in the patterns $x = (0.68–0.60)$ to $x = (0.36–0.28)$ where the two cubic phases coexisted (Figure 9b), had a complicated shape, mainly because it was overlapping with other phases like LiC_{12} and Al. In the refinement, the shape of this peak was fitted by adjusting the peak shape parameters gam-1, sig-1, sig-2, in the profile section of GSAS.

The variations of lattice parameters and unit cell volumes as the cell is charged, are shown in Figure 11. The lattice parameter *a* of $Li_xMn_2O_4$ can be seen to be decreasing with removal of Li^+ ions (Figure 11a). The average valence of Mn increases from 3.5 to 4, as $LiMn_2O_4$ transforms to λ-MnO_2. As Mn^{+3} has higher ionic radius than Mn^{+4}, the unit cell of $LiMn_2O_4$ must decrease which is consistent with shifting of (311) and (331) peaks to the left. The decrease of lattice parameters of $Li_xMn_2O_4$, continuously across the composition $Li_{0.6}Mn_2O_4$, shows that it is a first order phase transition. As the lattice parameters continuously decreases, so does the unit cell volume, which can be seen from Figure 11c. The increase in lattice parameter *c* as seen in Figure 11b, is consistent with the intercalation of Li atoms in graphite.

In summary, it has been shown in this study that the structural phase transitions that occur in graphite, $LiCoO_2$, $LiMn_2O_4$ electrodes upon lithiation and delithiation could be successfully tracked simultaneously using the in-situ cell designed here. The distinct advantage is that the cell uses only small volume electrodes with thicknesses of about 100 μm. The amount of electrode volume used is greatly less compared to that used in work of Rosciano et al.[23] where $LiNiO_2$ electrode of 5 mm in thickness was used and that of Bergstom et al.[21] where $LiMn_2O_4$ electrode of 6 mm in thickness was used in their respective in-situ cells. This shows that the current in-situ cell is effective in tracking accurately the phase transitions in small volume electrodes.

Further improvements can be easily made to the cell to achieve even better results. The use of Rietveld refinement for precise phase analysis needs data with high signal-to-noise ratio. This can be accomplished by (i) obtaining data with higher intensity from all the phases (ii) minimization of background that masks some of the weakly diffracting phases. The first objective can be accomplished by adding one more layer of anode and cathode. The second objective can be accomplished by the minimization of liquid electrolyte and H-containing cell components. Hydrogen, due to its very high incoherent neutron cross-section, would lead to large background when present in

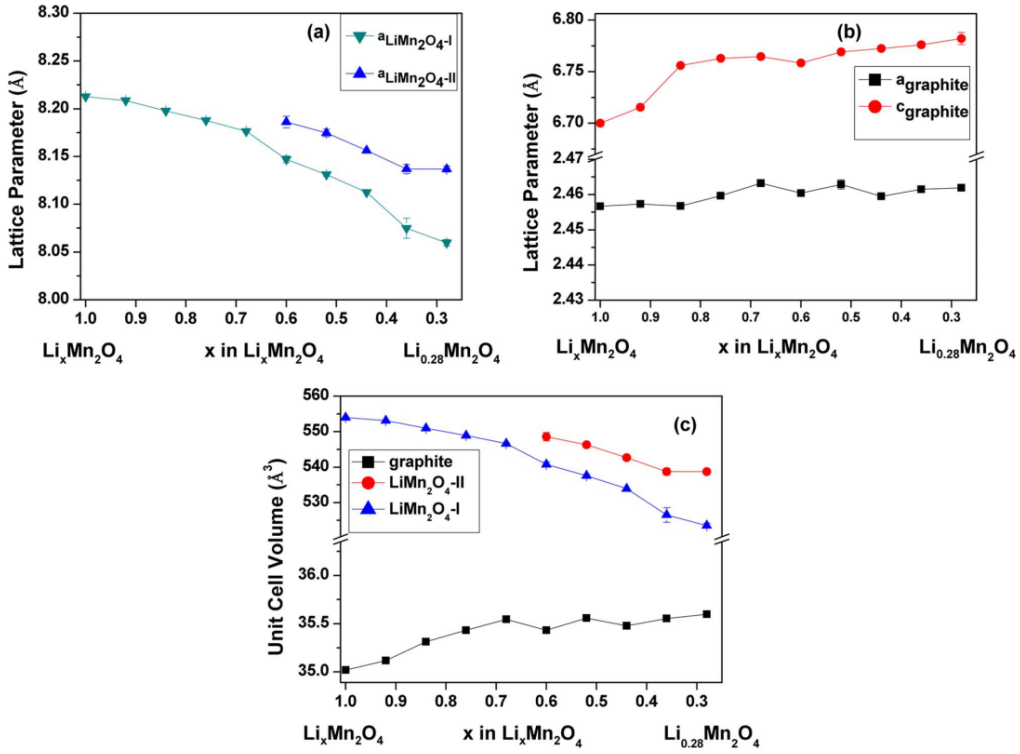

Figure 11. The variation of (a,b) lattice parameters and (c) unit cell volumes of various phases as function of charging time in graphite/$LiMn_2O_4$ cell. Phase I is denoted as $LiMn_2O_4$-I and phase II is denoted as $LiMn_2O_4$-II. The deviation marks are either equal to or less than the symbol sizes where ever they are not visible.

significant quantity. The chief sources of H being liquid electrolyte, casing material and separator. Therefore, the use of deuterated electrolyte in the current cell design could further improve the signal-to-noise ratio.

As for the casing/window, the use of null matrix alloy ($Ti_{68}Zr_{32}$) could completely eliminate the Bragg reflections due to the balancing of the positive coherent scattering length of Ti against the negative coherent scattering length of Zr making the average scattering length of alloy zero.[26] However, the use of null matrix alloy would produce background equivalent to vanadium.[24] The chief requirement of casing material is to produce low background, because halving the background has the same effect as doubling the counting time on signal-to-noise ratio.[26] In this respect, the use of amorphous Si sheet would be ideal as it completely eliminates the Bragg reflections as well as background from the casing material. However, amorphous Si is available at present only as thin films which are not thick or strong enough for application as windows in neutron cells.

Conclusions

1. A novel in-situ cell that provides good quality neutron diffraction data of structural phase transitions in small volume electrode materials of Li-ion batteries was successfully developed. All the structural transitions in graphite, $LiCoO_2$, $LiMn_2O_4$, as reported in literature, could be observed, which validates the cell design.
2. The small volume electrodes provided diffraction data of adequate quality, on which with 1 h binning intervals, Rietveld refinement could be successfully performed and lattice parameters could be extracted. The changes observed in lattice parameters and unit cell volumes are consistent with the structural changes in the electrodes upon lithiation or delithiation.
3. The progression of lithiation in graphite through the solid solution range, Li_xC_6 (x = 0.04–0.20), and the phase transitions to LiC_{12} and LiC_6 are clearly seen in the diffraction patterns.
4. The first order phase transition in $LiCoO_2$, form the layered hexagonal phase I to phase I+II, with the phase II being a delithiated version of phase I, could be clearly identified from the diffraction patterns.
5. The splitting and formation of two phases during the delithiation of $LiMn_2O_4$ could be observed which was not seen in prior ex-situ or in-situ neutron diffraction studies.

Acknowledgments

The research was supported by DoE-BES grant DE-FG02–12ER46891. The authors thank DOE-BES Neutron Scattering program for the support and encouragement. Research conducted at ORNL's Spallation Neutron Source was sponsored by the Scientific User Facilities Division, Office of Basic Energy Sciences, US Department of Energy. Authors thank Dr. S. Rao, formerly at National University of Singapore for his value suggestions. The authors also appreciate the assistance of M. Frost, H. D. Skorpenske and Dr. Y. Chen at SNS during experimentation.

Appendix

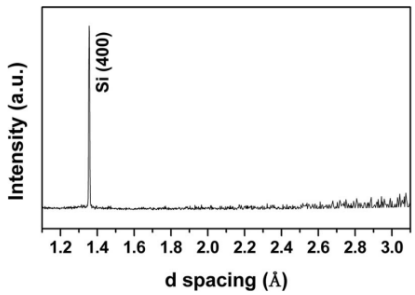

Figure A.1. ND pattern of an empty cell with three 500 μm thick (100)Si sheets as casing showing Bragg reflections with nearly zero background.

References

1. J. B. Goodenough and Y. Kim, *Chem. Mater.*, **22**, 587 (2010).
2. M. Tang, W. C. Carter, and Y.M. Chiang, *Ann. Rev. Mater. Res.*, **40**, 501 (2010).
3. J. R. Dahn, *Phys. Rev. B.*, **44**, 9170 (1991).
4. T. Ohzuku, Y. Iwakoshi, and K. Sawai, *J. Electrochem. Soc.*, **140**, 2490 (1993).
5. M. Inaba, H. Yoshida, Z. Ogumi, T. Abe, Y. Mizutani, and M. Asano, *J. Electrochem. Soc.*, **142**, 20 (1995).
6. P. Limthongkul, Y. Jany, N. J. Dudney, and Y. M. Chiang, *Acta. Mater.*, **51**, 1103 (2003).
7. M. N. Obrovac and L. Christensen, *Electrochem. Solid State Lett.*, **7**, A93 (2004).
8. M. Jagannathan and K. S. Ravi Chandran, *J. Power Sources*, **247**, 667 (2014).
9. D. Mohanty, S. Kalnaus, R. A. Meisner, A. S. Safat, J. Li, E. A. Payzant, K. Rhodes, D. L. Wood III, and C. Daniel, *RSC Adv.*, **3**, 7479 (2013).
10. B. E. Wilson, W. H. Smyrl, and A. Steina, *J. Electrochem. Soc.*, **161**, A700 (2014).
11. K. Rhodes, R. Meisner, Y. Kim, N. Dudney, and C. Daniel, *J. Electrochem. Soc.*, **158**, A890 (2011).
12. S. Mukerjee, T. R. Thurston, N. M. Jisrawi, X. Q. Yang, J. McBreen, M. L. Daroux, and X. K. Xiang, *J. Electrochem. Soc.*, **145**, 466 (1998).
13. H. Yu, H. Kim, Y. Wang, P. He, D. Asakura, Y. Nakamura, and H. Zhou, *Phys. Chem. Chem. Phys.*, **14**, 6584 (2012).
14. J. B. Leriche, S. Hamelet, J. Shu, M. Morcrette, C. Masquelier, G. Ouvrard, M. Zerrouki, P. Soudan, S. Belin, E. Elkaïm, and F. Baudelet, *J. Electrochem. Soc.*, **157**, A606 (2010).
15. R. Pynn, Neutron Scattering a Primer, *Los Alamos Science*, p.2, Summer 1990.
16. G. E. Bacon, *Neutron Diffraction*, p. 38, Clarendon Press, Oxford, (1975).
17. X. Wang, K. An, L. Cai, Z. Feng, S. E. Nagler, C. Daniel, K. J. Rhodes, A. D. Stoica, H. D. Skorpenske, C. Liang, W. Zhang, J. Kim, Y. Qi, and S. J. Harris, *Sci. Reports.*, **2**, 747 (2012).
18. N. Sharma, V. K. Peterson, M. M. Elcombe, M. Avdeev, A. J. Studer, N. Blagojevic, R. Yusoff, and N. Kamarulzaman, *J. Power Sources*, **195**, 8258 (2010).
19. A. Senyshyn, M. J. Muhlbauer, K. Nikolowski, T. Pirling, and H. Ehrenberg, *J. Power Sources*, **203**, 126 (2012).
20. L. Cai, K. An, Z. Feng, C. Liang, and S. J. Harris, *J. Power Sources*, **236**, 163 (2013).
21. O. Bergstom, A. M. Andersson, K. Edstrom, and T. Gustafsson, *J. of Appl. Cryst.*, **31**, 823 (1998).
22. H. Berg, H. Rundlov, and J. O. Thomas, *Solid State Ionics*, **144**, 65 (2001).
23. F. Rosciano, M. Holzapfel, W. Scheifele, and P. Novak, *J. of Appl. Crystallogr.*, **41**, 690 (2008).
24. M. Potter, H. Fritzsche, D. H. Ryan, and L. M. D. Cranswick, *J. of Appl. Crystallogr.*, **40**, 489 (2007).
25. M. Roberts, J. J. Biendicho, S. Hull, P. Beran, T. Gustafsson, G. Svensson, and K. Edström, *J. Power Sources*, **226**, 249 (2013).
26. S. S. Sidhu, L. Heaton, D. D. Zauberis, and F. P. Campos, *J. Appl. Phys.*, **27**, 1040 (1956).
27. M. Bianchini, J. B. Leriche, J. L. Laborier, L. Gendrin, E. Suard, L. Croguennec, and C. Masqueliera, *J. Electrochem. Soc.*, **160**, A2176 (2013).
28. X. L. Wang, *Physica B-Condensed Matter*, **385**, 673 (2006).
29. K. An, H. D. Skorpenske, A. D. Stoica, D. Ma, X. L. Wang, and E. Cakmak, *Metall. Mater. Trans. A.*, **42**, 95 (2011).
30. X. L. Wang, T. M. Holden, A. D. Stoica, K. An, H. D. Skorpenske, A. B. Jones, G. Q. Rennich, and E. B. Iverson, *Mater. Sci. Forum.*, **652**, 105 (2010).
31. K. An, ORNL Report, Oak Ridge National Laboratory (2012) ORNL-TM-2012-621.
32. A. C. Larson and R. B. V. Dreele, *Los Alamos National Laboratory Report (LAUR)*, 86 (2004).
33. B. H. Toby, *J. of Appl. Cryst.*, **34**, 210 (2001).
34. K. R. Kganyago, P. E. Ngoepe, and P. E. Phys. *Rev. B.*, **68**, 205111 (2003).
35. J. N. Reimers and J. R. Dahn, *J. Electrochem. Soc.*, **139**, 2091 (1992).
36. H. Liu, C. R. Fell, K. An, L. Cai, and Y. S. Meng, *J. Power Sources*, **240**, 772 (2013).
37. M. A. Rodriguez, D. Ingersoll, S. C. Vogel, and D. J. Williams, *Electrochem. Solid State Lett.*, **7**, A8 (2004).
38. M.A. Rodriguez, D. Ingersoll, and D. H. Doughty, *Adv. X-ray Anal.*, **45**, 182 (2002).
39. Y. J. Kim, E.-K. Lee, H. Kim, J. Cho, Y. W. Cho, B. Park, S. M. Oh, and J. K. Yoon, *J. Electrochem. Soc.*, **151**, A1063 (2004).
40. T. Ohzuku, M. Kitagawa, and T. Hirai, *J. Electrochem. Soc.*, **137**, 769 (1990).
41. C. Fong, B. J. Kennedy, and M. M. Elcombe, *Z. Kristall.*, **209**, 941 (1994).
42. X. Sun, X. Q. Yang, M. Balasubramanian, J. McBreen, Y. Xia, and T. Sakai, *J. Electrochem. Soc.*, **149**, A842 (2002).
43. H. Berg and J. O. Thomas, *Solid State Ionics*, **126**, 227 (1999).
44. P. Trucano and R. Chen, *Nature*, **258**, 136 (1975).
45. D. Gubrard and A. Herold, *Carbon*, **13**, 337 (1975).
46. H. J. Orman and P. J. Wiseman, *Acta Crystallogr.*, **C40**, 12 (1984).

CHAPTER 4

SILICON WITH COLUMNAR-MICROPOROUS ARCHITECTURE FOR ULTRAHIGH TOTAL ENERGY STORAGE CAPACITY AND WITH HIGHLY REVERSIBLE LITHIATION PERFORMANCE

Submitted for publication as:

B. Vadlamani, M. Jagannathan, and K.S. Ravi Chandran

Silicon with columnar-micro-porous architecture for ultrahigh total energy storage capacity and with highly reversible lithiation performance

Nature Scientific Reports, 2017

4.1 Abstract

The success of miniature microelectronic devices, such as labs-on-chips, depends critically on the energy storage capacities of on-chip Li-ion batteries. The search for positive electrodes for such batteries inevitably leads to Si because of its very high *specific capacity* (~3580 mAh/g for $Li_{15}Si_4$). Although thin films and nanowires can provide very high specific capacities, their *total storage capacities* are, however, very limited. We report here a new Si electrode architecture, having *columnar micropores*, which provides a highly reversible specific Li-storage capacity (~1250 mAh/g), and the highest total Li-storage capacity (~1.25 mAh/cm^2) relative to other Si electrodes. It is shown that this Si architecture can store a greater amount of charge (~250%) than solid-Si, due to the increased surface area of columnar pores. Further, the most exciting finding of this study is that the pore walls of the columnar microporous architecture do not crumble even after a large number of cell cycles, mitigating the Si cracking issues. Electron microscopy revealed that the superior performance is due to the accommodation of volume changes within the pores. The present findings reveal a new pathway for architecturing Si electrodes for much larger and highly reversible total charge-storage capacities for on-chip Li-ion cells.

4.2 Introduction

There have been rapid and impressive advances in the technologies of microelectronic devices in recent years, including the development of high-density CMOS memories,[1] microscale actuators or sensors,[2] drug delivery systems,[3] implantable heart defibrillators,[4] and other such devices.[5] The functional requirements of these

devices strictly isolate them in their application environments. Any external supply of power to these devices is not only challenging but could severely limit their functionality.[6] Therefore, the concept of "the-chip-that-powers-itself" is quite appealing because of the tangible gains in efficiencies of power storage and the decentralized power distribution, without limiting the functionality. For example, the power requirement of a RFID tag, which is implanted in consumer products or in animal pets for tracking, is about 10 μW.[7] This device would consume about 300 J of energy in a year. To power such a device for a year, using a single layer of Si thin film Li-ion cell electrode (for example, using a 150 nm thick Si electrode providing a total capacity of ~80 μAh/cm^2), a chip area of 28000 mm^2 will be needed. This size requirement is unrealistic, as this is much larger than the size of a typical semiconductor chip. Evidently, there are constraints on the areal foot print, and hence the *total capacity* (which depends on the thickness dimension) of the electrode becomes more important than the *mass-specific capacity*. Additionally, the integration of on-chip-Li-ion-cell is feasible only if the electrode fabrication process is compatible with electronic microfabrication processes. Si is thus attractive from two important considerations: (i) highest theoretical capacity and (ii) compatibility with chip fabrication.

Si thin films, although they may appear to be very desirable from the point of view of microfabrication compatibility and impressive specific capacities, in reality possess a relatively low *total energy storage capacity*. What is meant by total capacity is the total amount of charge that is stored in the volume the electrode, but delivered over an area on demand, and represented here as mAh/cm^2. The total capacities of Si thin film electrodes are in the range of 0.04 to 0.11 mAh/cm^2.[8] For example, an amorphous Si thin film (~50

nm thickness) electrode provided a total capacity ~ 0.04 mAh/cm^2 (specific capacity ~3500 mAh/g) for 200 cycles[9] at ~1C rate. However, with a 150 nm thick amorphous Si film, the total and specific capacities reduced to ~ 0.08 mAh/cm^2 and ~2200 mAh/g, respectively, after ~200 cycles.[9] A further increase in film thickness degraded the capacity and cyclability even more—the total and the specific capacities of 300 nm thick Si film were ~ 0.11 mAh/cm^2 and ~1700 mAh/g, respectively, after 200 cycles.[10] The power requirement of the RFID tag is ~10 μW,[7] which requires a total energy of ~300 J per year to operate. The total capacity of 300 nm thick Si thin film, assuming a delivery area of 30 mm^2, is ~0.5 J. This is evidently far lower than that required for the RFID tag mentioned above. More importantly, the mass-specific-capacity of Si thin film is a misleading measure of energy storage capacity because the effective total capacity (~0.11 mAh/cm^2) achievable without cracking is quite low. It is also far less than that required to match the total capacity of 50 μm thick $LiCoO_2$ electrode (1.75 mAh/cm^2). Meaningful increases in the total capacities of Si thin films, while requiring high reversibility of lithiation, are not possible for two reasons. First is the diffusion limitation (the Li diffusion coefficient, D_{Li}, in amorphous Si film is ~10^{-11} to 10^{-13} cm^2/s [11]) leading to limits on the thickness of Si that can be lithiated fully. At 1C rate, this thickness is about 190 nm. Another reason is the rapid capacity fading with cycles due to cracking of the film (~300% volume change for $Li_{4.4}Si$ or ~180% for amorphous $Li_{2.7}Si$ during lithiation[12]), the delamination from the substrate, and the consequent loss of electrical contact.[13] The total capacity cannot be improved without solving the diffusion limitation problem and the cracking problem.

Recognizing these limitations of Si thin films, recent research attempted to improve

the performance by making Si electrodes with nanoparticles,[14,15,16] nanowires (NWs),[17,18,19] or nanotubes.[20] For example, nanowires (dia. ~ 141 nm, length ~ 10 μm), grown by the vapor-phase method, exhibited a very high capacity, about ~3500 mAh/g, although this lasted for only 20 cycles at the C/5 rate.[17] This result can be deceiving—the total capacity is only 0.7 mAh/cm^2 and this is due to the rather low Si mass density (0.2 mg/cm^2) in this nanowire electrode. The total capacity, however, can be increased either by increasing the NW diameter or the density of nanowires, both of which would increase the Si mass density. The mass loading density for NWs of 100 nm diameter is about 0.4 mg/cm^2 and it could be increased to 1.52 mg/cm^2 for nanowires of 500 nm in diameter.[21] However, NWs with diameters exceeding 300 nm do not cycle well due to premature fracture during lithiation.[22] It is quite important to note that the total capacity of 300 nm diameter NW, which could be taken as an upper limit of a practical nanowire electrode, is only 0.3 mAh/cm^2. This is, in fact, far lower than that of a graphite electrode[23] with ~50 μm thickness (~4 mAh/cm^2) that is used in commercial Li-ion cells. Further, the NWs, after some cycling, lost electrical continuity with substrate leading to capacity fading—the roots of NWs do not seem to withstand the stresses created by the volume-changing strains. Thus the NWs, although impressive when assessed in terms of specific capacities, actually show a much lower total capacity and are prone to early fracture during lithiation and delithiation cycling.[23] Moreover, the NW synthesis processes are not compatible with conventional semiconductor processing, making the practical implementation in on-chip fabrication more challenging.

We demonstrate here that *microporous Si (μp-Si) architecture*, fabricated on single crystal Si wafer by an inexpensive electrochemical etching route, can lead to a high

specific energy capacity and the highest-to-date total capacity in Si over 200 cycles. The physical limitations of Si thin films and nanowires, as discussed above, suggest that new strategies must be developed to increase the total capacity of Si electrodes to the level required for on-chip application. When the footprint area is the principal geometric constraint, the only way to increase energy storage is to go for a three dimensionally (3D) architectured electrode.[24,25] The 3D electrodes, owing to a larger surface area for lithiation or delithiation, can lead to higher Li storage capability and could perform well at high cycling rates. One way to create the 3D architecture is to use microfabrication methods (photolithographic patterning and reactive-ion etching) to create 3D columnar structures on Si. However, Si columns with the required small enough sizes (< 1 μm) are not only too difficult to create by photolithography, the process is also expensive. Additionally, the typical lithographic columns (1x1 μm^2 columns spaced apart by ~1μm, giving 25% area density) are too far apart leading to a relatively low effective mass of Si available for lithiation. Hence this approach will not lead to high total capacities. The objective of the present work, however, is to show that the architecturing of single crystal Si with columnar micropores, made possible by the anisotropic etching characteristics of Si,[26,27] can produce an electrode with impressive cyclic performance and total energy storage capacity. It is also shown that the columnar pores, with a specific architecture, can synergistically accommodate a significant part of the volume increase due to lithiation, and reduce the cracking tendency greatly.

4.3 Results and Discussion

The SEM micrographs showing the top and side views of the microporous architecture of the Si (µp-Si) electrode, made by electrochemical etching (see Methods section), are shown in Figure 4.1a and 4.1b respectively. The electrode is made of uniformly distributed columnar pores of 1.1 µm in average diameter and 8 µm in average depth, with a continuous Si wall structure (mass loading density ~0.9 mg/cm^2) throughout the electrode. The effective surface area of the columnar micropores, available for lithiation, was calculated to be ~14 times higher than that of solid-Si.

The potential of µp-Si architecture to store a relatively higher amount of Li is first explored through cyclic voltammetric (CV) experiments. The CV data for solid-Si and µp-Si are shown in Figure 4.2a-c and 4.2d-f respectively. The most striking result is that the total capacities, as revealed in the lithiation and delithiation currents of µp-Si (Figure 4.2d), are several times higher than that for solid-Si (Figure 4.2a). The variations in the total capacities during each cycle, obtained by integrating the CV curve, are shown in Figure 4.2g. For both Si electrodes, the total capacities increase at first and subsequently reach a plateau. The steady-state total lithiation capacity of µp-Si is ~375 µAh/cm^2, which is 250% of that of solid-Si (150 µAh/cm^2). This increase in total charge storage capacity can be solely attributed to increased surface area in the columnar pore architecture.

The specific electrode surface reactions, upon lithiation, were also analyzed by evaluating the peak positions. For both solid-Si (Figure 4.2b) and µp-Si (Figure 4.2e), all the lithiation curves exhibit a strong peak at ~0 V (labeled A) and this corresponds to the formation of $Li_{22}Si_5$.[28] An additional lithiation peak (labeled B) starts to evolve at 155

mV in cycle 2 and progressively shifts toward a lower voltage with further cycling, eventually overlapping with the peak A after 15 cycles. The formation of peak B and its gradual shift to peak-A-position is likely to correspond to the formation of a-Li_xSi in cycle 2, and its enrichment with Li in subsequent cycles. This enrichment of a-Li_xSi surface layer with lithiation cycles will naturally make its composition reach $Li_{4.4}Si$ (or $Li_{22}Si_5$) at ~0 V eventually. This is also evident from the increased peak currents of Li_xSi and $Li_{4.4}Si$ with cycling.

The nature of delithiation in µp-Si (and in solid-Si for reference) can be understood by tracking the two peaks labeled C and D, shown in Figure 4.2c and 4.2f. The peak C originates at 362 mV in the first cycle and shifts to a higher voltage (430 mV) in subsequent cycles. This can be explained as the formation of $Li_{13}Si_4$ (or $Li_{3.25}Si$) phase because the final peak is close to 428 mV, which corresponds to the equilibrium potential of $Li_{13}Si_4$ phase.[29] Similarly, the peak D occurs at 536 mV in the first cycle and progressively shifts to 620 mV in fifteen cycles. This can be attributed to $Li_{12}Si_7$ (or $Li_{1.71}Si$) formation because this peak is close to 582 mV, which is the equilibrium potential of $Li_{12}Si_7$ phase.[29] Since the peaks in the CV data occur at similar potentials for both solid-Si and µp-Si, it is evident that the columnar micropores did not fundamentally alter the mechanism of phase transitions in Si upon lithiation or delithiation. The trends in the CV data for Si and µp-Si are also in agreement with that observed for Si nanowires,[30] pillar arrays on Si substrate,[31] or other microcolumnar Si[32] morphologies.

The galvanostatic cycling performance of µp-Si electrode and the corresponding variation in specific capacity with cycles are shown in Figure 4.3a and 4.3b, respectively. The performance of solid-Si, tested at same current density as the µp-Si electrode, is

presented in Figure 4.3c and 4.3d. The µp-Si morphology was lithiated to a capacity of 3580 mAh/g during the first cycle. The subsequent delithiation, however, occurred only to a capacity of ~3300 mAh/g. These capacities diminished with further cycling. Nevertheless, it can be seen that µp-Si exhibits an excellent cycling behavior with the specific capacity stabilizing at ~1250 mAh/g after ~220 cycles (test 1). In a duplicate experiment (test 2), µp-Si attained capacity of ~1500 mAh/g after 100 cycles (Figure 4.3b), which confirms the excellent repeatability of the galvanostatic result. Clearly, this performance is much better than that of solid-Si (Figure 4.3d) where the specific capacity drops to a low value of ~500 mAh/g in about 33 cycles, after which the cell is an open circuit. The total capacity of the columnar microporous Si electrode is ~1.25 mAh/cm^2, which compares favorably with that (1.75 mAh/cm^2) of the 100 µm thick $LiCoO_2$ counter electrode in commercial Li-ion cells. Hence, capacity matching of µp-Si with $LiCoO_2$ is quite favorable.

To explain the relatively large cyclable total capacity, the structural changes in the microporous electrode were investigated by SEM. The structure of µp-Si electrode after 220 lithiation/delithiation cycles is illustrated in Figure 4.4(a-f). A regular and stable cracking pattern, resembling tessellated islands of contiguous pore walls (~ 70 x70 µm^2; Figure 4.4a and 4.4e), is observed in the µp-Si electrode (Figure 4.4a). The cracks are nearly perpendicular to each other and are perpendicular to electrode edges, which are parallel to (110) planes. This suggests that the cracks are parallel to <110> directions. Such a cracking pattern was also observed by He[33] et al. in lithiation/delithiation cycling of 500 nm Si thin film. The fact that the (110) plane has a relatively lower fracture toughness[34] may explain the observed cracking pattern in µp-Si. Clearly, the formation of

the tessellated islands by crystallographically oriented cracks seems to have helped in relieving the stresses created during lithiation and delithiation cycles. The enlarged SEM micrographs of a representative island are shown in Figure 4.4b and 4.4c. Within the island, the residual porosity after 220 cycles is ~11% (Figure 4.4c) whereas the electrode was ~50% porous prior to lithiation (Figure 4.1a). This clearly demonstrates that a part of the pore volume (~39%) is filled up by the lithiated phase.

The most remarkable finding of this work is the evidence that (Figure 4.4e and 4.4f) almost all of the tessellated islands in the µp-Si are fully intact with substrate, maintaining electrical contact, even after 220 cycles. The detachment of some of the islands (Figure 4.4f) is due to the cleaning step involved in the preparation of the electrode for SEM. In contrast, the solid-Si is found to crack severely in 33 cycles (Figure 4.4g and 4.4h). The extensive delamination and curling of the lithiated layer, followed by the loss of electrical contact with substrate, is clearly the reason for its poor cycling behavior. On the other hand, the cracking pattern itself cannot sufficiently explain the accommodation of volume change in µp-Si upon lithiation. It is very likely that the volume expansion is accommodated principally by the porous structure of µp-Si, largely due to growth of the lithiated phase into the pores. Thus, the exceptionally good cycling performance of the µp-Si electrode can be attributed to the unique microporous architecture, and this arises from: (i) the increased Si surface area for lithiation, (ii) effective accommodation of volume change within the pore walls, (iii) the preservation of electrical contact at the base of the cracked islands (Figure 4.4e and 4.4f), and (iv) the preservation of the columnar structure even after a large number of cycles.

To understand the lithiation processes within the pore walls, the structure of lithiated

µp-Si was investigated by transmission electron microscopy (Figure 4.5). The FIB-cut thin slice for TEM imaging is shown in Figure 4.5a-4.5c. The lithiation in µp-Si occurred to a depth of about 380 nm from the wall surface, which can be seen as the dark annular region around each pore (indicated by white arrow in Figure 4.5c). The lattice image (Figure 4.5e) obtained in a region next to the pore surface (Figure 4.5d) confirms the formation of amorphous structure (a-Li_xSi) during lithiation. This is also confirmed by the absence of spots in the corresponding FFT image (Figure 4.5f) and kikuchi lines in the CBED pattern (Figure 4.5g). Moving further into the lithiated region, the amorphous structure transitions to amorphous + crystalline structure (Figure 4.5h), where the amorphous matrix is found to contain crystalline islands of Si ~6 nm^2 in size, embedded in a-Li_xSi (Figure 4.5i). This is similar to the formation of amorphous + crystalline structure in NWs [17] upon lithiation. Figures 4.5j through 4.5k illustrate the NBD patterns confirming the progressive transition of the structure of the lithiated region from amorphous to crystalline Si. The two-phase structure, in the middle of the lithiated region, is characterized by spot and diffuse rings present in the NBD patterns (Figure 4.5j and 4.5k). The HRTEM image obtained outside of the annular region shows a fully crystalline Si structure, which is additionally confirmed by FFT (inset) with spots (Figure 4.5m).

The energy storage capacity of an electrode is truly reflected in terms of its total capacity, as opposed to the conventionally used measure, which is the mass-specific-capacity. This is illustrated by comparing the variation of specific capacities and total capacities with cycle number, in Figure 4.6a and 4.6b respectively, for various forms of Si. The data for µp-Si is from the present work, and the data for Si thin film, nanowire

and particle morphologies, taken from literature, are all included. In terms of specific capacity, the thin film (50 nm thick) morphology shows the highest reversible capacity due to a relatively shorter Li diffusion length (thickness). However, when the data are plotted in terms of total capacity (mAh/cm^2), the performance of Si thin film is quite poor and this is due to the limited thickness for charge storage. The µp-Si exhibits the highest total capacity (mAh/cm^2) amongst all the morphologies considered—this is principally due to a much higher surface area afforded by the columnar microporous architecture, which provides for efficient and reversible storage of a relatively higher amount of Li. The µp-Si electrode morphology therefore has the potential to succeed in technological applications such as on-chip batteries.

The present work has demonstrated that µp-Si electrodes can be architectured to produce a high degree of energy storage and with good cell cyclability. In particular, the present work helps to dislodge some negative impressions about the potential of µp-Si that arise from the examination of results in previous works.[35,36,37,38] For instance, Thakur et al. [39] reported that their µp-Si provided a specific capacity of only about 500 mAh/g in the first cycle, which decreased to 76 mAh/g in the tenth cycle. With a gold coating over the µp-Si, the specific capacity, although increased in the initial cycles, came down to ~1400 mAh/g after 163 cycles. The reason for this performance only with a gold coating, was not explained. Perhaps due to these factors, the previous works did not generate sufficient enthusiasm about the potential of µp-Si as an electrode for Li-ion battery till date. The present results, on the other hand, convincingly demonstrate the great promise of µp-Si for practical high capacity energy storage electrodes.

4.4 Conclusions

In summary, it has been demonstrated that µp-Si, with a columnar architecture, can perform as an electrode material with superior mass-specific capacity as well as total capacity for energy storage in Li-ion cells. An exceptionally high, record total capacity of ~1.25 mAh/cm^2 (1250 mAh/g) over 220 cycles, for µp-Si, during galvanostatic cycling has been observed. This is comparable to the total storage capacity of $LiCoO_2$ negative electrodes (mAh/cm^2) in Li-ion cells. The superior performance of µp-Si is attributed to (i) the increased Si surface area for lithiation, (ii) effective accommodation of volume change within the pore walls, (iii) the preservation of electrical contact at the base of tessellated islands, and, more importantly, (iv) the preservation of the columnar structure of the pores even after a large number of cycles.

4.5 Methods

4.5.1 Electrode Preparation

The µp-Si used in this work was fabricated from (100) oriented and p-doped single crystal wafers (obtained from University Wafers, MA, USA) of about 150 mm in diameter. The surface of the wafer was first cleaned with 48% HF to remove any native oxide layer. Electrochemical etching to create a porous structure was carried out using a home-made etching cell, constructed out of Teflon. A platinum counter electrode and an electrolyte of composition (HF:DMF = 1:10) were used for etching. The etching was carried out at a current density of 3 mA/cm^2 using KEITHLEY, 2601B Source-meter. The µp-Si electrode produced by the etching was thoroughly rinsed with methanol and dried in flowing nitrogen.

4.5.2 Electrochemical Measurements

The electrochemical experiments were performed by assembling the µp-Si electrode and the counter electrode in Swagelock cells made out of Teflon. A lithium foil (750 µm thick) was used as the counter electrode. The electrolyte used was of the composition: 1M $LiPF_6$ in EC:DEC = 1:1 (Novolyte Technologies, BASF). The cyclic voltammetric (scan rate of 0.5 mV/sec) and galvanostatic measurements (C/10 rate) were made using the Gamry Potentiostat (Reference 3000). A current density of 3.29 $\mu A/cm^2$ was used for the galvanostatic studies of both µp-Si and solid-Si. The electrode assembly and the electrochemical and cycling experiments were performed inside an Ar-filled glove box where the levels of H_2O and O_2 were maintained below 0.1 ppm.

4.5.3 Microscopy Analysis

The µp-Si electrodes after cycling were thoroughly cleaned, to remove the electrolyte residue, by shaking the electrodes in DMC for 20 min inside the glove box. The structure of the µp-Si electrode and the pores were examined using SEM (FEI Quanta 600 FEG). The sample for TEM analysis was prepared using the FIB technique using Ga^+ ion. High resolution transmission electron microscopy (HRTEM) imaging and nano beam diffraction (NBD) were conducted using JEOL JEM 2800. The NBD patterns were obtained from an area of 320x320 nm^2 in the [0 0 1] zone axis. The CBED patterns were obtained from an area of 46x46 nm^2 near the pore surface.

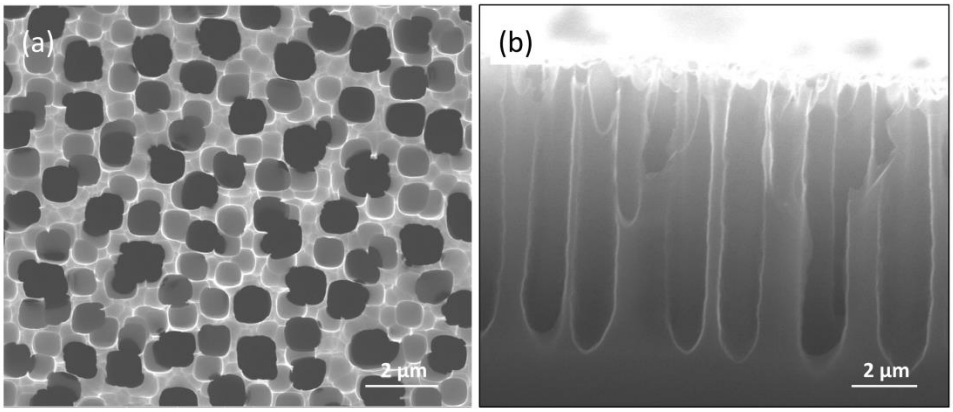

Figure 4.1. The morphology of µp-Si electrode made by electrochemical etching. (a) top view and (b) side view of the electrode.

Figure 4.2. Cyclic Voltammetric data of of µp-Si and solid-Si. Figures (a-c) illustrate the CV data for solid-Si obtained with a scan rate of 0.5 mV/s, with (b) and (c) showing the enlarged portions of lithiation and delithiation. Figures (d-f) illustrate the CV data for µp-Si, also obtained with a scan rate of 0.5 mV/s, with (e) and (f) showing the enlarged portions of lithiation and delithiation peaks. Figure (g) summarizes the total capacities realized during the CV cycles.

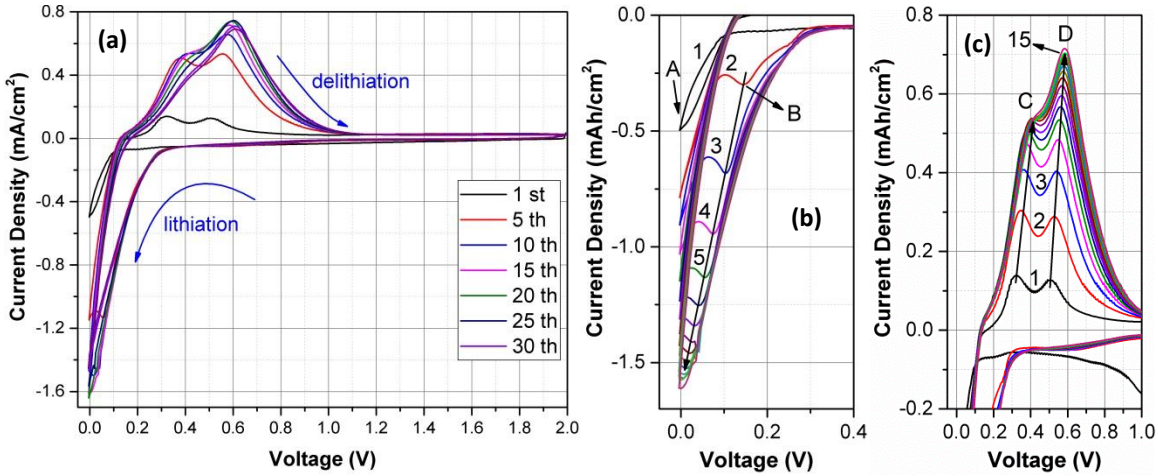
(a)
delithiation
lithiation
1 st
5 th
10 th
15 th
20 th
25 th
30 th
Current Density (mA/cm²)
Voltage (V)
(b)
A
B
1
2
3
4
5
Current Density (mAh/cm²)
Voltage (V)
(c)
15
D
C
1
2
3
Current Density (mAh/cm²)
Voltage (V)

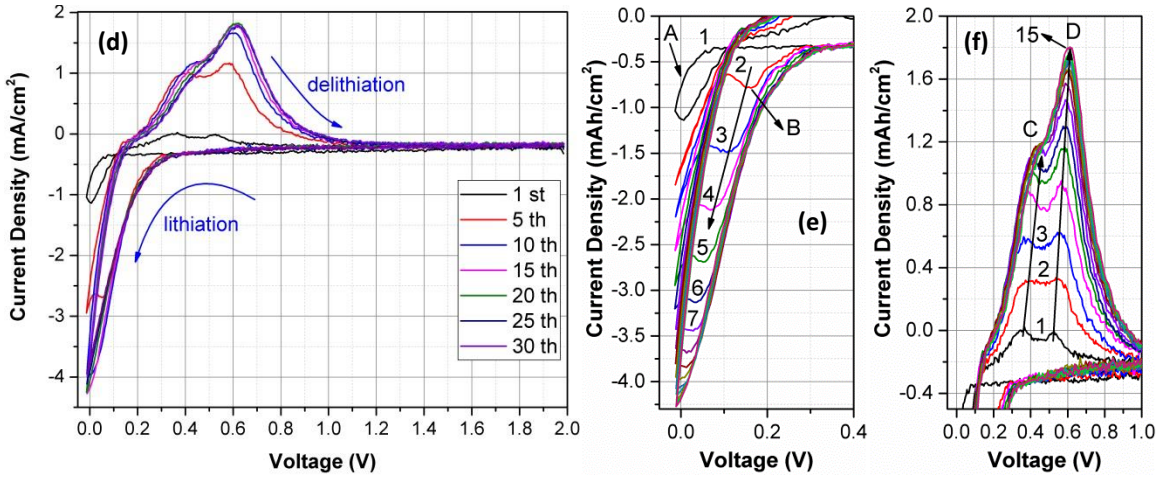
(d)
delithiation
lithiation
1 st
5 th
10 th
15 th
20 th
25 th
30 th
Current Density (mA/cm²)
Voltage (V)
(e)
A
B
1
2
3
4
5
6
7
Current Density (mAh/cm²)
Voltage (V)
(f)
15
D
C
1
2
3
Current Density (mAh/cm²)
Voltage (V)

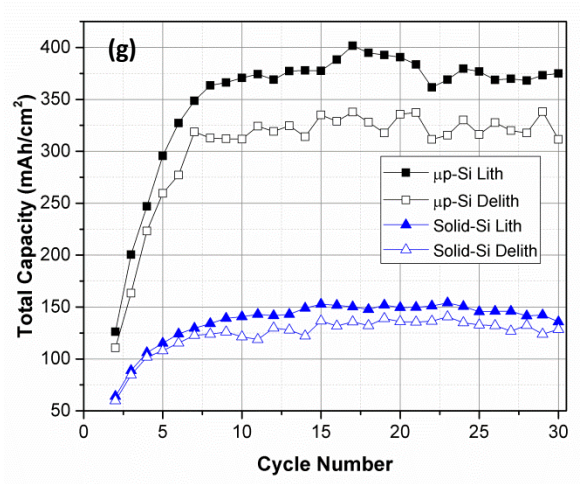
(g)
µp-Si Lith
µp-Si Delith
Solid-Si Lith
Solid-Si Delith
Total Capacity (mAh/cm²)
Cycle Number

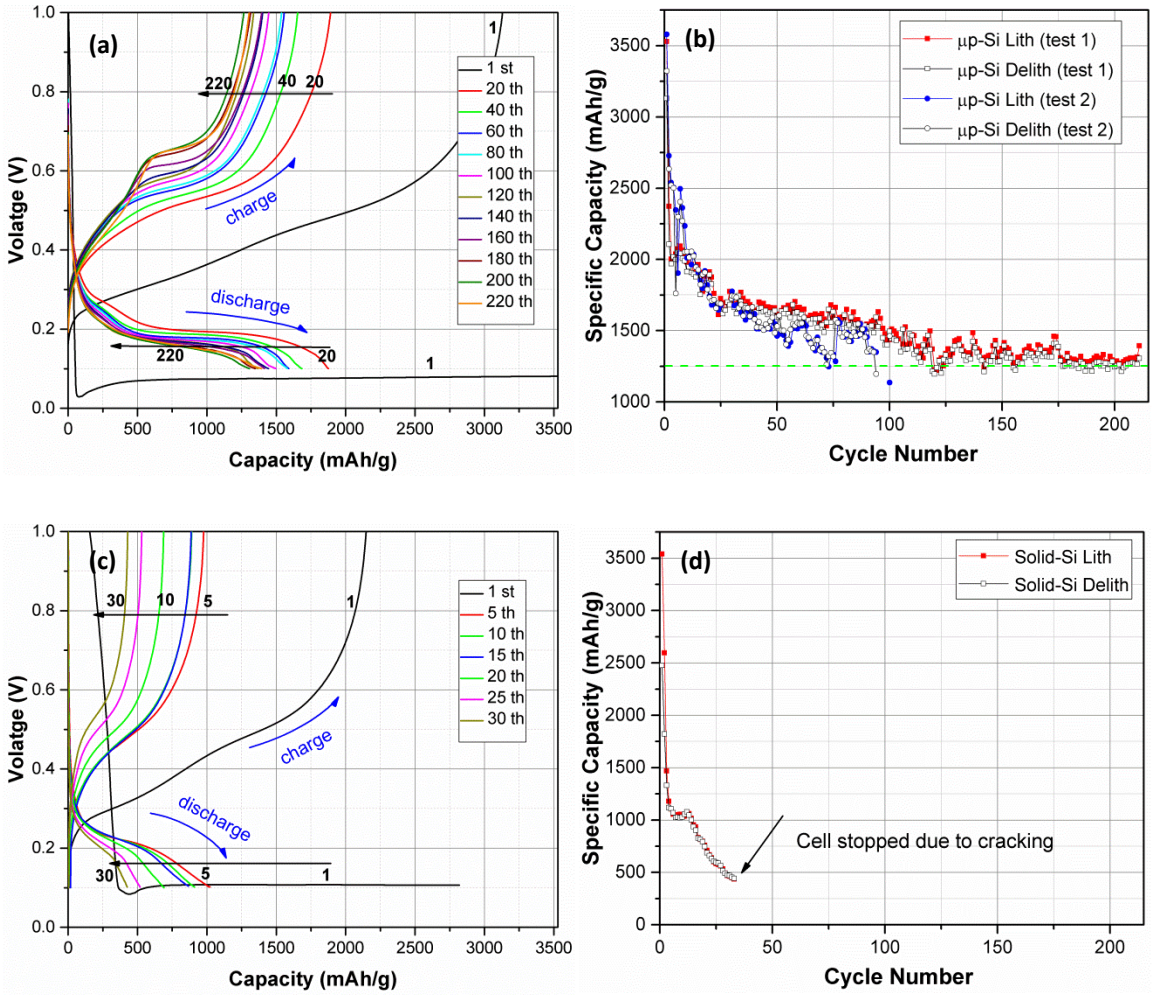

Figure 4.3. Galvanostatic cycling performance of µp-Si and solid-Si. Figures (a & b) show the voltage-versus-capacity curves during cell cycling, and the specific capacity values, as a function of cycle for µp-Si. Figures (c & d) show the voltage-versus-capacity curves during cycling, and the specific capacity values, as a function of cycle for solid-Si.

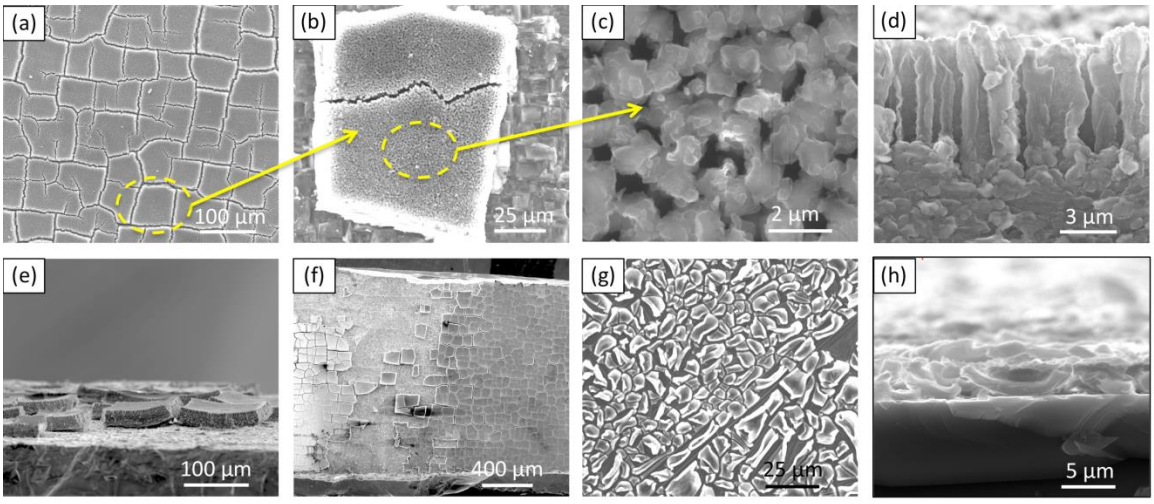

Figure 4.4. Morphologies of µp-Si and solid-Si electrodes after the 220 and 33 galvanostatic cycles respectively. Figures (a-f) are the SEM micrographs for µp-Si morphology and (g-h) are for solid-Si. The µp-Si shows a regular tessellated cracking pattern in (a) with the micropore walls being intact within the islands as shown in (b). The accommodation of volume change by the expansion of lithiated phase within the pore space is seen in (c) with the pore walls being remarkably intact even after cycling for 220 cycles as shown in (d). The tessellated islands in (a) are largely seen to be bonded to the substrate as seen in (e, f) despite the crystallographic cracking pattern. On the other hand, a more extensive cracking and curling of lithiated layer in solid-Si is seen in figures (g) and (h).

Figure 4.5. Structure evolution in µp-Si (100) during lithiation. The figures show (a) a section of µp-Si electrode, (b) the FIB cutting of the Si electrode sample, (c) the sample with the Li_xSi annular regions around pore (indicated by white arrow in (d)), (d) the magnified image of a pore from 'c' showing the locations at which NBD patterns were collected and (e) lattice image showing amorphous structure next to the pore surface, which is confirmed by the FFT image in (f). Figure (g) is a CBED pattern from an area of ~46x46 nm^2 next to the pore surface showing the amorphous structure. Figure (h) is a low magnification image of the structure next to the pore wall. The image in Figure (i) is taken from a location that is ~20 nm from pore surface which shows the amorphous structure embedded with crystalline domains. Figures (j) and (k) illustrate the NBD patterns confirming the progressive transition of the structure of the lithiated region from amorphous to crystalline Si. Figure (m) is a lattice image taken from the unlithiated Si region (with the spot FFT image shown in inset) conforming its crystallinity.

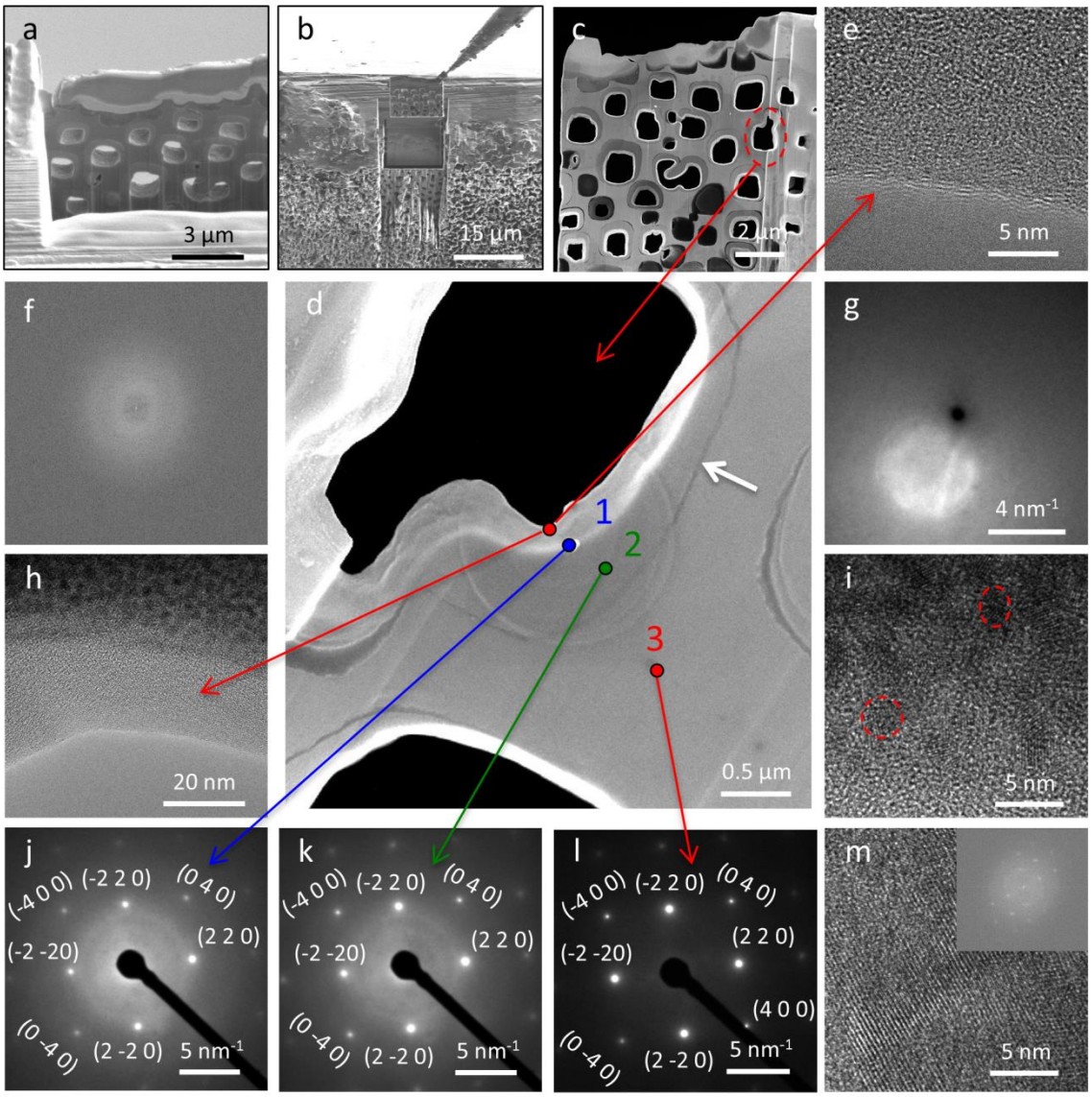
a
3 µm
b
15 µm
c
2 µm
e
5 nm
f
d
g
4 nm-1
1
2
3
h
20 nm
0.5 µm
i
5 nm
j
(-4 0 0)
(-2 2 0)
(0 4 0)
(2 2 0)
(-2 -20)
(0 -4 0)
(2 -2 0)
5 nm-1
k
(-4 0 0)
(-2 2 0)
(0 4 0)
(2 2 0)
(-2 -20)
(0 -4 0)
(2 -2 0)
5 nm-1
l
(-4 0 0)
(-2 2 0)
(0 4 0)
(2 2 0)
(-2 -20)
(4 0 0)
(0 -4 0)
(2 -2 0)
5 nm-1
m
5 nm

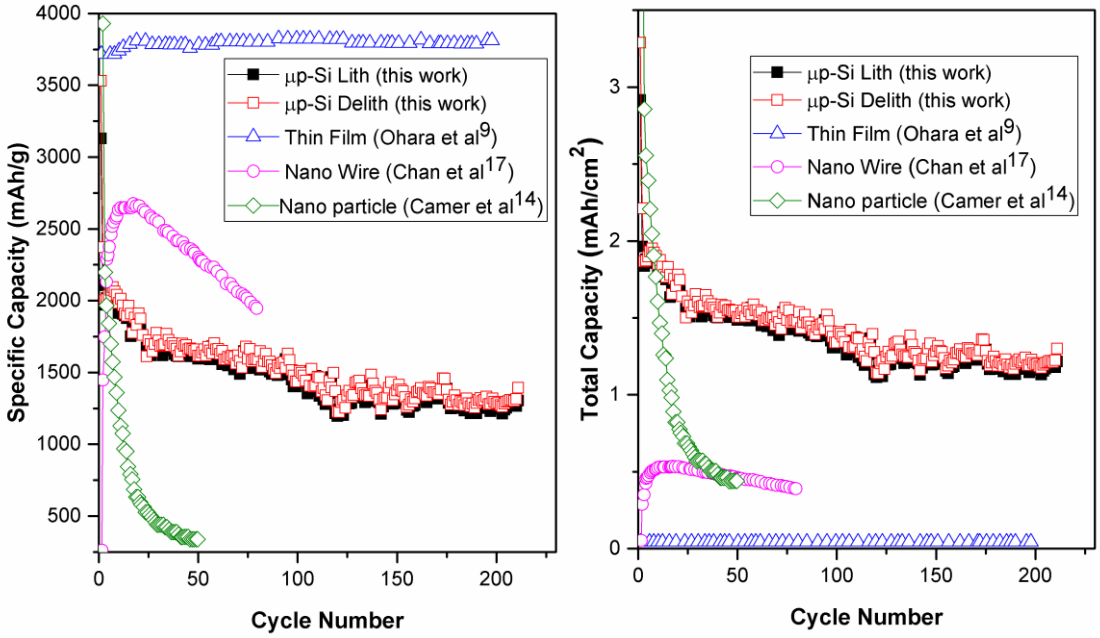

Figure 4.6. Evaluation of the performance of µp-Si architecture against the other forms of Si including thin films, nanowires, and nanoparticle electrodes. Figure (a) is in terms of mass-specific-capacity (mAh/g) as a function of cycle and Figure (b) is in terms of the total energy storage capacity (defined as mAh/cm^2) as a function of cycles. The remarkably superior performance of µp-Si is evident from the comparison made in terms of total capacity.

4.6 References

1. H.Qu, *J. Micromachines*, **7**, 14 (2016).
2. P. S. Waggoner and H. G. Craighead, *Lab Chip*, **7**, 1238 (2007).
3. D. A. LaVan, T. McGuire, and R. Langer, *Nat. Biotechnol*., **21**, 1184 (2003).
4. T. Adams, *Automatic implantable defibrillator and pacer*, US4693253A (1987).
5. N. M. Elman, H. L. Ho Duc, and M. J. Cima, *Biomed Microdevices*, **11**, 625 (2009).
6. P. Koeneman, I. Busch-Vishniac, and K. Wood, *J. Microelectromech. Syst*., **5**, 355 (1997).
7. Y. Brunet, *Energy Storage*, p. 87, John Wiley & Sons, Inc., USA (2009).
8. A. Patil, V. Patil, D. W. Shin, J. W. Choi, D. S. Paik, and S. J. Yoon, *Mater. Res. Bull*., **43**, 1913 (2008).
9. S. Ohara, J. Suzuki, K. Sekine, and T. Takamura, *J. Power Sources*, **136**, 303 (2004).
10. T. Takamura, S. Ohara, M. Uehara, J. Suzuki, and K. Sekine, *J. Power Sources*, **129** 96 (2004).
11. X. Su, Q. Wu, J. Li, X. Xiao, A. Lott, W. Lu, B. W. Sheldon, and J. Wu, *Adv. Energy Mater*., **4**, 1300882 (2014).
12. J. W. Wang, Y. He, F. Fan, X. H. Liu, S. Xia, Y. Liu, C. T. Harris, H. Li, J. Y. Huang, S. X. Mao, and T. Zhu, *Nano Lett*., **13**, 709 (2013).
13. J. P. Maranchi, A. F. Hepp, A. G. Evans, N. T. Nuhfer, and P. N. Kumta, *J. Electrochem. Soc*., **153**, A1246 (2006).
14. J. L. G. Camer, J. Morales, and L. Sanchez, *Electrochem. Solid-State Lett*., **11**, A101 (2008).
15. H. Li, X. Huang, L. Chen, Z. Wu, and Y. Liang, *Electrochemical and Solid-State Letters*, **2**, 547 (1999).
16. M. N. Obrovac and L. J. Krause, *J. Electrochem. Soc*., **154**, A103 (2007).
17. C. K. Chan, H. Peng, G. Liu, K. McIlwrath, X. F. Zhang, R. A. Huggins, and Y. Cui, *Nature nanotechnology*, **3**, 31 (2007).
18. K. Peng, J. Jie, W. Zhang, and S. T. Lee, *Appl. Phys. Lett.*, **93**, 033105 (2008).

19. C. K. Chan, R. N. Patel, M. J. O'Connell, B. A. Korgel, and Y. Cui, *Acs Nano*, **4**, 1443 (2010).

20. T. Song, J. Xia, J. H. Lee, D. H. Lee, M. S. Kwon, J. M. Choi, J. Wu, S. K. Doo, H. Chang, W. I. Park, D. S. Zang, H. Kim, Y. Huang, K. C. Hwang, J. A. Rogers, and U. Paik, *Nano Lett*., **10**, 1710 (2010).

21. M. R. Zamfir, H. T. Nguyen, E. Moyen, Y. H. Lee, and D. Pribat, *J. Mater. Chem.A*, **1**, 9566 (2013).

22. S. W. Lee, M. T. McDowell, L. A. Berla, W. D. Nix, and Y. Cui, *Proc. Natl. Acad. Sci. U. S. A.*, **109**, 4080 (2012).

23. H. T. Nguyen, F. Yao, M. R. Zamfir, C. Biswas, K. P. So, Y. H. Lee, S. M. Kim, S. N. Cha, J. M. Kim, and D. Pribat, *Adv. Energy Mater.*, **1**, 1154 (2011)

24. W. L. Jeffrey, B. Dunn, D. R. Rolison, and H. S. White, *Chem. Rev*., **104**, 4463 (2004).

25. Y. Gogotsi and P. Simon, *Science*, **334**, 917 (2011).

26. A. Harraz, K. Kamada, K. Kobayashi, T. Sakka, and Y. H. Ogata, *J. Electrochem. Soc*., **152**, C213 (2005).

27. A. Vyatkin, V. Starkov, V. Tzeitlin, H. Presting, J. Konle, and U. König, *J. Electrochem. Soc*., **149**, G70 (2002).

28. K. Kang, H. S. Lee, D. W. Han, G. S. Kim, D. Lee, G. Lee, Y. M. Kang, and M. H. Jo, *Appl. Phys. Lett.*, **96**, 053110 (2010).

29. W. J. Weydanz, M. Wohlfahrt-Mehrens, and R. A. Huggins, *J. of Power Sources*, **81–82**, 237 (1999).

30. C. K. Chan, H. L. Peng, G. Liu, K. McIlwrath, X. F. Zhang, R. A. Huggins, and Y. Cui, *Nat. Nanotechnol*., **3**, 31 (2008).

31. M. Green, E. Fielder, B. Scrosati, M. Wachtler, and J. S. Moreno, *Electrochem. Solid-State Lett.*, **6**, A75 (2003).

32. H. C. Shin, J. A. Corno, J. L. Gole, and M. Liu, *J. Power Sources*, **139**, 314 (2005).

33. Y. He, X. Yu, Y. Wang, H. Li, and X. Huang, *Adv. Mater*., **23**, 4938 (2011).

34. A. George and G. Michot, *Mater. Sci. Eng. A*, **164**, 118 (1993).

35. H. Shina, J. A. Cornob, J. L. Goleb, and M. Liua, *J. Power Sources*, **139**, 314 (2005).

36. H. C. Shin, Z. Shi, L. T. Seals, J. L. Gole, and M. Liu, *J. Power Sources*, **139**, 314 (2005).

37. X. Sun, H. Huang, K. Chu, and Y. Zhuang, *J. Electron. Mater.*, **41**, 2369 (2012).

38. D. Kang, J. A. Corno, J. L. Gole, and H. Shina, *J. Electrochem. Soc.*, **155**, A276 (2008).

39. M. Thakur, M. Isaacson, S. L. Sinsabaugh, M. S. Wong, and S. L. Biswal, *J. Power Sources*, **205**, 426 (2012).

CHAPTER 5

ELECTRON MICROSCOPIC STUDY OF LITHIATION IN MICROPOROUS SILICON ELECTRODE

5.1 Introduction

The increased demand for development of energy storage devices for application in hybrid electric vehicles and portable electronics like mobile phones, laptops, and ipads has led to the design of Li-ion batteries with even higher storage capacities. Silicon is considered to be a potential negative electrode material due to its higher capacity (3580 mAh/g), which is ten times higher than commercially used graphite (330 mAh/g).[1] The huge volume expansion (~300% for $Li_{4.4}Si$) occurring during lithiation of Si leads to volumetric and structural changes that cause capacity fading due to mechanical fracture/delamination of electrode particles. In the past, the issue has been partially solved by employing nanostructure electrodes such as nano particles, thin films, nanowires,[2,3,4] nano tubes, and so on. Additionally, the electrodes can be cycled at higher cycling rates due to shorter diffusion lengths.[5] The development of high performance Si nanostructures is only possible by the proper understanding of the phase transitions, volume expansion, stresses, and fracture aspects occurring during cycling.[6]

The lithiation in crystalline Si particles occurs via a two phase mechanism: Si transforms to a-Li_xSi and finally below 50 mV vs Li/Li^+ [7,8] to crystalline $Li_{15}Si_4$ phase. The volume expansion results in loss of electrical contact with current collector, leading to poor cycling capacities in the range of 400-600 mAh/g.[9] The pulverization can be mitigated by limiting the upper and lower cut-off voltage limits—lower degrees of lithiation causes lower volumetric strains that can be accommodated in the structure.[10] The volumetric expansion can also be buffered by adding electrochemically inactive matrices and conductive additives. The cycling capacities can be improved, but the energy storage density, the most important characteristic of electrode material, is reduced.

The use of inactive carbon as a matrix, like XE2 carbon black and Super P carbon, were found to improve the cycling capacities to around 1800 mAh/g.[11] The advantages of using carbon black are threefold: improved conduction due to its high electrical conductivity, ability to accommodate huge volumetric strains due to its high ductility, and ability to form a stable SEI layer with conventionally used organic electrolytes.

Silicon nanowires[12] and nanotubes[13] have demonstrated huge discharge capacities, around 3400 mAh/g over a few tens of cycles. The structures provide free space for accommodating the facile strains during cycling. The facile strain relaxation in nanowires is experimentally observed by partially coating with electrochemically inactive nickel.[12] After lithiation, nanowires were found to have changed shape and wrapped in a three dimensional manner around the nickel backbone. Silicon nanotubes were found to show discharge capacities above 2600 mAh/g and 2100 mAh/g for over 50 cycles at C-rates of C/20 and C/5, respectively.[13] The cycling is due to the accommodation of highly anisotropic volume expansion of ~120% in radial direction (into and out of inner and outer free surfaces) and ~35% in axial direction.

Apart from volume expansion, the phase transitions occurring during cycling of Si electrodes also seriously affects its electrochemical performance. The formation of $Li_{15}Si_4$ that occurs during lithiation of a-Si below 50 mV was found to be detrimental to cycling performance.[14]

We very recently demonstrated that μp-Si fabricated by cheaper electrochemical route shows exceptionally high cycling capacities of ~1250 mAh/g over 220 cycles. The scope of the current research is to study the process of lithiation occurring in μp-Si using electron microscopy. In particular, how the huge volume expansion is accommodated in

the pores is studied. The phase transitions occurring during cycling are studied in detail using Transmission Electron Microscopy (TEM).

5.2 Experimental Procedure

The Si (100) wafers used for the experiment were of 7 Ω-cm resistivity supplied by University Wafers, MA, USA. The electrical contact to Si was made by sputtering 400 nm thick Cu, using the Denton SJ20C sputtering device, and annealing at 500ºC for 1 hr under vacuum. The µp-Si electrodes were prepared using an electrochemical etching route. The electrochemical etching was carried out using an etching cell made of teflon. The working electrode and counter electrode used were Si and Pt, respectively. The electrolyte with the composition HF:DMF = 1:10 was used. The etching was carried out at a current density of 3 mA/cm^2 for 1 hr using the KEITHLEY, 2601B Sourcemeter. The µp-Si electrodes were electrochemically cycled at a C-rate of C/10 for 221 lithiation cycles using a swage lock cell. The µp-Si electrodes after cycling were thoroughly rinsed with DEC for 20 min inside a glovebox to remove electrolyte residue. SEM micrographs were captured for the µp-Si electrodes before and after cycling. FIB experiments were performed using FEI Helios 650. Transmission Electron Microscopy (TEM) imaging and diffraction were conducted using JEOL JEM 2800. The Nano Beam Diffraction (NBD) patterns were collected from an area of 230 nm x 230 nm.

5.3 Results and Discussion

The SEM micrographs of representative µp-Si sample containing uniformly distributed pores (constituting 50% porosity) which are 1.1 µm in diameter and 8 µm in

depth are shown in Figure 5.1. The sample was cycled galvanostatically at C-rate of C/10 for 221 lithiation cycles. The post cycled SEM micrographs showing the top view and side view of the sample, after 221 lithiation cycles, is shown in Figure 5.2a and 5.2b, respectively. The process of lithiation in Si is associated with huge volumetric expansion, which is manifested as a decrease in porosity to 10% (Figure 5.2a) from the initial 50% (Figure 5.1a) and swelling of pore walls (Figure 5.2b).

To understand how the volume expansion is accommodated in the pores, the pores were sectioned vertically and imaged, using the FIB technique (Figure 5.3). The cross section of the lithiated µp-Si (Figure 5.3b) was observed by removing the material from the island structure (Figure 5.3a) formed during cycling. The lithiation was observed to have occurred uniformly all along the depth of the pore (Figure 5.3b-d). The final diameter of the pore, on average, is around 500 nm. The lithiated Si assumed a nodular morphology towards the end of the process of filling the pore. The system has assumed nodular morphology to minimize its overall free energy—the surface energy contribution is minimized as spheres have minimum surface area compared with all shapes for the given volume. Most importantly, it was noticed that lithiation didn't occur into the base (Figure 5.3b), which is the reason why the base is not included in the calculation of gravimetric capacity in Chapter 4. This is in agreement with the work of Thakur et al.,[15] who showed that base is not affected during lithiation, using XRD. It is expected because if the base had been affected by lithiation, the morphology would have shown ultra-poor cycling performance like flat Si.

The nature of the phase transitions occurring in µp-Si upon cycling was investigated using TEM in imaging and diffraction modes. The TEM sample prepared by FIB

technique is shown in Figure 5.4a. The magnified bright field TEM image of the representative pores A and B chosen is shown in Figure 5.4b and 5.4c, respectively. The boundary of pores A and B is marked in yellow (Figure 5.4b and 5.4c). The edges of material that grew into the original pore, due to volume expansion, has a wavy structure. It is the same as the cross-section of the nodular structure observed in Figure 5.3b-5.3d.

The structural changes that occurred due to lithiation were investigated by collecting Nano Beam Diffraction (NBD) patterns from the region around pore A to the region around pore B, with several locations in between (Figure 5.5). The NBD patterns collected from material grown into original pores show spotty patterns (Figure 5.5b, 5.5c and 5.5g), conforming the structure to be crystalline in nature. However, the NBD patterns from regions in between pores show a spotty pattern with diffuse rings, confirming the structure to be a mixture of crystalline plus amorphous phase mixtures in nature. The phase constitution in the crystalline regions next to pores A and B was determined using HRTEM imaging (Figure 5.6). The HRTEM images collected next to pores A and B are shown in Figure 5.6a and 5.6c respectively. The presence of lattice in both images confirms the crystalline nature. The FFT images corresponding to Figures 5.6a and 5.6c (show spotty pattern), which further confirms the crystallinity, are shown in Figure 5.6b and 5.6d respectively. The spots A, B, D, E, G, H, I, J, and L in Figure 5.6b correspond to Si phase, and the spots C, F, and K correspond to $Li_{15}Si_4$. The spots A, B, C, E, F, H, and I in Figure 5.6b correspond to Si phase, and those from spots D and G correspond to $Li_{15}Si_4$. The region grown into the pore therefore has crystalline Si and crystalline $Li_{15}Si_4$ phases.

The preferred orientation of the crystalline Si grown into pore was determined by

collecting SADP (Figure 5.7). The bright field TEM image showing both the pores A and B with the original pore boundary (marked in yellow) is shown in Figure 5.7a. The dark field image corresponding to the diffraction spots (2 -2 0), (220), and (040) is shown in Figure 5.7b, 5.7c, and 5.7d. The material grown into the original pore shows a greater number of brighter regions in (2 -2 0) compared to (220) and (040). This means that Si (2 -2 0) grains are preferentially oriented.

5.4 Conclusions

1. The volume expansion associated with lithiation was found to be uniformly accommodated throughout the depth of the pore.
2. The lithiation occurs only along pore walls but not into the base of Si. The calculation of gravimetric capacity, therefore, doesn't need the base to be included.
3. µp-Si assumes a duplex microstructure: (a) "crystalline Si + $Li_{15}Si_4$" in the region which grew into the original pore, and (b) "crystalline Si + amorphous Li_xSi" in the region between pores. The region around the pore shows preferential orientation of Si (2 -2 0) grains.

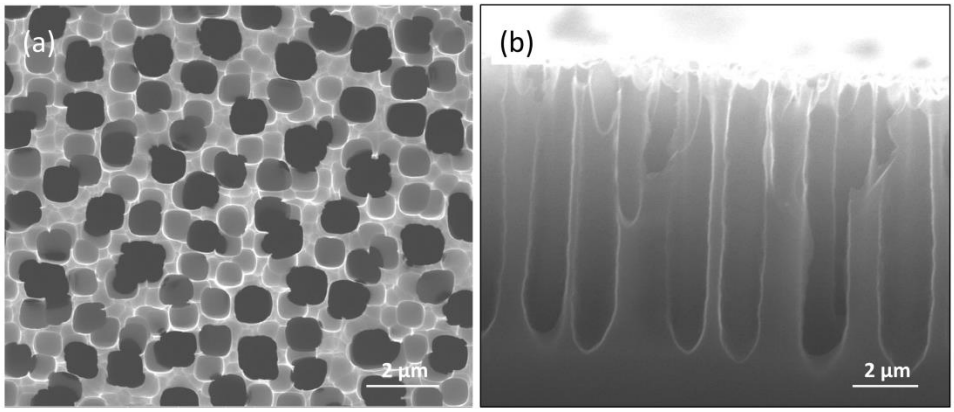

Figure 5.1. SEM micrograph showing (a) top view and (b) side view of µp-Si made by electrochemical route.

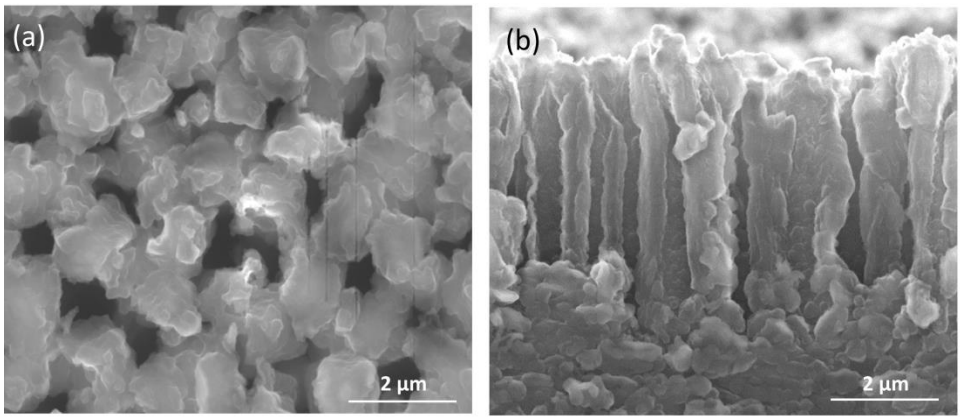

Figure 5.2. SEM micrograph showing (a) top view and (b) side view of µp-Si cycled for 220 cycles.

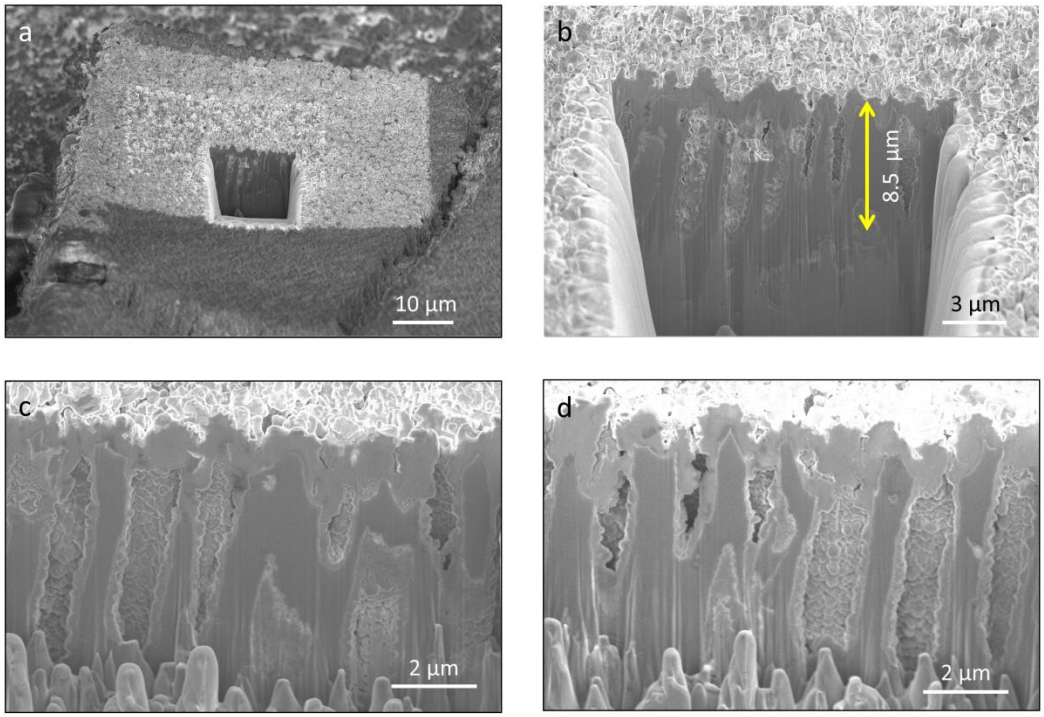

Figure 5.3. FIB cross-section images collected from sample cycled for 221 lithiation cycles. (a) The representative island chosen to observe the cross-section, (b) Si base is not at all affected by lithiation and all the volume expansion, due to lithiation, accommodated by the pores, and (c-d) the lithiated material that grew into the pores assumes nodular morphology and is uniform all along the pore depth. Because of the inclination of the sectioned plane, the actual depth of lithiation (which is indicated) was determined by dividing the unit length in the micrograph by cos (52°).

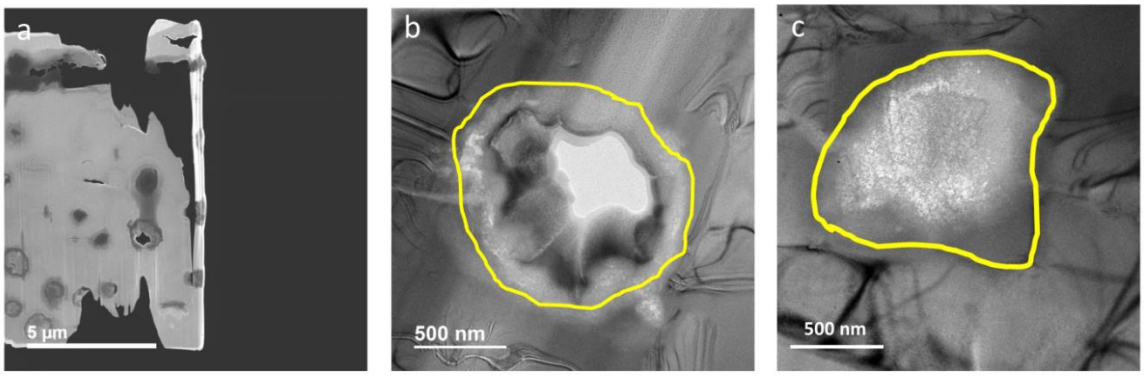

Figure 5.4. Electron microscopy images showing pores A and B in the sample cycled for 221 lithiation cycles. (a) FIB cut sample showing the representative pores A and B choosen to study the phase transitions duirng cyclcing and (b,c) Magnified TEM images of representative pores A and B. The pore boundary before lithiation is marked in yellow.

Figure 5.5. Structural evolution in µp-Si cycled for 221 lithiation cycles. (a) Bright Field TEM image showing pores A and B chosen for the study, (b,c) NBD patterns collected from the material that grew into pore A, (c-f) NBD patterns collected from material that swelled into pore B, and (g) NBD patterns collected from material that swelled into pore B. The regions from which NBD patterns b,c,g are collected are crystalline in nature, whereas the region from which c-f are collected are crystalline + amorphous in nature.

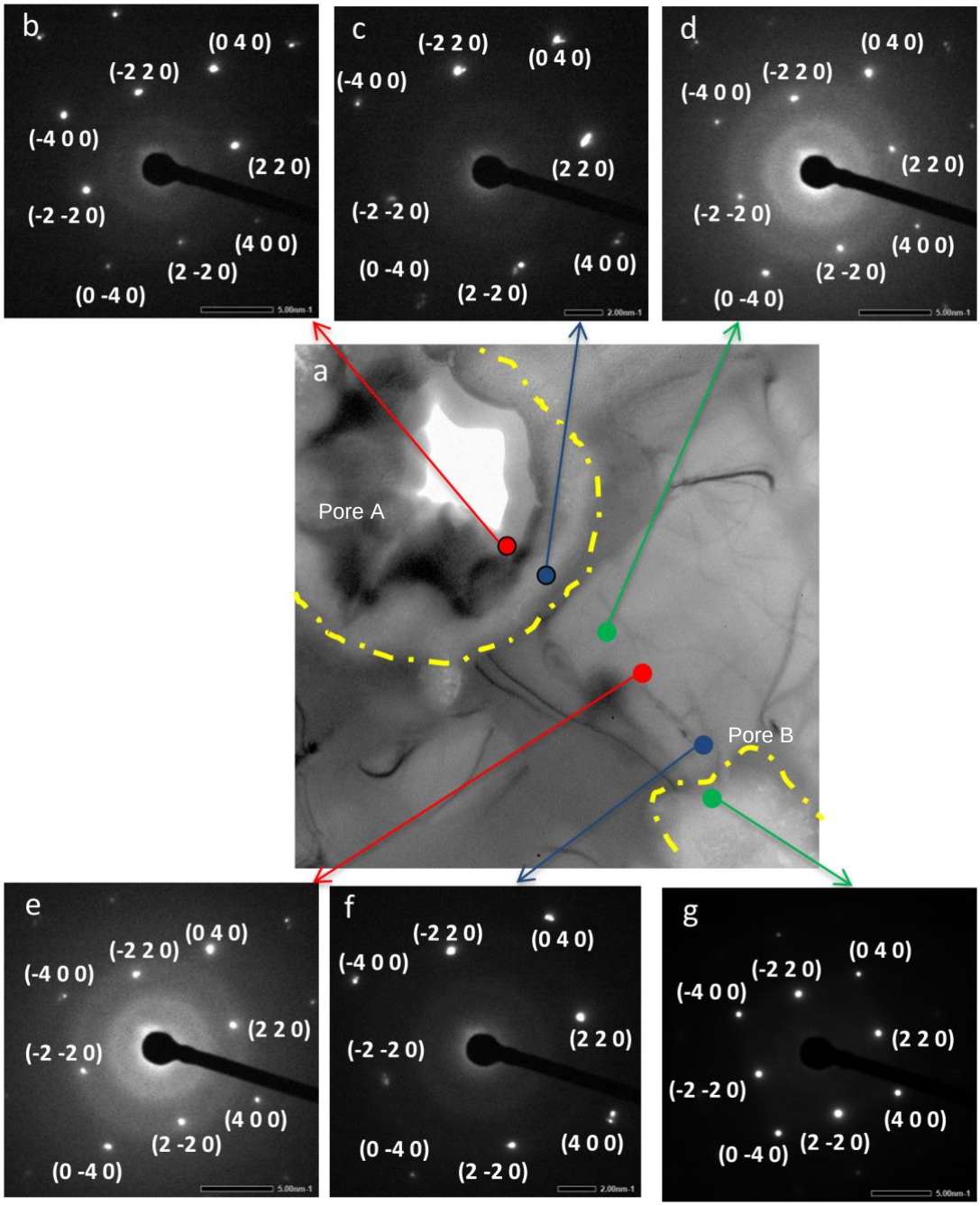
b
(0 4 0)
(-2 2 0)
(-4 0 0)
(2 2 0)
(-2 -2 0)
(4 0 0)
(2 -2 0)
(0 -4 0)
c
(-2 2 0)
(0 4 0)
(-4 0 0)
(2 2 0)
(-2 -2 0)
(0 -4 0)
(4 0 0)
(2 -2 0)
d
(0 4 0)
(-2 2 0)
(-4 0 0)
(2 2 0)
(-2 -2 0)
(4 0 0)
(2 -2 0)
(0 -4 0)
a
Pore A
Pore B
e
(0 4 0)
(-2 2 0)
(-4 0 0)
(2 2 0)
(-2 -2 0)
(4 0 0)
(2 -2 0)
(0 -4 0)
f
(-2 2 0)
(0 4 0)
(-4 0 0)
(2 2 0)
(-2 -2 0)
(0 -4 0)
(4 0 0)
(2 -2 0)
g
(0 4 0)
(-2 2 0)
(-4 0 0)
(2 2 0)
(-2 -2 0)
(4 0 0)
(0 -4 0)
(2 -2 0)

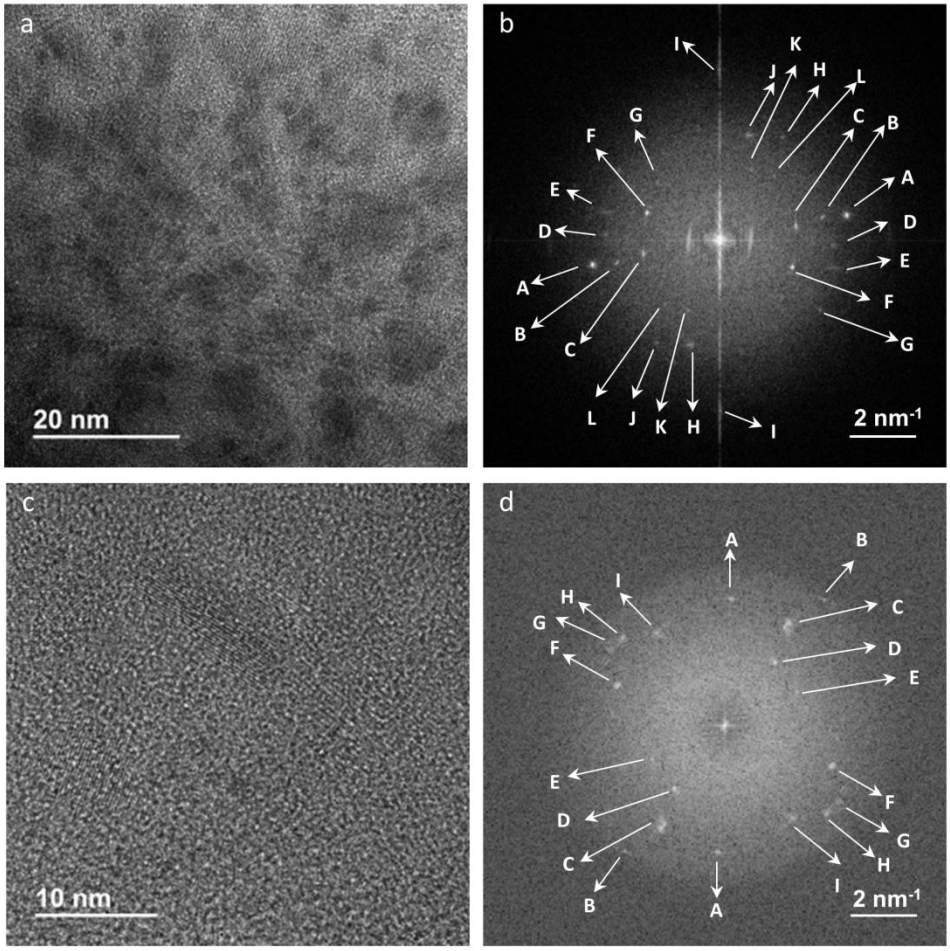

Figure 5.6. HRTEM images with their corresponding FFT patterns. (a, c) HRTEM images from material that swelled into pores A and B (Figure 5.5) and (b, d) FFT images corresponding to HRTEM images a and c.

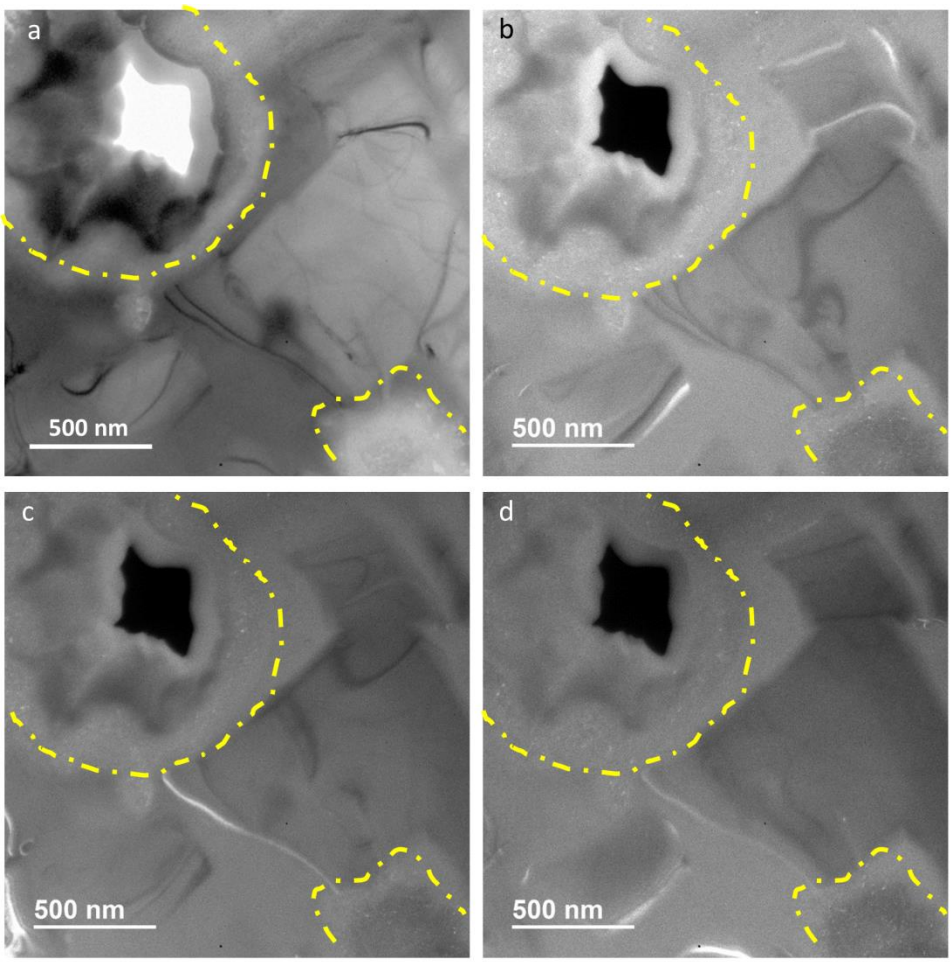

Figure 5.7. Bright Field and Dark Field TEM images of the regions around pores A and B. (a) Bright Field TEM image showing pores A and B chosen for the study and (b-d) Dark Field images corresponding to Si (2 -2 0), Si (220), and Si (040) spots in the SADP pattern.

5.5 References

1. T. D. Hatchard and J. R. Dahn, *J. Electrochem. Soc.*, **151**, A838 (2004).

2. C. K. Chan, H. Peng, G. Liu, K. McIlwrath, X. F. Zhang, R. A. Huggins, and Y. Cui, *Nature Nanotech.*, **3**, 31(2007)

3. K. Peng, J. Jie, W. Zhang, and S. T. Lee, *Appl. Phys. Lett.*, **93**, 033105 (2008).

4. C. K. Chan, R. N. Patel, M. J. O'Connell, B. A. Korgel, and Y. Cui, *Acs Nano*, **4**, 1443 (2010).

5. H. Wu and Y. Cui , *Nano Today*, **7**, 414 (2012)

6. W. J. Zhang, *J. Power Sources*, **196**, 877 (2011).

7. M. N. Obrovac and L. Christensen, *Electrochem. Solid-State Lett.*, **7**, A93 (2004).

8. J. Li and J. R. Dahn, *J.Electrochem. Soc.*, **154**, A156 (2007).

9. A. A. Arie, J. O. Song, and J. K. Lee, *Mater. Chem. Phys.*, **113**, 249 (2009).

10. M. N. Obrovac and L. J. Krause, *J. Electrochem. Soc*., **154**, A103 (2007).

11. J. L. Gomez Camer, J. Morales, L. Sanchez, P. Ruch, S. H. Ng, R. Koetz, and P. Novak, *Electrochim. Acta*, **54**, 6713 (2009).

12. C. K. Chan, H. Peng, G. Liu, K. McIlwrath, X. F. Zhang, R. A. Huggins, and Y. Cui, *Nat. Nanotechnol*., **3**, 31 (2007).

13. T. Song, J. Xia, J. H. Lee, D. H. Lee, M. S. Kwon, J. M. Choi, J. Wu, S. K. Doo, H. Chang, W. I. Park, D. S. Zang, H. Kim, Y. Huang, K. C. Hwang, J. A. Rogers, and U. Paik, *Nano Lett*., **10**, 1710 (2010).

14. M. N. Obrovac and L. Christensen, *Electrochem. Solid-State Lett.*, **7**, A93 (2004).

15. M. Thakur, M. Isaacson, S. L. Sinsabaugh, M. S. Wong, and S. L. Biswal, *J. Power Sources*, **205** 426 (2012).

CHAPTER 6

LITHIATION INDUCED MOSAICITY IN MICROPOROUS COLUMNAR SI (100) BY IN-SITU NEUTRON DIFFRACTION

6.1 Introduction

The pressing need for development of high energy density Li-ion batteries has led to the search for novel electrode materials. Si is an obvious choice because of its very high charge capacity of 3580 mAh/g. However, Si electrodes suffer from capacity degradation because of electrode crumbling due to huge volume expansion associated with lithiation reaction. The volume expansion issue has been mitigated in the past by use of porous electrode materials.

The lithiation of Si involves amorphization of Si lattice accompanied by volume expansion. The process of amorphization was very well studied earlier using XRD,[1] NMR,[2] and TEM[3] techniques. The nature of phase transition in crystalline and amorphous states was very well investigated. However, earlier studies didn't focus well on the changes that occur in the atomic Si-Si bonding in the process of shape change caused by volume expansion. The process can be best studied in real time by use of neutron diffraction, owing to higher depth of penetration of neutrons and their ability to detect Li atoms despite low Z. The current study focuses on the study of changes that occur in microporous Si (µp-Si) electrodes using an in-situ neutron diffraction technique.

6.2 Experimental Procedure

6.2.1 In-Situ Cell Preparation

The copper electrical contact to Si (100) sheet was made using wafer bonding. µp-Si electrode was prepared by electrochemically etching the copper connected to the Si (100) sheet. The in-situ cell configuration assembly (Figure 6.1) consists of one centrally located Li foil, with microfabricated Si (100) electrodes on either side, thereby forming

two parallel cells. A Celgard 3501 separator (25 µm) soaked in electrolyte was placed in between each set of electrodes, and the cell was fully assembled in a He filled glove box. The electrolyte composed was of composition: 1 M $LiPF_6$ in EC:DEC:DMC = 1:1:1 (MTI Corporation, CA, USA). The levels of H_2O and O_2 were kept below 0.1 ppm.

6.2.2 Electrochemical Tests

The electrochemical tests were conducted using Bio-Logic SP-300 potentiostat at VULCAN diffractometer, SNS, ORNL. The µp-Si electrode was lithiated at a current density of 0.05 mA/cm^2 (cycling rate of C/20) for 10 hrs, which corresponds to a lithium content of x = 1.89 per Si atom or a specific capacity of 1790 mAh/g.

6.2.3 VULCAN Diffractometer

VULCAN is an engineering materials time-of-flight diffractometer located at SNS, Oak Ridge National Laboratory, USA. The in-situ diffraction data were obtained by the VULCAN diffractometer using an incident beam (5 mm x 12 mm) of 0.5-3.5 Å band width, allowing the d-space range of 0.5-2.5 Å in the diffracted patterns in the +90º, -90º detectors. Event-based neutron data were collected continuously as the cell was charged to full capacity. ND data was binned every 3600 s and reduced using VDRIVE software.

6.2.4 ND Studies at VULCAN

The in-situ cell was arranged such that the µp-Si electrode made an angle of 44º with the incident beam (Figure 6.2a). As a result, the (400) and (440)/(220) planes in µp-Si electrode were Bragg diffracted into the west detector and east detector, respectively. The corresponding detector images are shown in Figure 6.2b and 6.2c. The presence of two

sets of Si (400) spots (Figure 6.2b), corresponding to two µp-Si electrodes in in-situ cell and Si (111) spot from in-situ cell casing, can be observed on the west bank. Also, two sets of Si (440)/(220) spots (Figure 6.2c), arising from two µp-Si electrodes in the in-situ cell can be observed.

The unique arrangement ensures that any change in the orientation of planes can be tracked by observing the change in the position of spots (each spot corresponds to a Bragg reflection from a plane) on the detector screen. The spots on the detector screen can be processed to obtain the corresponding diffraction pattern. The sample to detector distance used was such that the maximum angle coverage on each detector is 23º (Figure 6.2a).

6.3 Results and Discussion

The microstructure of the microfabricated columnar porous Si (100) electrode is shown in Figure 6.3. The porosity observed was 50%, whereas the pore depth was 12 µm. The plane of electrode is (100) and the pore walls are perpendicular to <01-1> and <011> directions. The electrochemical discharge/charge data obtained during cycling are shown in Figure 6.4.

6.3.1 Neutron Diffraction Studies

The real time ND patterns showing the evolution of Si (400), Si (440), and Cu (200) reflections are shown in Figure 6.5a-c, respectively. The ND patterns were obtained by binning 1 hr of data into one pattern. The intensities of Si (400) and (440) reflections increased gradually and that of Cu (200), obtained from the current collector, remained

the same. The d-spacing and FWHM of the Si (400) and Si (440) reflections remained the same throughout lithiation.

The XRD work of Li et al.[4] and Obrovac et al.[5] suggested that during lithiation, (i) "crystalline-Si" transforms to a "crystalline-Si" + "amorphous-Si" two phase mixture, and (ii) below 50 mV, the two phase mixture crystallizes to $Li_{15}Si_4$, the fully lithiated phase. The peak intensity of Si (400) and Si (440) reflections must decrease and FWHM must increase, if such a phase transition is to occur. To understand the reason for intensity increase with no change in d-spacing and FWHM, the position of spots on the detector corresponding to Si (400) and Si (440) were observed. This is accomplished by construction of a 2D projection map, which is a plot between d spacing and the spread of spots (angle subtended by edges of spot at center of the sample) on the detector (Figure 6.6 and 6.7). The (400) spot (Figure 6.6) and (440) spot (Figure 6.7) were found to be spreading with lithiation. This gives an indication about lattice becoming mosaic due to lithiation. The variation of intensity across (400) spots in Figure 6.6 is shown Figure 6.8. The evolution of mosiacity as lithiation proceeds can be accessed by calculating the FWHM for these plots. The FWHM was found to increase with lithiation, indicating mosaicity. The increase in the intensity of Si (400), (440) reflections during lithiation also confirms the mosaicity (Figure 6.9).

6.3.2 Electron Diffraction and Imaging Studies

The presence of mosaicity was further confirmed by conducing TEM imaging and diffraction (Figure 6.10 & 6.11). The electron diffraction patterns (Figure 6.10d-f) collected from the region in between pores showed amorphous + crystalline structure. It

was interesting to note that an additional diffraction spot was present at each Si reflection. This is an indication of the presence of crystals being separated from each other by a small angle or the presence of the mosaic structure. The HRTEM image (Figure 6.11a) obtained from the region grown into pore B (Figure 6.10) shows a lattice structure, and this confirms the structure is crystalline. The FFT of lattice image in Figure 6.11a is shown in Figure 6.11b. The spots A-I (in Figure 6.11b) with their corresponding interplanar spacing values are shown in Table 6.1. The percentage change in the interplanar spacing value, obtained by comparing against theoretical, is also tabulated in Table 6.1. The interplanar spacing for Si (111) (spot C) is 7% less than the theoretical value, indicating distortion in lattice. Moreover, the spot C that corresponds to the Si (111) plane shows huge spread indicating the mosaic nature of {111} planes. The spread of spot C is large in comparison with other Si spots F and H. This is in agreement with the lithiation model proposed by S. W. Lee et al.[6]

S. W. Lee et al.[6], in their work, proposed that Li diffusion in Si is highest along <110> direction, as it offers least activation energy due to maximum spacing amongst the Si atoms (Figure 6.12). In order to study Li diffusional anisotropy in Si (100), they held Li foil and Si (100) sheet in intimate contact for 5 hrs. The cross-sectional SEM micrograph is shown in Figure 6.13.[6] The bright contrast region shows that Li diffusion occurs parallel to {111} planes and Si-Si bonds across {111} planes are broken. It was inferred that, during lithiation as Li diffuses in Si (100) along <110> direction, the Si-Si bonds across {111} planes are broken.[6] As a result, microcracks are formed parallel to {111} planes, causing the collapse of {111} planes, resulting in mosaicity in crystal structure (Figure 6.14).

The collapse of {111} planes must result in partial distortion in lattice structure and result in reduced interplanar spacing of other planes. This was found to be consistent with reduced interplanar spacing of the (200) planes coming from spots E and H (Table 6.1).

6.4 Conclusions

1. We could successfully observe the crystallographic changes occurring in the Si lattice during lithiation from pores just 12 μm in depth.
2. Neuron diffraction coupled with TEM studies established that the Si lattice becomes mosaic during the process of lithiation.

Table 6.1. The crystal planes corresponding to spots A to I in FFT shown in Figure 6.10b. The interplanar spacing is compared to that of theoretical values.

Spot	(h k l)	$d_{(hkl)\text{-experimental}}$ (Å)	$d_{(hkl)\text{-theoretical}}$ (Å)	% Change against theoretical value
A	Si (200)	2.7	2.71	-0.37
B	Si (200)	2.5	2.71	-7.75
C	Si (111)	2.9	3.13	-7.34
D	$Li_{15}Si_4$ (211)	4.26	4.35	-2.07
E	Si (200)	2.5	2.71	-7.75
F	Si (111)	3	3.13	-4.15
G	$Li_{15}Si_4$ (211)	4.26	4.35	-2.07
H	Si (200)	2.54	2.71	-6.27
I	Si (111)	2.97	3.13	-5.11

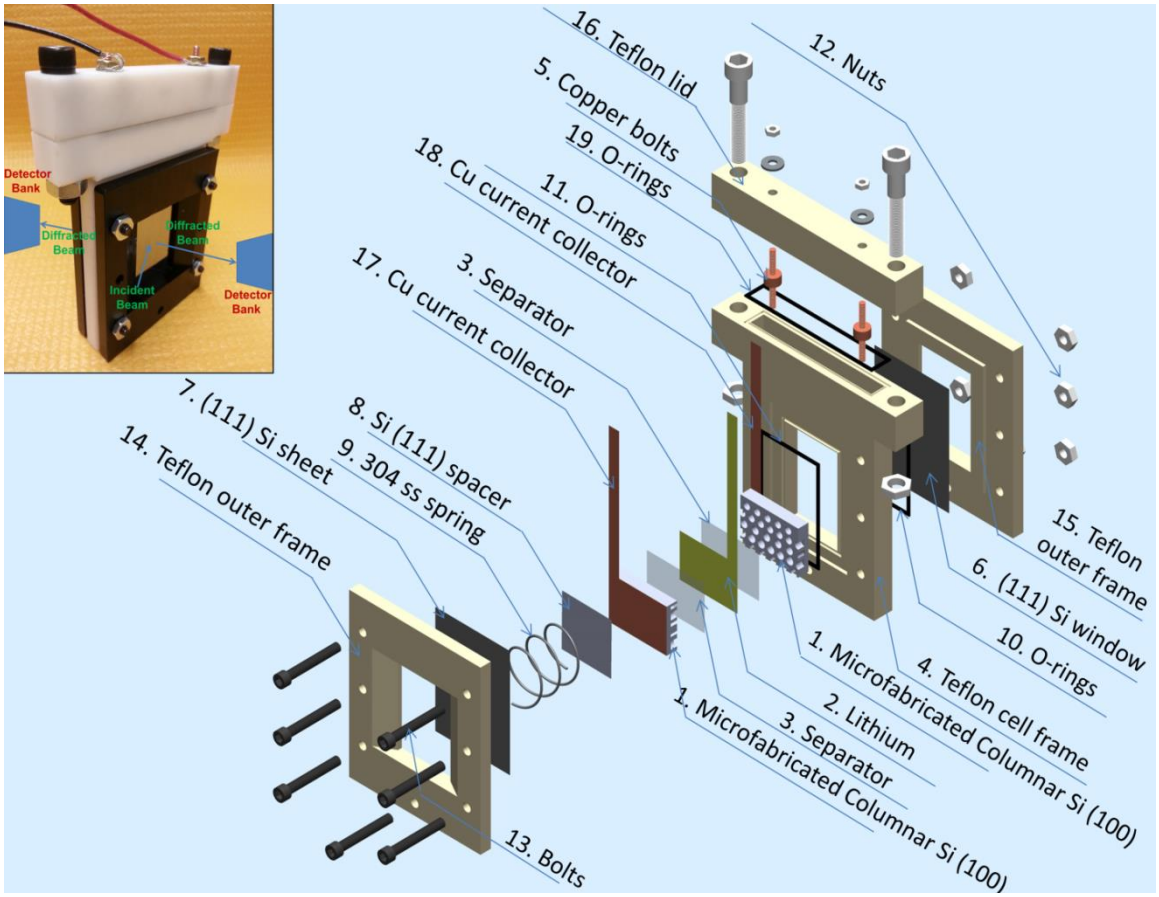

Figure 6.1. Exploded view of the in-situ electrochemical cell showing various components.

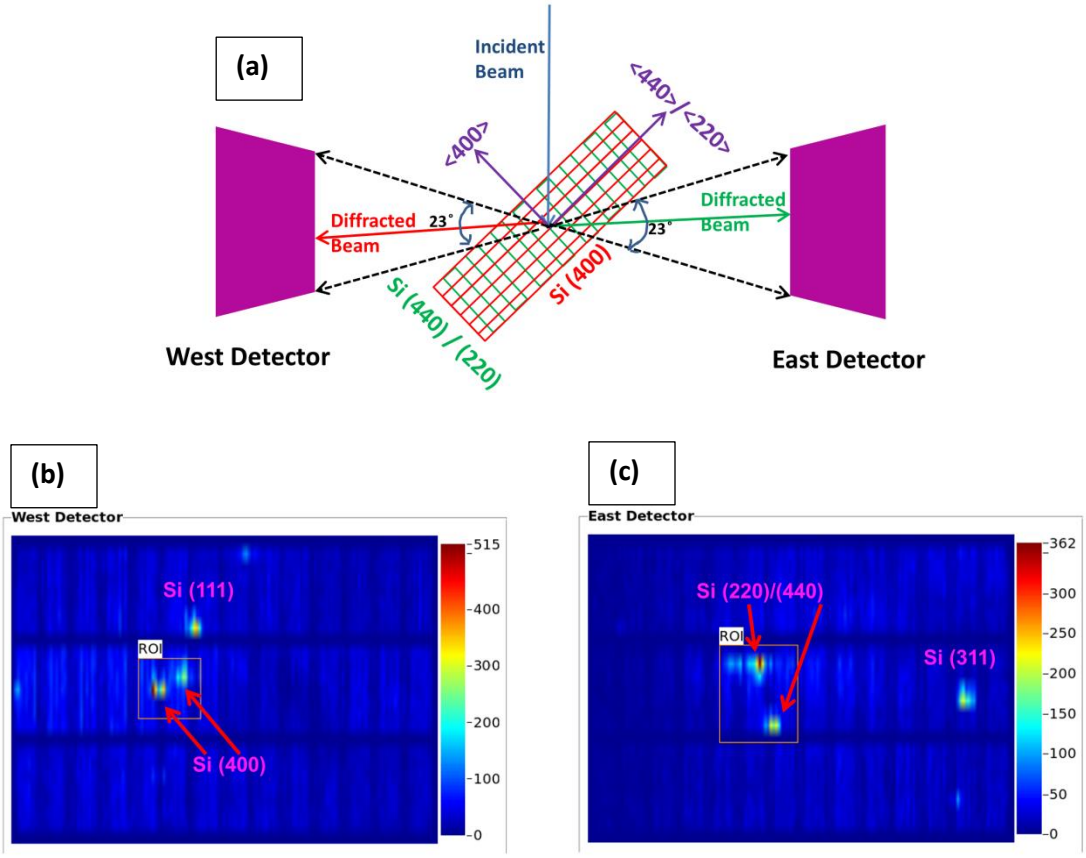

Figure 6.2. In-situ neutron diffraction at VULCAN diffractometer, SNS, ORNL. (a) The experimental arrangement where incident neutron beam interacts with sample and the signal from Si (400) gets diffracted into the west detector and that from Si (440)/(220) into the east detector. (b) The west detector shows spots corresponding to Si (400), Si (111) spots, and (c) east detector shows spots corresponding to Si (220)/(440), Si (311) reflections.

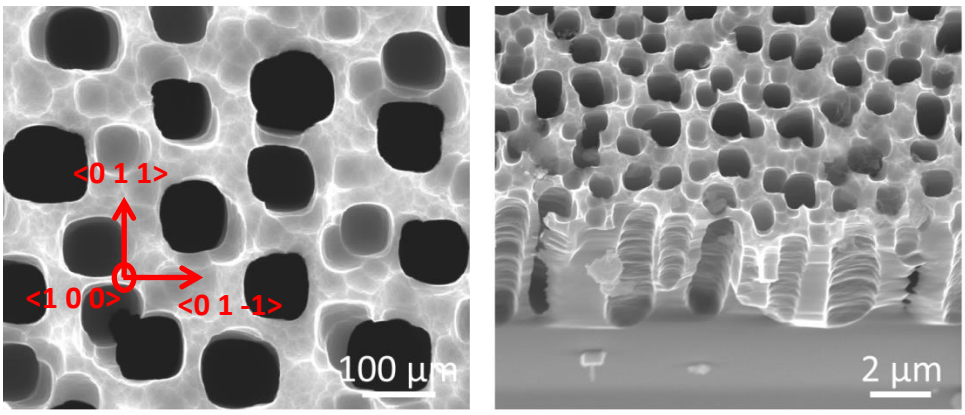

Figure 6.3. SEM micrograph of the microfabricated µp-Si (100) electrode.

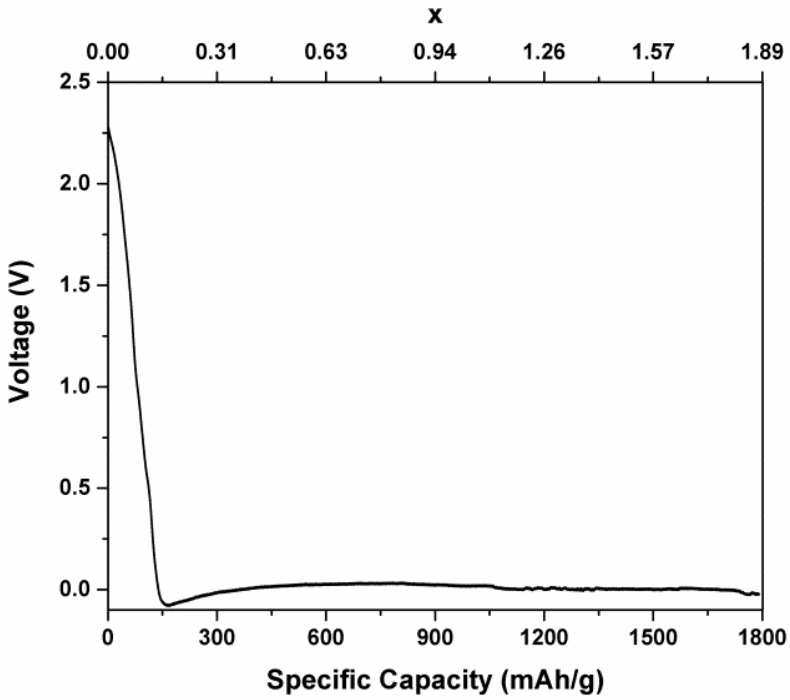

Figure 6.4. Electrochemical cycling data of µp-Si.

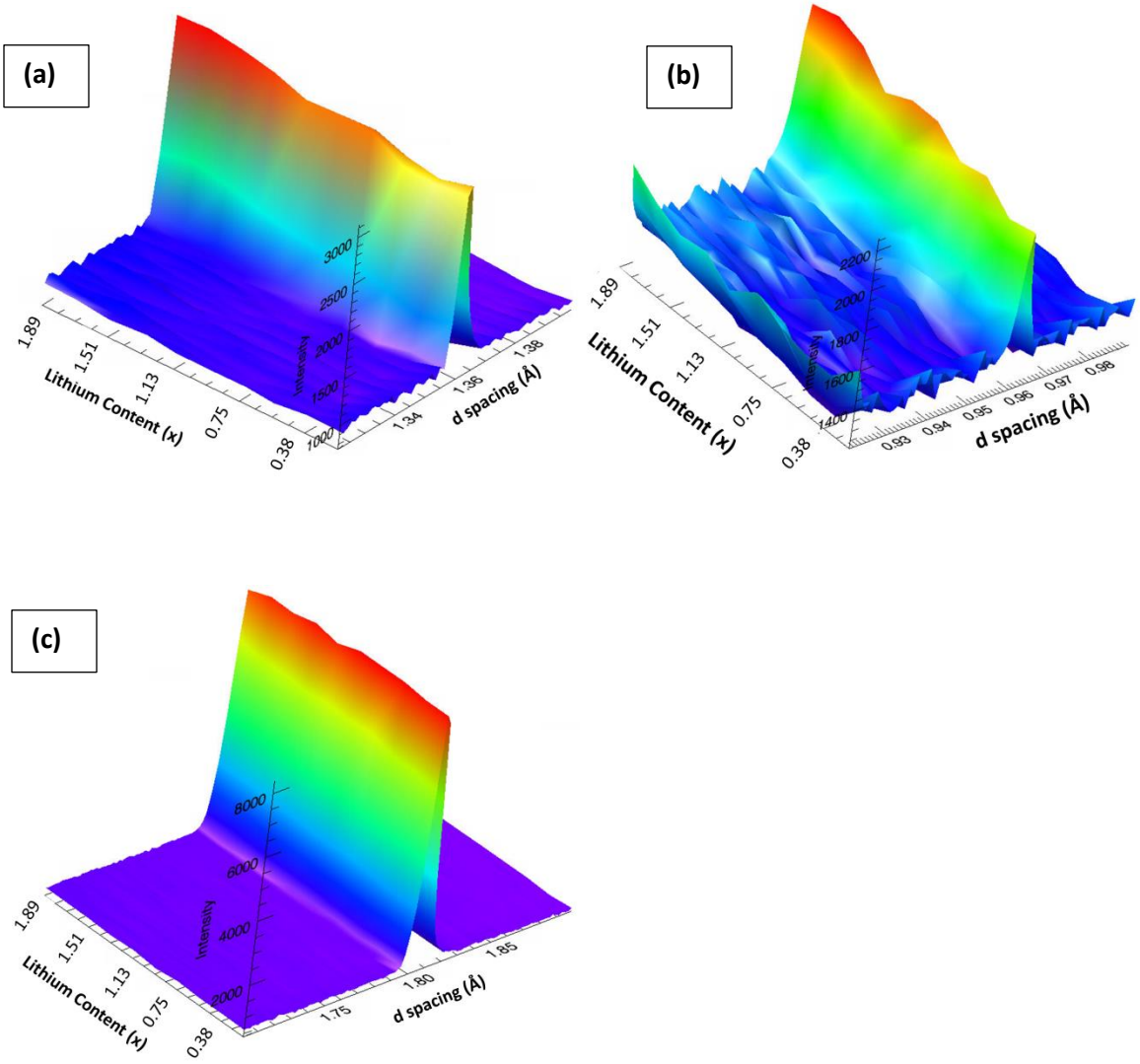

Figure 6.5. In-situ neutron data collected during 1st lithiation cycle of µp-Si electrode at VULCAN, showing the (a) Si (400), (b) Si (440), and (c) Cu (200) peaks.

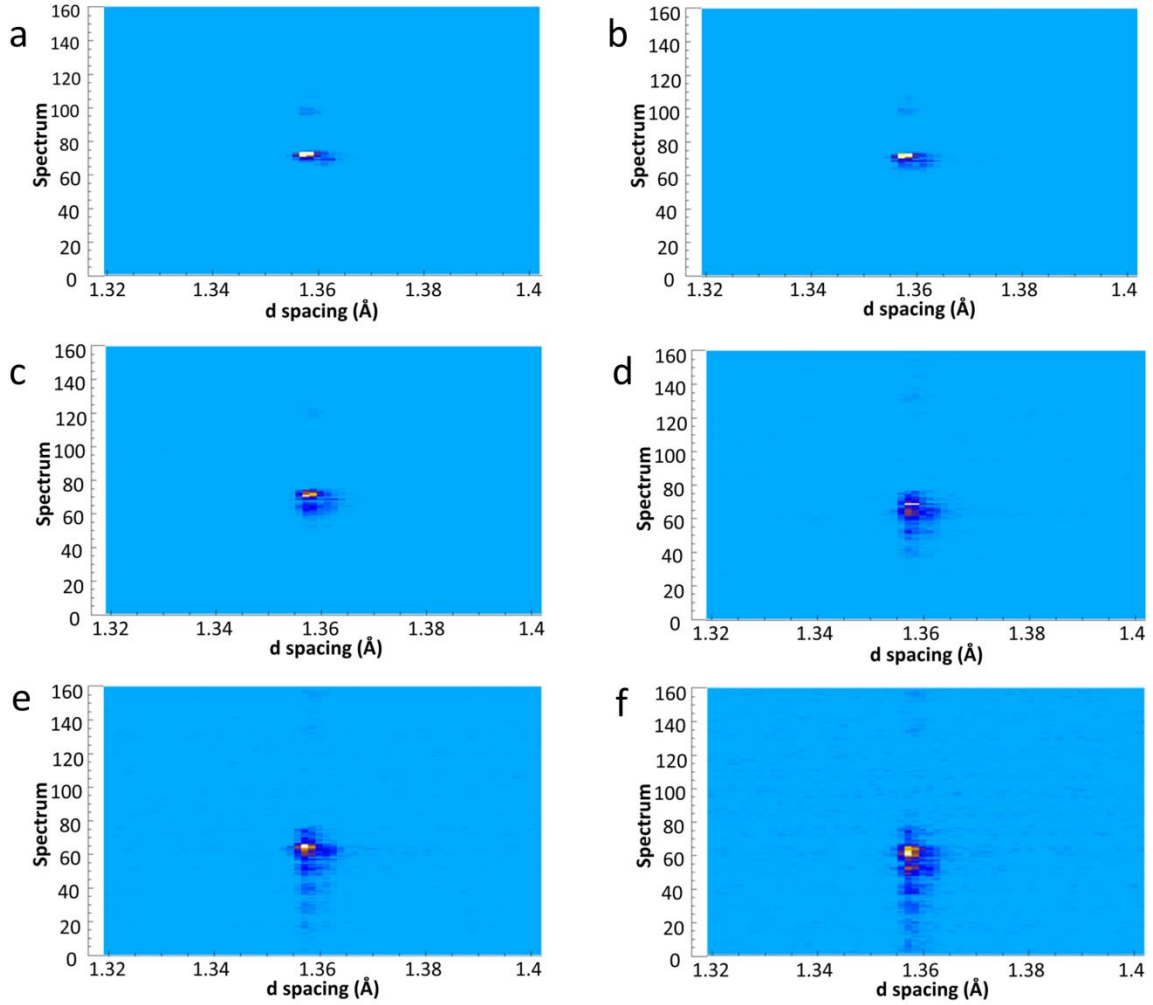

Figure 6.6. 2D projection images showing Si (400) spot at (a) x = 0, (b) x = 0.378, (c) x = 0.756, (d) x = 1.134, (e) x = 1.512, and (f) x = 1.89. The y axes in the plots show the spread of spots. As the value of x increases (lithiation proceeds) the spread of Si (400) spots in vertical direction on detector increases, which indicates evolution of mosaicity.

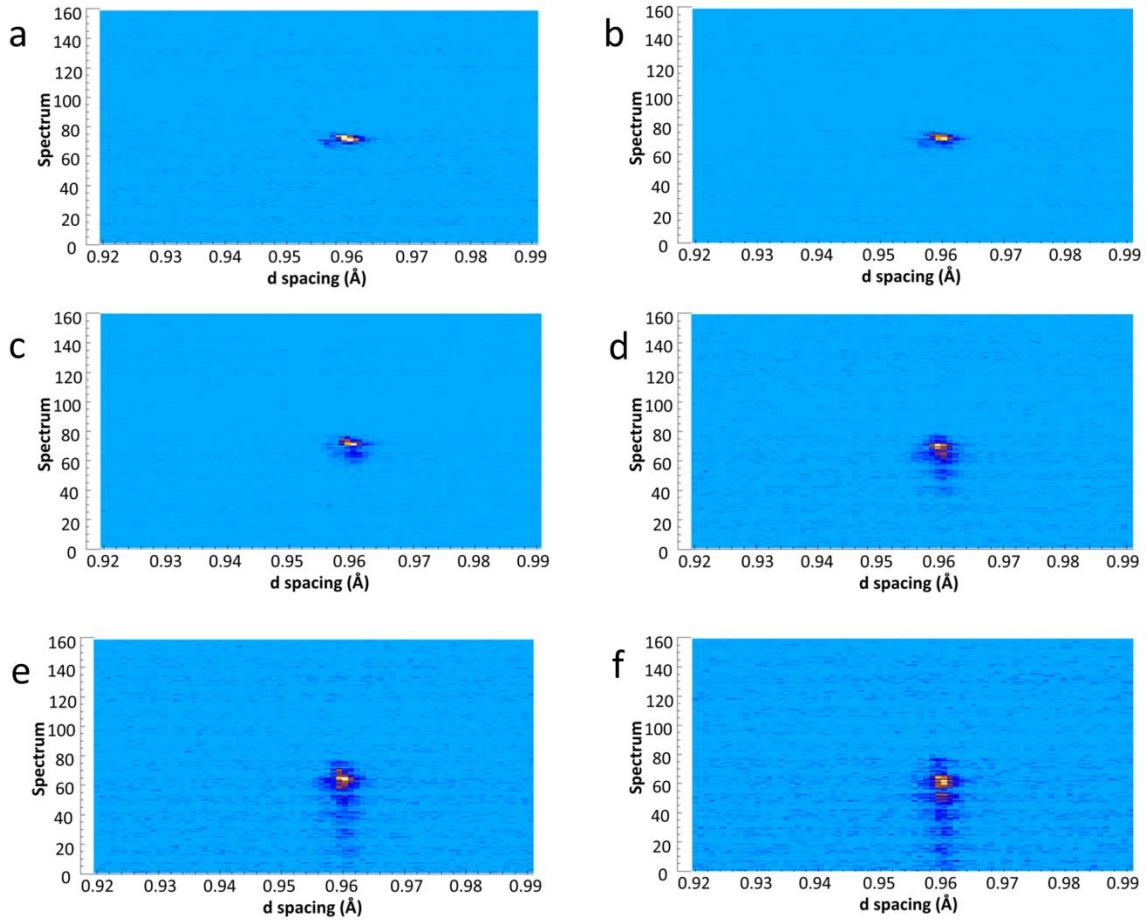

Figure 6.7. 2D projection images showing Si (440) spot at (a) x = 0, (b) x = 0.378, (c) x = 0.756, (d) x = 1.134, (e) x = 1.512 and (f) x = 1.89. The y axes in the plots show the spread of spots. As the value of x increases (lithiation proceeds) the spread of Si (440) spots in vertical direction on detector increases, which indicates evolution of mosaicity.

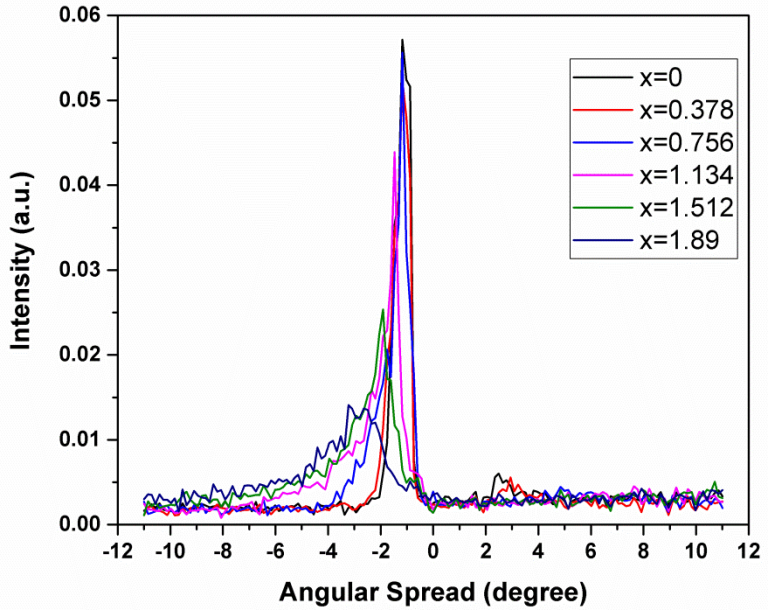

Figure 6.8. The variation of angular spread for the Si (400) spot at various states of charge (x = 0, x = 0.378, x = 0.756, x = 1.512, and x = 1.89).

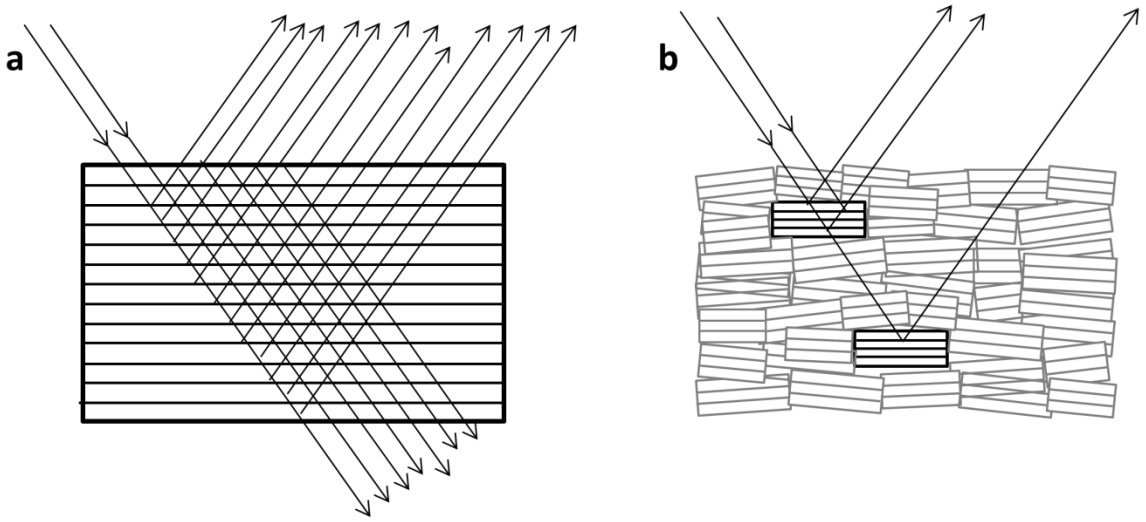

Figure 6.9. Diffraction under (a) dynamic and (b) kinematic conditions in the μp-Si electrode. In the dynamic diffraction condition, due to the multiple reflection of neutrons at planes, a portion of incident neutrons don't enter the detector, resulting in a lower intensity. As the conditions become kinematic, there are domains that satisfy Bragg's law, and relatively more neutrons enter the detector, resulting in higher intensity in the neutron diffraction pattern.

Figure 6.10. Structure evolution in µp-Si cycled for 221 lithiation cycles. (a) Bright Field TEM image showing pores A and B chosen for the study, (b, c) NBD patterns collected from material that grew into pore A, (c-f) NBD patterns collected from material that grew into pore B, and (g) NBD patterns collected from material that grew into pore B. The regions from which NBD patterns b, c, and g are collected are crystalline in nature, whereas the region from which c-f are collected are crystalline + amorphous.

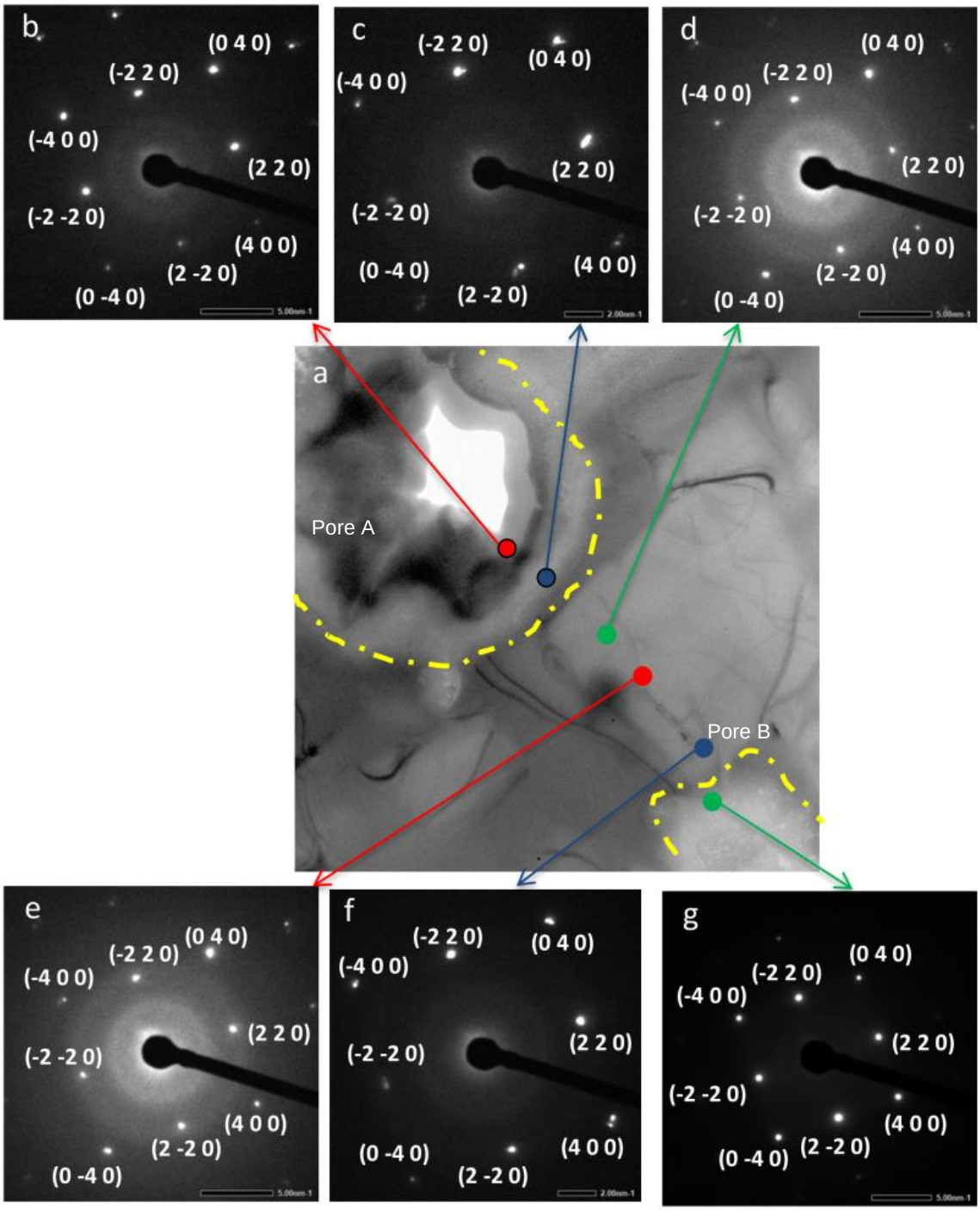
b
(0 4 0)
(-2 2 0)
(-4 0 0)
(2 2 0)
(-2 -2 0)
(4 0 0)
(2 -2 0)
(0 -4 0)
c
(-2 2 0)
(0 4 0)
(-4 0 0)
(2 2 0)
(-2 -2 0)
(0 -4 0)
(4 0 0)
(2 -2 0)
d
(0 4 0)
(-2 2 0)
(-4 0 0)
(2 2 0)
(-2 -2 0)
(4 0 0)
(2 -2 0)
(0 -4 0)
a
Pore A
Pore B
e
(0 4 0)
(-2 2 0)
(-4 0 0)
(2 2 0)
(-2 -2 0)
(4 0 0)
(2 -2 0)
(0 -4 0)
f
(-2 2 0)
(0 4 0)
(-4 0 0)
(2 2 0)
(-2 -2 0)
(0 -4 0)
(4 0 0)
(2 -2 0)
g
(0 4 0)
(-2 2 0)
(-4 0 0)
(2 2 0)
(-2 -2 0)
(4 0 0)
(0 -4 0)
(2 -2 0)

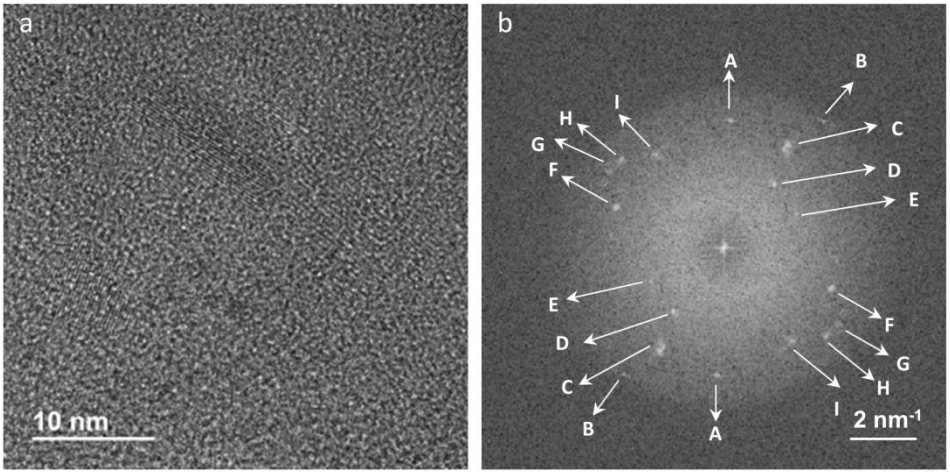

Figure 6.11. HRTEM image with corresponding FFT pattern. (a) HRTEM image from material that has grown into pore B in Figure 6.9 and (b) FFT image corresponding to HRTEM image in (a).

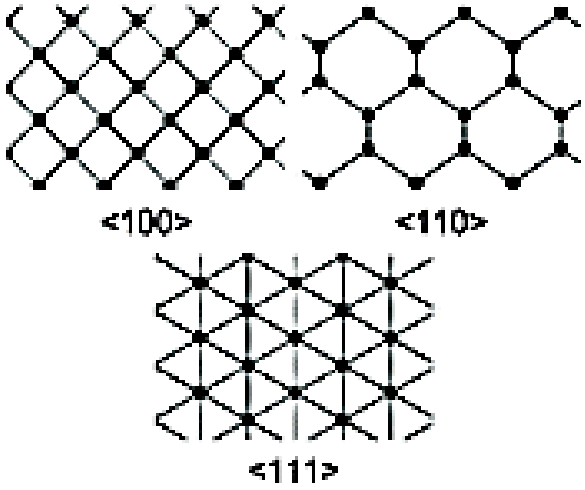

Figure 6.12. Crystallographic view along the directions <100>, <110>, and <111> in the Si lattice. It can be seen that <110> offers the maximum spacing, and hence possesses the lowest activation energy for Li diffusion. Reprinted with permission from S. W. Lee, M. T. McDowell, J. W. Choi, and Y. Cui, *Nano Lett.*, **11**, 3034 (2011).[6] Copyright (2011) American Chemical Society.

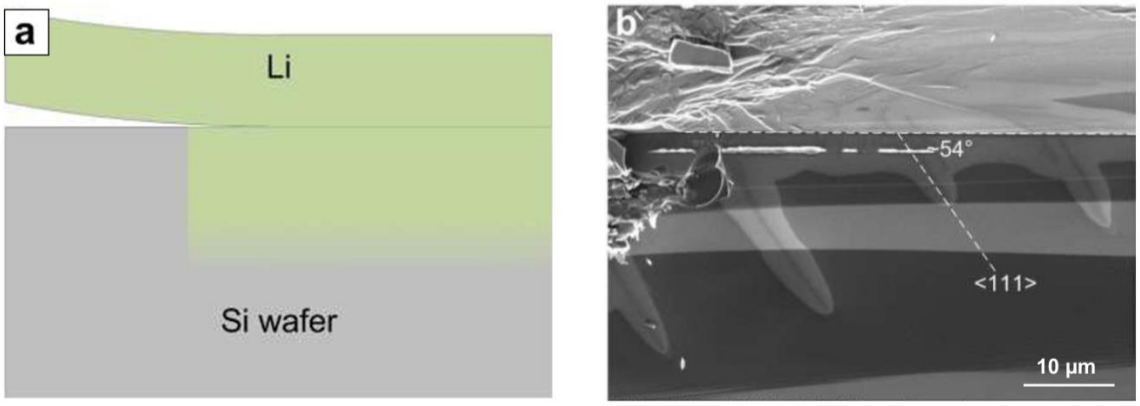

Figure 6.13. Diffusion of Li on surface of Si wafer. (a) Li and Si (100) sheets held together for 5 hrs and (b) SEM micrograph shows Li diffusion occurring perpendicular to {111} planes, resulting in microcracks across the Si {111} planes observed. Reprinted with permission from S. W. Lee, M. T. McDowell, J. W. Choi, and Y. Cui, *Nano Lett*., **11**, 3034 (2011).[6] Copyright (2011) American Chemical Society.

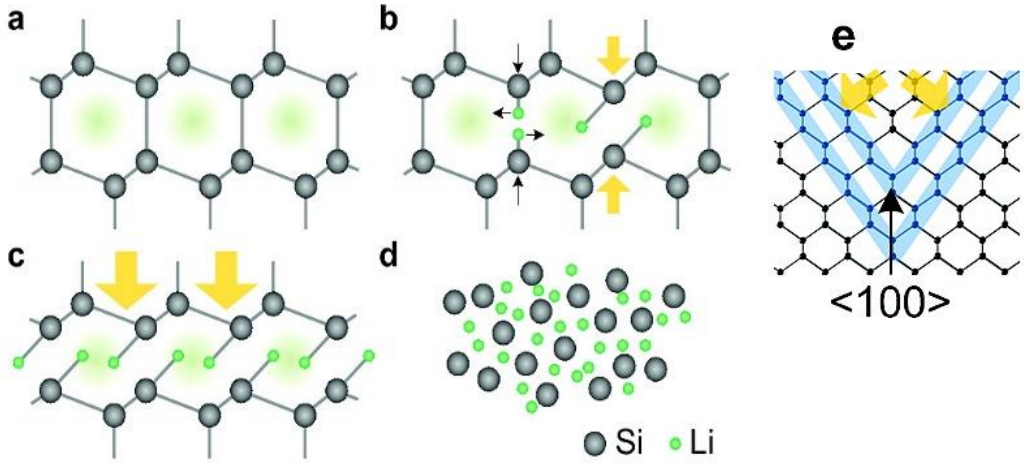

Figure 6.14 Schematic illustrating the mechanism of lithiation in Si nanowire. The images (a-c) show view along the <110> direction. (a-d) Li diffuses along <110> ionic channels and, as a result, the broken Si-Si bonds across {111} planes are replaced by Si-Li bonds. Li atoms slide past each other and enter stable positions as lithiation proceeds. Finally, Si transforms to an amorphous structure. (e) The collapse of {111} planes results in mosaicity. Reprinted with permission from S. W. Lee, M. T. McDowell, J. W. Choi, and Y. Cui, *Nano Lett*., **11**, 3034 (2011).[6] Copyright (2011) American Chemical Society.

6.5 References

1. T. D. Hatchard and J. R. Dahn, *J. Electrochem. Soc*., **151**, A838 (2004).

2. B. Key, R. Bhattacharyya, M. Morcrette, V. Seznec, J. M. Tarascon, and C. P. J. Grey, *Am. Chem. Soc*., **131**, 9239 (2009).

3. H. Liu, J. W. Wang, S. Huang, F. Fan, X. Huang, Y. Liu, S. Krylyuk, J. Yoo, S. A. Dayeh, A. V. Davydov, S. X. Mao, S. T. Picraux, S. Zhang, J. Li, T. Zhu, and J. Y. Huang, *Nat Nanotechnol*., **7**, 749 (2012).

4. J. Li and J. R. Dahn, *J.Electrochem. Soc*., **154**, A156 (2007).

5. M. N. Obrovac and L. Christensen, *Electrochem. Solid-State Lett.*, **7**, A93 (2004).

6. S. W. Lee, M. T. McDowell, J. W. Choi, and Y. Cui, *Nano Lett*., **11**, 3034 (2011).

CHAPTER 7

CONCLUSIONS

The conclusions that can be drawn from the work involving the design of an in-situ electrochemical cell for neutron diffraction studies on small volume Li-ion battery electrodes are the following:

1. A novel in-situ cell that provides good quality neutron diffraction data of structural phase transitions in small volume electrode materials of Li-ion batteries was successfully developed. All the structural transitions in graphite, $LiCoO_2$, and $LiMn_2O_4$, as reported in literature, could be observed, which validates the cell design.

2. The small volume electrodes provided diffraction data of adequate quality, on which with 1 hr binning intervals, Rietveld refinement could be successfully performed and lattice parameters could be extracted. The changes observed in lattice parameters and unit cell volumes are consistent with the structural changes in the electrodes upon lithiation or delithiation.

3. The progression of lithiation in graphite through the solid solution range, Li_xC_6 ($x = 0.04$-0.20), and the phase transitions to LiC_{12} and LiC_6 are clearly seen in the diffraction patterns.

4. The first order phase transition in $LiCoO_2$, form the layered hexagonal phase I to phase I+II, with phase II being a delithiated version of phase I, could be clearly identified from the diffraction patterns.

5. The splitting and formation of two phases during the discharging of $LiMn_2O_4$ could be observed which was not seen in prior ex-situ or in-situ neutron diffraction studies.

The conclusions from the work involving the synthesis and electrochemical testing of Si with columnar-microporous architecture are as follows:

1. Microporous Si, with a columnar architecture, can perform as an electrode material

with superior mass-specific capacity as well as total capacity for energy storage in Li-ion cells.

2. An exceptionally high, record total capacity of ~1.25 mAh/cm^2 (1250 mAh/g) over 220 cycles, for µp-Si, during galvanostatic cycling has been observed. This is comparable to the total storage capacity of $LiCoO_2$ negative electrode (mAh/cm^2) in Li-ion cells.

3. The superior performance of µp-Si is attributed to (i) the increased Si surface area for lithiation, (ii) effective accommodation of volume change within the pore walls, (iii) the preservation of electrical contact at the base of tessellated islands, and, more importantly, (iv) the preservation of the columnar structure of the pores even after the large number of cycling.

The conclusions that can be drawn from the electron microscopy study of the cycling behavior of microporous Si are as follows:

1. The volume expansion associated with lithiation was found to be uniformly accommodated throughout the depth of the pore.

2. The lithiation occurs only along pore walls but not into the base of Si. The calculation of gravimetric capacity, therefore, doesn't need the base to be included.

3. µp-Si assumes a duplex microstructure: (a) "crystalline Si + $Li_{15}Si_4$" in the region which grew into the original pore, and (b) "crystalline Si + amorphous Li_xSi" in the region between pores. The region around the pore shows preferential orientation of Si (2 -2 0) grains.

The conclusions from work involving the investigation of real time phase transitions in microporous Si electrodes are the following:

1. We could successfully observe the changes occurring in the Si lattice during

lithiation from pores just 12 μm in depth.

2. Neuron diffraction coupled with TEM studies established that the Si lattice becomes mosaic during the process of lithiation.